POLITECNICO DI TORINO

Corso di Laurea Magistrale

in Ingegneria Meccanica

Tesi di Laurea Magistrale

Numerical analysis of aerodynamic damping in a transonic compressor

Relatori
Nenad Glodic
Antonio Mittica

Candidato
Vincenzo Stasolla

Anno Accademico 2018/2019

Numerical analysis of aerodynamic damping in a transonic compressor

Vincenzo Stasolla

Master thesis 2019

Master of Science Thesis
KTH School of Industrial Engineering and Management
Department of Energy Technology
Division of Heat and Power Technology
100 44 Stockholm, Sweden

KTH Industrial Engineering
and Management

Master of Science Thesis EGI 2019: TRITA-ITM-EX 2019:612

Numerical analysis of aerodynamic damping in a transonic compressor

Vincenzo Stasolla

Approved Date 2019-09-11	Examiner Björn Laumert	Supervisor Nenad Glodic
	Academic referent Antonio Mittica	Co-supervisor Mauricio Gutierrez Salas

ABSTRACT

Aeromechanics is one of the main limitations for more efficient, lighter, cheaper and reliable turbomachinery, such as steam or gas turbines, as well as compressors and fans. In fact, aircraft engines designed in the last few years feature more slender, thinner and more highly loaded blades, but this trend gives rise to increased sensitivity for vibrations induced by the fluid and result in increasing challenges regarding structural integrity of the engine. Forced vibration as well as flutter failures need to be carefully avoided and an important parameter predicting instabilities in both cases is the aerodynamic damping.

The aim of the present project is to numerically investigate aerodynamic damping in the first rotor of a transonic compressor (VINK6). The transonic flow field leads to a bow shock at each blade leading edge, which propagates to the suction side of the adjacent blade. This, along with the fact that the rotating blade row vibrates in different mode shapes and this induces unsteady pressure fluctuations, suggests to evaluate unsteady flow field solutions for different cases. In particular, the work focuses on the unsteady aerodynamic damping prediction for the first six mode shapes. The aerodynamic coupling between the blades of this rotor is estimated by employing a transient blade row model set in blade flutter case. The commercial CFD code used for these investigations is ANSYS CFX.

Aerodynamic damping is evaluated on the basis of the Energy Method, which allows to calculate the logarithmic decrement employed as a stability parameter in this study. The least logarithmic decrement values for each mode shape are better investigated by finding the unsteady pressure distribution at different span locations, indication of the generalized force of the blade surface and the local work distribution, useful to get insights into the coupling between displacements and consequent generated unsteady pressure. Two different transient methods (Time Integration and Harmonic Balance) are employed showing the same trend of the quantities under consideration with similar computational effort. The first mode is the only one with a flutter risk, while the higher modes feature higher reduced frequencies, out from the critical range found in literature. Unsteady pressure for all the modes is quite comparable at higher span locations, where the largest displacements are prescribed, while at mid-span less comparable values are found due to different amplitude and direction of the mode shape. SST turbulence model is analyzed, which does not influence in significant manner the predictions in this case, with respect to the k-epsilon model employed for the whole work. Unsteady pressure predictions based on the Fourier transformation are validated with MATLAB codes making use of Fast Fourier Transform in order to ensure the goodness of CFX computations. Convergence level and discrepancy in aerodynamic damping values are stated for each result and this allows to estimate the computational effort for every simulation and the permanent presence of numerical propagation errors.

Keywords: transonic compressor, flutter, vibration, CFD

SAMMANFATTNING

Aeromekanik är en av huvudbegränsningarna för mer effektiva, lättare, billigare och mer pålitliga turbomaskiner, som ångturbiner, gasturbiner, samt kompressorer och fläktar. I själva verket har flygplansmotorer som designats under de senaste åren har fått tunnare och mer belastade skovlar, men denna trend ger upphov till ökad känslighet för aeromekaniska vibrationer och resulterar i ökande utmaningar när det gäller motorns strukturella integritet. Aerodynamiskt påtvingade vibrationer såväl som fladder måste predikteras noggrant för att kunna undvikas och en viktig parameter som förutsäger instabilitet i båda fallen är den aerodynamiska dämpningen.

Syftet med det aktuella projektet är att numeriskt undersöka aerodynamisk dämpning i den första rotorn hos en transonisk kompressor (VINK6). Det transoniska flödesfältet leder till en bågformad stötvåg vid bladets främre kant, som sprider sig till sugsidan på det intilliggande bladet. I och med detta, tillsammans med det faktum att den roterande bladraden vibrerar i olika modformer och detta inducerar instationära tryckfluktuationer, syftar detta arbete på att utvärdera flödesfältslösningar för olika fal. I synnerhet fokuserar arbetet på prediktering av den instationära aerodynamiska dämpningen för de första sex modformen. Den aerodynamiska kopplingen mellan bladen hos denna rotor uppskattas genom att använda en transient bladradmodell uppsatt för fladderberäkningen. Den kommersiella CFD-koden som används för denna utredning är ANSYS CFX.

Aerodynamisk dämpning utvärderas med hjälp av energimetoden, som gör det möjligt att beräkna den logaritmiska minskningen som används som en stabilitetsparameter i denna studie. De minsta logaritmiska dekrementvärdena för varje modform undersöks bättre genom att hitta den ostadiga tryckfördelningen på olika spannpositioner, som är en indikering av den lokala arbetsfördelningen, användbar för att få insikt i kopplingen mellan förskjutningar och därmed genererat ostabilt tryck. Två olika transienta metoder används som visar samma trend för de kvantiteter som beaktas med liknande beräkningsinsatser. Den första modformen är den enda med en fladderrisk, medan de högre modformerna har högre reducerade frekvenser, och ligger utanför det kritiska intervallet som finns i litteraturen. Instationärt tryck för alla moder är ganska jämförbart på de högre spannpositioner, där de största förskjutningarna föreskrivs, medan runt midspannet finns mindre jämförbara värden på grund av olika amplitud och riktning för modformen. SST-turbulensmodellen analyseras, som i detta fall inte påverkar predikteringen på ett betydande sätt. Det predikterade instationära trycket baserad på Fourier-transformationen valideras med MATLAB-koder som använder sig av Fast Fourier Transform för att säkerställa noggrannheten hos CFX-beräkningar. Konvergensnivå och skillnader i aerodämpningsvärden anges för varje resultat och detta gör det möjligt att uppskatta beräkningsinsatsen för varje simulering och uppskatta utbredningen av det numeriska felet.

Nyckelord: transonic kompressor, fladder, vibration, CFD

ACKNOWLEDGMENTS

The present work has been developed at Royal Institute of Technology in collaboration with Politecnico di Torino, the support of which is gratefully acknowledged. Thanks to these two institutions, I improved myself in different contexts and I had the opportunity to broaden my horizons.

I would like to express my gratitude to Prof. Björn Laumert at the Chair of Heat and Power Technology at KTH, for giving me opportunity to perform this work at the department.

I am extremely thankful to my supervisor Nenad Glodic at KTH for his offer of the thesis and for his guidance and enthusiastic support in solving the problems faced along this path. Thanks for having involved me in the THRUST Master Program at KTH, where I met new professors and students from whom I could work with and learn new skills.

Thanks to Prof. Antonio Mittica for having accepted to be my supervisor at Politecnico di Torino and for his confidence on my work.

Special thanks to Mauricio Gutierrez Salas, my co-supervisor and postdoctoral researcher at KTH, for his constant insightful tips and important feedbacks, which allowed me to further investigate the suspected aspects and find an optimal solution.

Fundamental has been the support of my mate Salvatore Guccione, with whom I took some courses at KTH and studied together. His advices helped me keep always motivated and overcome every kind of difficulty.

Thanks to all the new friends I met in this wonderful year in Sweden, especially to Alex, Pietro, Marta, Simone, Edoardo, Mara, Giulia, Antonella and all the other people from Björksätra. Thanks to my friends in Italy for always being present.

Endless gratitude goes to my family and in particular to my parents, who have always supported me in every day of my study carrier and have been a warm light especially during hard times. Without them all this would not have been possible!

Table of Contents

List of Figures

List of tables

NOMENCLATURE

Latin Symbols

A	blade oscillation amplitude
c	blade chord, damping coefficient
b	blade height
$\bar{c}_p$	normalized steady pressure coefficient
$\hat{c}_p$	normalized unsteady pressure coefficient $\hat{c}_p = \frac{\hat{p}}{A \cdot p_{dyn}}$
df	infinitesimal force coefficient
dS	infinitesimal arcwise surface component, per unit of span
dZ	displacement in axial direction
f	oscillation frequency
$\vec{f}$	normalized unsteady force vector on span section
F	harmonic force
$\vec{F}$	normalized unsteady force vector on blade
p	pressure
$\bar{p}$	mean pressure
$\tilde{p}$	time-varying pressure perturbation
$\hat{p}$	complex pressure amplitude
$\vec{h}$	complex mode shape vector
h	structural motion
i	imaginary unit, $i = \sqrt{-1}$
k	reduced frequency, based on full chord $k = \frac{2\pi f c}{u}$
l	nodal diameter
m	mass
M	Mach number, mass matrix, harmonic number (HB method)
K	stiffness matrix, kinetic energy

k	stiffness
C	damping matrix
Q	modal displacement vector
$\vec{n}$	normal vector to surface element
t	time, time of flight
Δt	timestep size
T	oscillation period
u, v, w	Cartesian velocity components
W_{cycle}	work per cycle
x, y, z	Cartesian coordinates
x	displacement
Δx	mesh element size
$\dot{x}$	first derivative of displacement
$\ddot{x}$	second derivative of displacement
r	frequency ratio
n, m	blade indices
e	unit vector
Re	real part
Im	imaginary part
N	rotational speed, number
S	stress matrix

Greek Symbols

α	rotation angle, normalized blade oscillation amplitude $\alpha = \frac{h_{max}}{c}$
ϵ	turbulence dissipation rate
ζ	damping ratio
μ	mass ratio
π	pressure ratio

ρ	density
σ	inter-blade phase angle
ω	rotational frequency, $\omega = 2\pi f$
θ	phase lag between torsion and bending
Θ	stability parameter
$\phi_{p\rightarrow h}$	phase angle of response with respect to excitation (motion); the phase angle is per definition positive if the response is leading the excitation
λ	eigenvalue
Ω	rotor speed
ω^*	critical reduced frequency
δ	logarithmic decrement

Subscripts

i	inertial
e	elastic
$a, aero$	aerodynmic
$damp$	damping
$dist$	disturbance
n	natural
ref	reference
dyn	dynamic
BL	blades
L	lift
F	force
M	moment
$-\infty$	machine inlet
B	reference surface
w	work

ave	average

Abbreviation

KTH	Kungliga Tekniska Hogskolan
IBPA	Inter-Blade Phase Angle
ND	Nodal diameter
SDOF	Single Degree Of Freedom
MDOF	Multiple Degree of Freedom
TWM	Travelling Wave Mode
VIGV	Variable Inlet Guide Vanes
R	Rotor
S	Stator
ICC	Inter-Cooling Channel
LPC	Low Pressure compressor
HPC	High Pressure Compressor
LPT	Low Pressure Turbine
HPT	High Pressure Turbine
CFD	Computational Fluid Dynamic
SST	Menter's Shear Stress Transport
CPU	Central Processing Unit
FEM	Finite Element Model
VINK	Virtual Integrated Compressor
ARIAS	Advanced Research Into Aeromechanical Solution
RANS	Reynolds Averaged Navier-Stokes
HCF	High Cycle Fatigue
EO	Engine Order
AIC	Aerodynamic Influence Coefficient
1F, 1B	First Bending

1T	First Torsion
2B	Second Bending
2T	Second Torsion
3B	Third Bending
1E	First Edgewise Bending
FT	Fourier transformation
FFT	Fast Fourier Transformation
TS	Time Steps
P	Period
HB	Harmonic Balance
HA	Harmonic Analysis
TI	Time Integration
SV	Steady-Value
P2P	Peak-to-Peak

1 BACKGROUND

Aeromechanics is one of the main limitations for more efficient, lighter, cheaper and reliable turbomachinery, such as steam or gas turbines, as well as compressors and fans. In fact, aircraft engines designed in the last few years feature more slender, thinner and more highly loaded blades, but this tendency gives rise to increased sensitivity for vibrations induced by the fluid and result in increasing challenges regarding structural integrity of the engine.

The dominant mechanism causing failures in turbomachinery components is the high cycle fatigue (HCF), which may arise from forced vibration as well as flutter, characterized by self-induced and self-sustained oscillations leading to detrimental effects on the structure. The source of such phenomena is attributed to a large spectrum of non-uniformity in the flow field around the regarded components, which creates unsteadiness in time due to blade row interactions, structural motion or separation phenomenon. Therefore, the structure will be stressed by aerodynamic forces depending on the unsteady surface pressure and it will oscillate in different mode shapes.

Moreover, turbomachinery operations in a transonic flow field add influence of shocks, boundary layer interactions and other unsteady flow effects. These phenomena interacting with the structure increase the flow field complexity and might be another possible cause of vibration triggering and subsequent failures.

1.1 The emergence of aeroelasticity

Aeroelasticity is the term used to describe the study of the interaction between the deformation of an elastic structural component exposed to a fluid flow and the resultant of the aerodynamic forces arising from the flow field.

In the past, although the fluid-structural interaction had always been investigated, it was taken more in detail into account with the advent of the Second World War, during which the requirement of high-performance aircrafts became vital. Before then, in fact, aircrafts featured lower performances and engine structures were resistant enough to avoid the appearance of catastrophic phenomena. Therefore, as soon as thrust requirements increased but the technical background in this field was not relevant, several engine failure cases began to occur. One of these dramatic events is remembered as "Kegworth air disaster" (8th January 1989), where 47 people died, out of a total of 126. In particular, the Boeing 737-400, which operated the flight from London to Belfast, crashed just before the landing strip while attempting to make an emergency landing at East Midlands airport, after reporting anomalies to both aircraft engines. The causes of the accident were linked to a fan blade rupture, which affected the compressor operation, damaging it and putting the entire engine out of action. Additionally, the co-pilot did not deactivate the damaged engine, but the one that worked, due to incorrect communication between cabin crew and pilots.

Figure 1.1: Kegworth air disaster

After the accident, analysis showed abnormal vibrations, occurred at high altitude (about 8000 meters) and high power, which led the fan blade to fatigue failure. From then on, it has been mandatory to test all newly designed and significantly redesigned engines under representative flight conditions since before ground test were only performed [1]. A theoretical study on aeroelasticity was conducted by Collar, who introduced a graphical interpretation of the interaction between the different types of forces acting on a structure, the so-called "triangle of forces" shown in Figure 1.2.

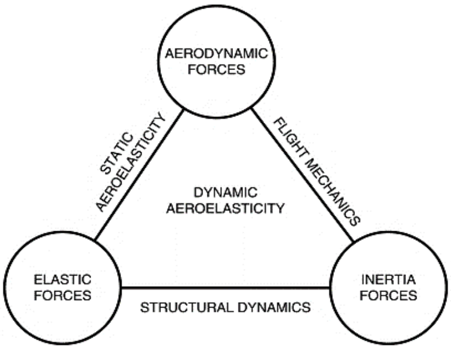

Figure 1.2: Triangle of forces created by Prof. A.R. Colar in 1947 [2]

In light of this, aeroelasticity can be divided in two fields:

- static aeroelasticity, which deals with the steady response of an elastic body in a fluid flow field;
- dynamic aeroelasticity, which deals with the structural dynamic response in a fluid flow field.

1.2 Fluid-structural equation and forced response for a SDOF system

The motion of an elastic structure interacting with a flow field is governed by Newton's equation, which expresses the equilibrium between inertial, elastic and aerodynamic forces:

$$f_i(x, \dot{x}, \ddot{x}) + f_e(x) + f_a(t, x, \dot{x}) = 0 \tag{1.1}$$

Equation (1.1) is non-linear and time dependent, but an analytical formulation of such a system is generally quite complicated to deal with. In order to make the problem easier to solve, small oscillations around an equilibrium state are assumed and this assumption can be considered consistent enough for the present aeroelastic analysis [1]. Therefore, both structural and aerodynamic terms can be appropriately modelled as linear so that the equation of motion around the equilibrium state is expressed as:

$$m\ddot{x} + c\dot{x} + kx = f_a(t) \tag{1.2}$$

where m is the mass distribution, c is the damping and k is the stiffness of the solid structure under consideration. On the right-hand side of equation (1.2), instead, the fluid interaction is modelled by a generic aerodynamic forcing term $f_a(t)$. In case of forced vibration, this time-varying force has a relevant value otherwise it is set to zero representing the free vibration case.

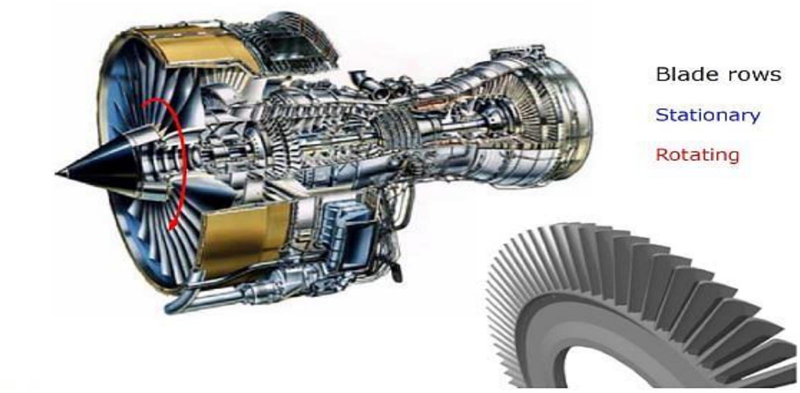

Figure 1.3: Aircraft engine structure and turbomachinery blade row [3]

Within turbomachinery framework, equation (1.2) is applied to one blade of a given blade row moving in the air and one single structural mode is assumed for each blade. The aerodynamic force $f_a(t)$ can be seen as sum of two separate contributions:

$$f_a(t) = f_{dist}(t) + f_{damp}(x, \dot{x}) \tag{1.3}$$

Disturbance forces (f_{dist}) arise from adjacent blade rows, but they might also be due to inhomogeneous distribution of flow parameters at a certain point in the machine, such as the distortion of the inlet flow, the arrangement of the combustion chamber or damage in some blades in the row. Aerodynamic damping force, instead, arises from the oscillation of the solid component and its interaction with the surrounding flow field and in turn can be expressed as summation of two contributions:

$$f_{damp}(x, \dot{x}) = c_a\dot{x} + k_a x \tag{1.4}$$

Since f_{damp} has a damping character, it is shifted to the left hand-side of equation (1.2), and algebraically summed up to the structural damping, so as to obtain the following final expression:

$$m\ddot{x} + (c + c_a)\dot{x} + (k + k_a)x = f_{dist}(t) \tag{1.5}$$

Equation (1.5) shows the aerodynamic contribution to the damping and the stiffness of the system both. These additional effects coming from the fluid-structural interaction can affect the system stability by changing the oscillation frequencies and influencing the structural mode shapes.

Disturbance force can be modelled by a periodic function and thus are expressed as sum of harmonics by means of Fourier transformation [4]. As the system is linear, it is lawful to apply the superposition principle and the generic disturbance force with frequency Ω is expressed as:

$$f(t) = f_0\cos(\Omega t) = Re\{f_0\, e^{i\Omega t}\} \tag{1.6}$$

where Re is the real part of the force, assuming a complex domain. Rewriting equation (1.2) in frequency domain one can obtain the following expression:

$$m\ddot{x} + c\dot{x} + kx = f_0 e^{i\Omega t} \tag{1.7}$$

The particular integral of this differential equation (1.7) is:

$$x = Xe^{i\Omega t} \tag{1.8}$$

where X is a complex constant. By computing the first and the second derivative of equation (1.8) and plugging the derivatives in equation (1.7), the expression of X can be found:

$$X = \frac{f_0}{k - m\Omega^2 + i\Omega c} = Ae^{i(\Omega t + \phi)} \tag{1.9}$$

where A is the amplitude of the motion and ϕ is the initial phase, which can be drawn up as follows:

$$\begin{cases} A = \dfrac{(f_0/k)}{\sqrt{(1 - r^2)^2 + (2\zeta r)^2}} \\ tg\phi = -\dfrac{2\zeta r}{1 - r^2} \end{cases} \tag{1.10}$$

where $r = \frac{\Omega}{\omega_n}$ is the frequency ratio and $\zeta = \frac{c}{2\sqrt{km}}$ is the damping ratio.

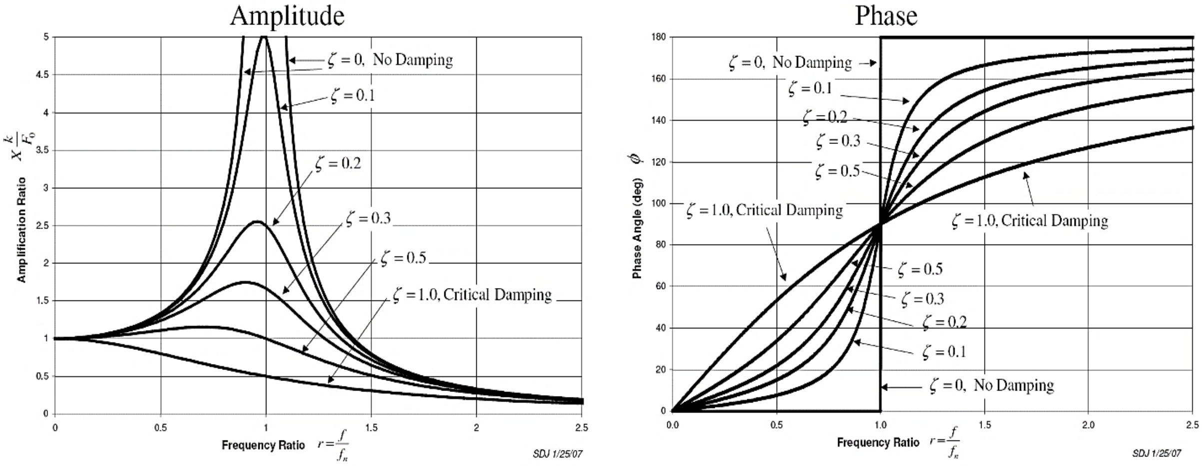

Figure 1.4: Module and phase of the structural displacement for forced response analysis [4]

The response amplitude (A) is seen to be a function of the excitation amplitude (f_0) and excitation frequency (Ω). The resonance condition, characterized by the highest vibratory amplitude, occurs when the damped natural frequency is equal to the excitation frequency, as seen in Figure 1.4; the phase shift between force and motion is $90°$ for every damping ratio in this condition.

1.3 Modal analysis and forced response for a MDOF system

The previous motion equation is obtained for a system with one single degree of freedom (SDOF) oscillating in one direction with a certain natural frequency $\left(\omega_n = \sqrt{k/m}\right)$. However, every vibrating solid body has more directions of motion and corresponding natural frequencies, which determine the structural mode shapes. Therefore, it is possible to resort to a discrete system model by assuming multiple degrees of freedom (MDOF), often used as simplified model for continuous systems. Here again, by combining the structural equations with the ones coming from the unsteady fluid dynamics [1], the following expression is obtained in its compact form:

$$[M]\ddot{q}(t) + [C]\dot{q}(t) + [K]q(t) = F(t) \tag{1.11}$$

where the matrix terms refer to mass, damping and stiffness, while q is conceived as the generalized displacement vector. $F(t)$ refers, instead, to the generalized forces vector and acts as connection between structural dynamics, inertial forces and unsteady aerodynamics. In turbomachinery applications, the two main components prone to vibrate are disk and blade. Oscillation modes for blades and disks can be obtained by a structural FEM analysis. The approach used to find these structural deformations is called modal analysis. In order to perform the latter one it is necessary to set to zero all damping and disturbance force terms. Hence the simplified expression in this case is:

$$[M]\ddot{q}(t) + [K]q(t) = 0 \tag{1.12}$$

where $q(t) = Qe^{i\omega t}$and thus it is possible to pass to frequency domain and define the following eigenproblem:

$$(-[M]\omega^2 + [K])Q = 0 \tag{1.13}$$

where Q represents eigenvectors and ω represents eigenvalues indicating the modal natural frequencies. The number of natural frequencies corresponds to the number of DOFs or mode shapes. Examples of mode shapes for blades and disks, which are known in terms of nodal diameters or inflection lines, are shown respectively in Figure 1.5 and 1.6.

Figure 1.5: Blade modes obtained from FEM analysis

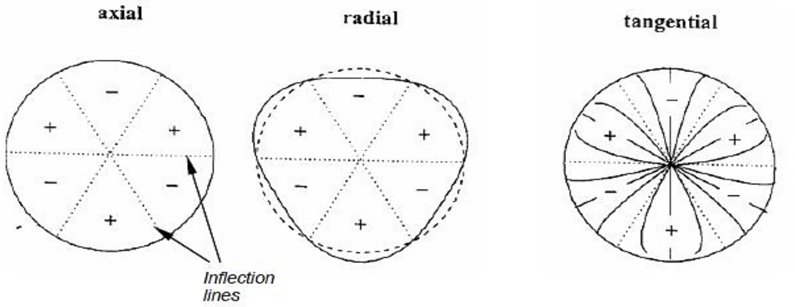

Figure 1.6: Main disk modes

The force imposed on rotating structures derives from circumferential flow field distortions. In fact, any anomaly understood as a construction defect or an interruption in the flow field continuity can be seen as a stimulus source. Each rotating blade is subject to the same variable force field along the circumferential direction. These forces can be decomposed into more harmonics by means of Fourier transformation as previously mentioned and the frequency of each harmonic depends on the rotor speed and on the number of interruptions occurring in the flow continuity. This can be mathematically formulated as follows:

$$F = F_0 + F_1 \sin(\omega_1 t + \theta_1) + \ldots + F_M \sin(\omega_m t + \theta_m) + \ldots \tag{1.14}$$

where the frequency term is expressed as [3]:

$$f = \frac{EO \cdot \Omega}{60} \tag{1.15}$$

where Ω is the rotor speed and EO is the engine order indicating the number of flow disturbances. In the forced response investigation, the maximum vibratory response occurs when excitation frequencies match natural frequencies, as aforementioned for the SDOF analysis. These operational conditions are called resonances and are captured on the so-called Campbell Diagram. Beside the previous ones, other particular frequency-matching events may occur, such as flutter, non-synchronous vibrations and separated flow vibrations. These phenomena are located in specific frequency ranges, close to certain natural frequencies, as shown in Figure 1.7. All these events lead to vibrations in mechanical components with subsequent damages or possible failures due to high stress or HCF.

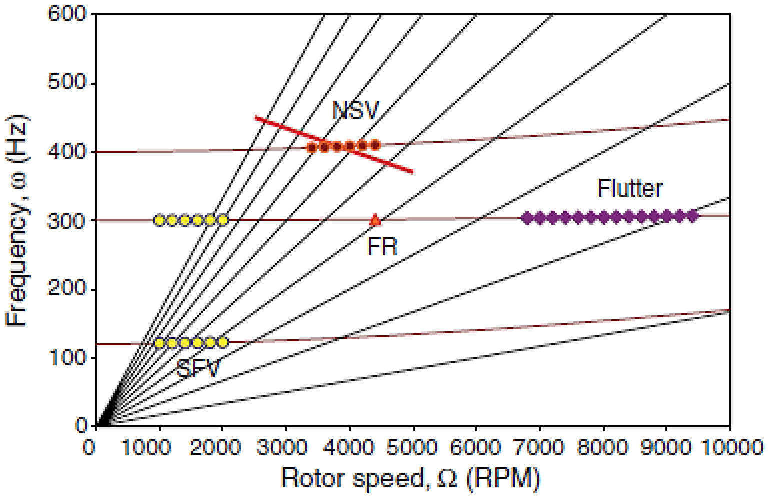

Figure 1.7: Campbell diagram showing frequency ranges for common aeroelastic problems [5]

1.4 Flutter phenomenon

Flutter is a dynamic instability between elastic, inertial and aerodynamic forces. Vibrations are self-excited and self-sustained in this case and no periodic flow disturbances are assumed, which are related to forced vibration case. Therefore, the disturbance force in equation (1.3) is equal to zero and only the coupled force, that is aerodynamic damping, contributes to the blade vibratory response. Blade motion causes pressure variations and thus the emergence of aerodynamic damping force, which can have a stabilizing or detrimental impact on the system stability as function of its amplitude and phase with respect to unsteady pressure. Classical flutter occurs due to an adverse phase difference between the structural motion and the unsteady aerodynamic forces. In other words, unsteady pressure leads structural displacements, which exponentially grow until reaching a limit condition. Flutter is more prone to occur in slender and long blades, on which aerodynamic forces are high enough to interact with the structural forces: fan, low pressure compressor (LPC) and low pressure turbine (LPT) are in this regard the most critical parts in an axial turbomachine. Figure 1.8 represents a typical aircraft engine architecture with focus on components prone to flutter. Blade vibrations at part-speed operation were one of the first problems turbomachine designers had to face with. Such phenomenon was later discovered to be caused by subsonic stalled flutter, which is associated with flow separation in the front stages of compressors operating with higher than nominal incidence. This kind of flutter usually appears for the first torsion mode. Flutter at part-speed operations may also occur in the mid and aft rotor stages when these are in choked condition and operating at low or negative incidence. Either bending or torsion mode of the blades may be involved in the latter case. Additionally for supersonic inflow conditions with either stalled or unstalled flow flutter phenomenon may appear, close to the 100% design speed. High blade loading, supersonic tip and strong shocks characterize this kind of flutter, which primary is of the first bending type. Supersonic stalled flutter can be associated to a movement of the detached bow shock at the entrance of each passage, which impinges the leading edge of the adjacent blade [6]. However, limited data are available and the latter mechanism is not well understood yet. Lastly, the supersonic unstalled flutter is considered to be the most dangerous one as it may occur on the working line for high corrected speeds. It appears in either bending or torsion mode and it afflicts fans rotating with supersonic tips, condition achieved at or near take-off for aircraft applications. From the compressor map in Figure 1.9, it is possible to better identify the limited ranges where flutter may occur in its different forms.

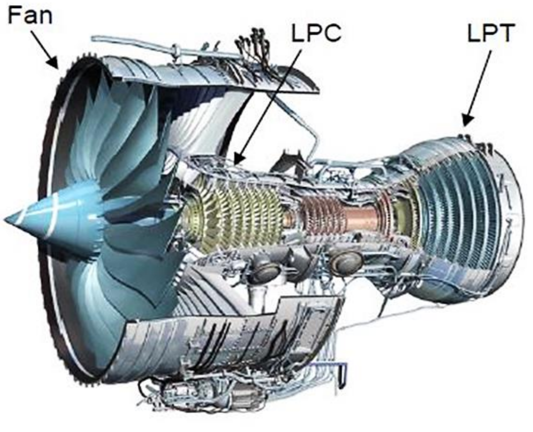

Figure 1.8: Rolls-Royce aeroengine

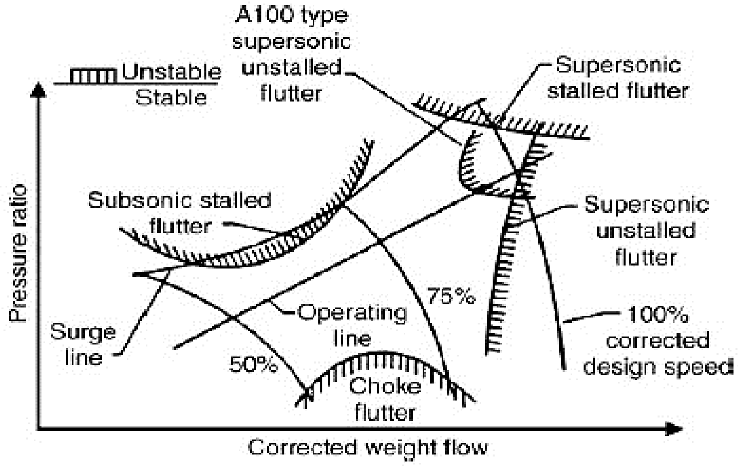

Figure 1.9: Compressor map with flutter boundaries

1.5 Transonic flow in axial compressor

Transonic axial compressors are sensitive components in jet engines as they make it possible to maximize pressure ratios per stage unit. This is achieved through a careful combination of tangential flow deflections and, above all, by taking advantage from shock wave formation around the rotor blades. The resulting flow field is highly complex as it can feature three-dimensional inviscid and viscous structures, strong shock-boundary layer interaction and significant tip clearance effects, which negatively influence compressor efficiency [7]. More in detail, transonic turbomachinery allow to obtain the following benefits:

- reduction in size of the machine;
- use of gases with low speed of sound;
- higher mass ratio and thus higher velocity;
- higher pressure ratios across the stage.

In transonic regime designers usually employ thin and sharp profiles compared to the thicker profiles used in subsonic regime. The Mach number range within which the machine is considered transonic is around $0.8 \div 1.2$. If the first stages of a transonic compressor are taken into account, the flow velocity is higher than the sound velocity and the flow pattern becomes complex [8]. However, flow velocity decreases after the shock and becomes lower than the sound velocity if the shock is normal.

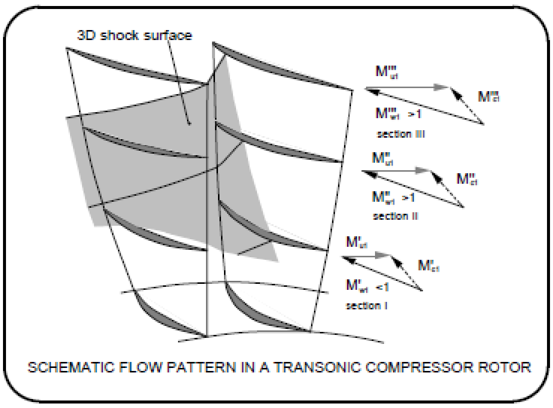

Figure 1.10: Rotating transonic compressor blade row [8]

Phenomena occurring in transonic passages are shock waves, flow separation, secondary flows and it is important to consider them in order to investigate machine efficiency. Drawbacks that these machines may present compared to the subsonic ones are:

- at the transonic velocities, a small variation of the flow surface causes a strong variations in the velocity;
- in the supersonic flow, shock waves appear and produces losses in the total pressure;
- instabilities of shocks and their interaction with the boundary layer can produce strong vibrations of the blade.

Starting from $M > 0.4$ the compressibility effect produces an additional deceleration of the flow through the compressor blades and the pressure ratio increases with the increase in Mach number. The values of the area ratio (outlet area/inlet area) and the relative Mach number at the inlet are limited by:

- the separation of the boundary layer due to strong flow deceleration along the profile;
- the separation of boundary layer downstream a normal shock;
- blockage in the throat of the interblade channel.

For critical Mach number values, the sound speed can be attained locally on the blade. Beyond that value, a supersonic zone arises at the leading edge, terminating generally in a normal shock. The leading edge shocks can extend upstream the blade and these can interact with each other due to non-symmetric flow field generating noise. In some compressors, a variable inlet guide vane can be placed upstream of the first transonic rotor for the purpose of the flow regulations so as to reduce the relative inlet Mach number at the rotor entrance, as shown in Figure 1.11.

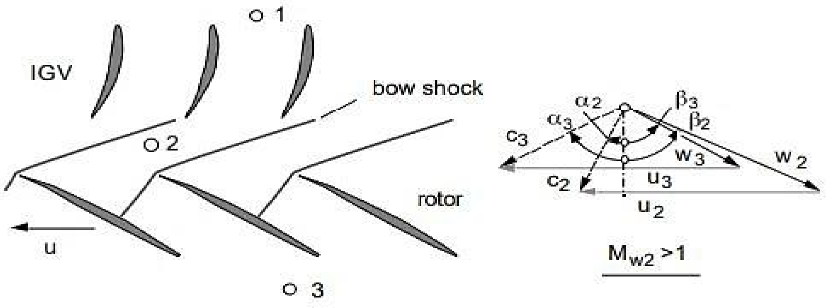

Figure 1.11: Bow shock at leading edge of a compressor rotor [8]

If Mach number upstream from the shock reaches values around 1.35, the boundary layer separates after the shock. This phenomenon has the effect of reducing the pressure ratio and increasing losses, which become more considerable when the flow reaches higher speed. In general, velocities at the inlet of a transonic axial compressor can be subsonic or supersonic, as shown in Figure 1.12.

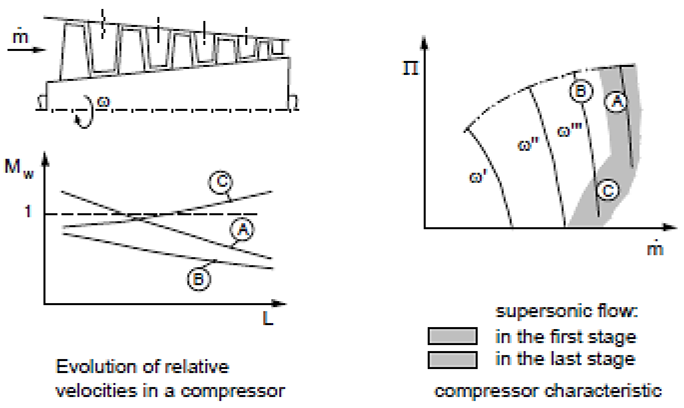

Figure 1.12: Transonic axial compressor features [8]

In case of supersonic inlet velocities, the flow deceleration can be realized by means of a normal shock. Within this framework there are two different types of flow conditions:

- supersonic inlet with attached shock wave;
- supersonic inlet with detached shock wave.

The shock is associated to a certain vibratory frequency. The frequency depends on flow velocity and boundary layer thickness. This obviously becomes a problem if the oscillation induced by the shock has a frequency coinciding with one natural frequency of the structural component. A concrete example can be the case of supersonic unstalled flutter, which is an aerodynamic instability caused by shock waves in blade passages at high speeds.

1.6 Introduction to numerical modeling and CFD-FEM methods

Equation (1.11) can be solved using various numerical strategies. The presence of non-linear terms in the partial differential equations modelling mathematically phenomena under consideration determines the impossibility of obtaining analytical solutions, except for cases in which some assumptions are stated and thus the formulation can be simplified. The discrepancy between numerical and exact solution depends on a number of factors including size and shape of control volumes and size of the final residuals. The choice of the resolution strategy is dictated by modelling requirements of the case. It is necessary to carry out a preventive assessment, which aims to achieve the best compromise between result and solving time. Essentially, here three different approaches enabling to solve fluid-structural equations are presented [9]:

- fully coupled dynamic models, which feature a single solver integrating fluid dynamic equations along with structural ones. Usually computational grids are formulated in the Eulerian viewpoint for the fluid and in the Lagrangian one for the structure. This translates into the achievement of a lower order structural matrix than the fluid matrix. In this case, it is impossible to consider a monolithic type resolution (single solver) for large scale problems. In addition, calculation grids at the interface must be the same and this almost never happens. Therefore, one should create solvers that are designed on purpose for each type of phenomenon, losing modelling generality. Examples of these codes are still relegated to very simple cases of two-dimensional nature, as they also present the disadvantage of having a large computational cost;
- tightly coupled dynamic models, which use different solvers coupled in a single module where the information exchange takes place. This exchange occurs at the interface between the two different computational grids. The fluid-dynamic solver provides the force values to the structural one, which

in turn communicates the displacements. Computational grids are thus moving and this implies that there is also the development of algorithms enabling to modify or reconstruct a new mesh. In this large family of solvers, the implemented equations of fluid dynamics can range from the simple potential flow equation up to the use of RANS equations. On the structural side, both the beam model and the non-linear solid element can be implemented;

- decoupled dynamic models, in which the two environments are solved by separate solvers and thus computational grids can be different, structured, hybrid and non-compliant. In this case, an information exchange interface must be developed. The information exchange is partial and there are only external interactions between the two environments. This method is useful for more simple applications because it loses accuracy in more complex cases. One of the advantages for which these methods are still used lies in the flexibility of use; in fact, it is possible to choose any computational grid or the solver more appropriate for each environment as function of the application.

In the present work, the latter strategy has been used since structural forces can be considered higher than aerodynamic forces for turbomachinery applications and this allow to decouple the interaction between fluid and structure. Therefore, it has been possible to investigate only the fluid environment, while structural displacements were obtained from previous studies not included in this work.

2 THEORETICAL APPROACH

One direct consequence of unsteady flow fluctuations is the appearance of aerodynamic damping, which is a parameter of paramount importance in an aeroelastic analysis. Aerodynamic damping denotes the part of damping arising from the flow around structural components and differs from the structural damping, which depends on blade structural properties. Aerodynamic stiffness appears also due to the aerodynamics around the blades and is summed up along with the structural stiffness. It is necessary to evaluate this parameter during turbine, compressor and fan designs to predict structural vibrations and estimate blade life. This work investigates aerodynamic damping in transonic axial compressor blades with focus on different mode shapes.

2.1 Unsteady surface pressure and aerodynamic coupling

Aerodynamic damping is linked to the unsteady pressure generated originally by the structural motion into the flow field. Harmonic blade motion in time can be expressed as a complex vector $\hat{h}$, whose components represent an arbitrary mode shape. If pressure perturbations are assumed small, unsteady pressure oscillations are also harmonic in time and feature same frequency and a phase shift with respect to the motion vector [10]. Harmonic pressure can be expressed as:

$$p(x,y,z) = \bar{p}(x,y,z) + \tilde{p}(x,y,z,t) = \bar{p}(x,y,z) + \hat{p}(x,y,z)e^{i(\omega t+\phi_{p\to h})} \tag{2.1}$$

where $\bar{p}(x,y,z)$ is the average value of the pressure distribution, while $\tilde{p}(x,y,z)$ represents the pressure perturbation varying in time, which can be seen as complex unsteady pressure amplitude $\hat{p}$ and phase $\phi_{p\to h}$.

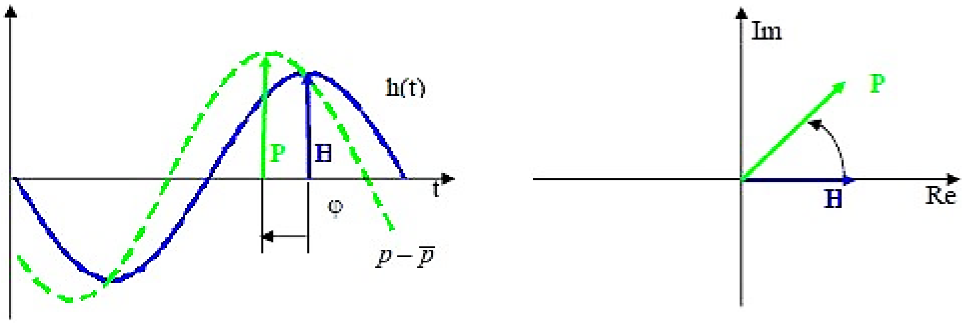

Figure 2.1: Harmonic pressure due to harmonic motion

In turbomachinery, blades are arranged in rows and therefore potentially influence each other. This interaction is referred to as aerodynamic coupling and consists in a blade of the row, which and induces an unsteady pressure field around other blades of the row. The coupling is such that all blades have an influence on each other. Hence, even though blades can be structurally isolated, they are coupled together through aerodynamics. Aerodynamic influences between blades are represented with complex values as the motion of each blade has a lag phase called Inter-Blade Phase Angle. In most cases, the influence of the oscillating blade on itself (direct influence) is stabilizing that means a single blade would not flutter, while the influence of other surroundings blades can lead to an unstable condition. If the influences from adjacent blades are greater in magnitude than the direct influence, then the stability of the entire setup will be negative. Hence there will be negative aerodynamic damping and this leads to increasing vibrations. Aerodynamic coupling may also arise from acoustic wave reflections due to influence coming from adjacent blade rows. In fact, upstream or downstream blade rows might receive an acoustic wave from the blade row under consideration and the subsequent reflection waves can affect system stability. This effect is neglected in the present work by using non-reflective boundary condition at the inlet and outlet interfaces, particularly needed for cut-on frequency configurations [11].

2.2 Aerodynamics and mode shapes interaction

Turbomachinery structures can oscillate in certain modes involving blade and disk deformations. As possible to see in Figure 2.2, the motion is disk-dominated for lower NDs, while it becomes blade-dominated for higher NDs characterized by a constant trend as function of ND; in the middle, instead, there is a veering region, which corresponds to a structural coupling area between blade and disk.

Figure 2.2: Coupled blade and disk modes

The coupling between flow and mode shapes can significantly affect the system dynamics, thus it is important to investigate this phenomena. The difficulty when predicting aerodynamic damping is that the flow behavior changes with operating point as well as with oscillation frequency even though unstable modes are not known a priori. Generally, any possible combination of mode, frequency and operating point needs to be analyzed to fully investigate aerodynamic damping. Modern CFD techniques are utilized to predict unsteady aerodynamics in turbomachinery. These methods are quite reliable, but they sometimes might fail due to specific flow structure or presence of acoustic modes. For this purpose, it is important to use a structured approach in order to validate methods and numerical setups used in the analysis, such as conducting a sensitivity study for the most important parameters to better understand their influence on numerical predictions. Another method to predict instabilities due to aerodynamic coupling is to calculate the reduced frequency ω^*:

$$\omega^* = \frac{\omega \cdot c}{v_{ref}} \tag{2.2}$$

where ω is the natural frequency, c is the blade chord and v_{ref} is the relative velocity at the compressor inlet. Before the emergence of CFD methods, the reduced frequency was the most important parameter used to estimate flutter risk; for low values of reduced frequency $(0.1 \div 1)$, in fact the flutter risk is high. Previous investigations has shown that an increase in the reduced frequency leads to a stabilizing effect on aeroelastic stability [12]. These studies have also shown that some mode shapes are more sensitive to reduced frequency changes than other ones, thus it can be useful to carry out a critical reduced frequency sensitivity study for each mode shape. In the present project except for the first mode analysis used as baseline, the other modes feature reduced frequency values out of the critical range, thus the flutter risk is not significant.

A graphical method developed to assess aerodynamic stability on a two dimensional section is called mode shape sensitivity plot [13]. This method is based on representing any possible pure rigid body mode as torsion mode around a respective center of torsion in order to determine the critical reduced frequency for different structural modes, as possible to see in Figure 2.3.

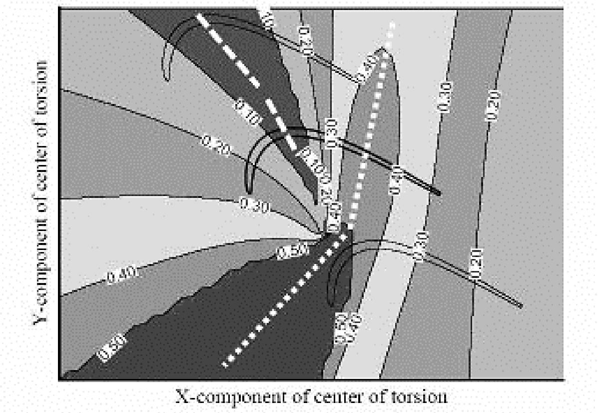

Figure 2.3: Stability plots, also called tie-dye plots [14]

2.3 Theoretical methods for aerodamping predictions

One parameter of interest in this analysis is the mass ratio that is the blade mass divided by the mass of the air entrapped in a circle of diameter equal to the blade chord and can be expressed as:

$$\mu = \frac{4m}{\pi \rho_0 c^2} \tag{2.3}$$

where c is the blade chord, m is the blade mass and ρ_0 is the air density. A typical assumption stated for turbomachinery applications is that the mass ratio has a high value and this implies that structural forces dominate and aerodynamic forces cannot modify the mode shape. Therefore, the aeroelastic investigation can be easily decoupled so that aerodynamic and structural analysis are separately computed. Mesh displacements are obtained by a structural FEM analysis and are associated to CFD mesh in order to solve the unsteady aerodynamics.

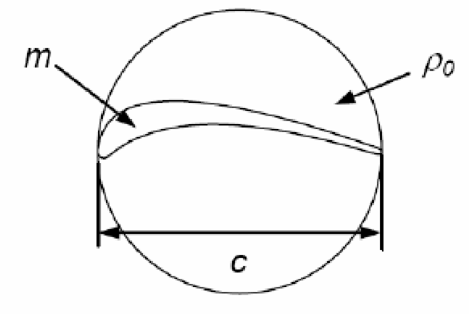

Figure 2.4: Graphical representation of mass ratio

The mathematical approach employed to model aerodynamic interaction between adjacent blades is based on Traveling Wave Mode, which is the way whereby energy is transferred around a blade row [15]. Blades are assumed tuned that means every blade of the row is supposed to have exactly the same structural and material properties (same stiffness and density). In reality, blades are not equal to each other due to manufacturing tolerances or different wear during operations thus they can be defined randomly mistuned. A supplementary effect can be added by intentional mistuning consisting in varying the blade natural frequency by some percentage order in a certain mistuning pattern. This helps to break the TWM in case of flutter, while it may increase oscillation amplitude in case of forced response and lead to more severe conditions. In a TWM each blade oscillates at equal amplitude and frequency, but with a constant phase lag between two adjacent blades. This angular shift between two adjacent blades is referred to as Inter-Blade Phase Angle. This parameter is estimated as:

$$\sigma = IBPA = \frac{2\pi ND}{N_{BL}} \tag{2.4}$$

where ND is an integer number representing the number of nodal diameters under consideration, which ranges between $\pm N_{BL}/2$ (positive ND represents a forward travelling wave mode and negative ND represents a backwards travelling wave mode), while N_{BL} is the number blades in the row. For each $IBPA$ value the resulting mode shape can be analyzed in terms of aerodynamic damping by performing a transient blade row analysis. The incipient flutter condition occurs when the oscillation imposed on the blading starts to diverge.

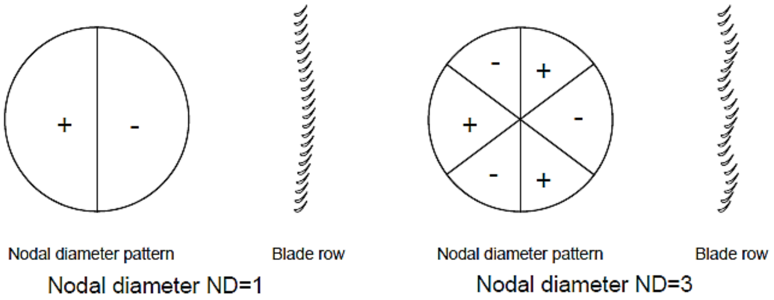

Figure 2.5: TWM for different nodal diameter patterns [12]

Different approaches can be implemented to predict aerodynamic damping, such as the Travelling Wave Mode method and the Aerodynamic Influence Coefficient method (AIC). These two techniques can be also referred to as respectively energy method and direct method. The latter technique is complementary to the first one and enables to get an insight into aerodynamic coupling mechanisms. Structural and material damping contributions are usually neglected in these investigations. This because the aim is to analyze the fluid behavior, thus only the aerodynamic contribution is relevant.

2.3.1 Travelling wave mode analysis and energy method

In the present work, each single structural mode is separately investigated in different its aeroelastic modes, which are TWMs. In a TWM, each blade will experience the same unsteady pressure field and a phase shift equal to IBPA with respect to the adjacent blade. It is thus possible to measure the unsteady pressure field around a reference blade to reconstruct the pressure field around all the blades of the same row.

Starting from combined mode shapes each single structural mode shape can be decoupled by neglecting mixed work contributions [16]. Therefore, the following discussion aims at understanding the complexity of coupling between structural modes, which in reality is present and gets an insight into mathematical workaround addressing to split contributions up. After knowing the unsteady aerodynamics for each mode and blade motion, the energy method can be applied for the evaluation of aerodynamic damping.

Every blade is considered a rigid body vibrating in a three dimensional space. It has been assumed that the blades are oscillating in three orthogonal mode shapes:

- bending in two directions (chord direction and orthogonal to chord direction);
- torsion (or pitching), around the axis orthogonal to the machine rotation and passing through the blade mass center.

The directions of the above described modes are shown in Figure 2.6.

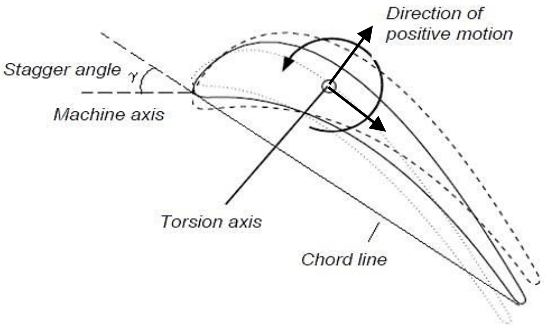

Figure 2.6: Combined blade mode shapes

It is assumed that the torsion motion has a phase lag θ_a with respect to the bending motion, thus they result temporally shifted [17]. The prescribed law is given in complex form:

$$h^m(x,y,t) = h^m(x,y)e^{i\omega^m t}e_h \tag{2.5}$$

$$\alpha^m(x,y,t) = \alpha^m(x,y)e^{i(\omega^m t+\theta_a^m)}\,e_z \tag{2.6}$$

where h and α are the absolute values of oscillation amplitude and ω is the oscillation frequency. Equations (2.5) and (2.6) represent respectively the translation motion and the rotation motion. Given the unsteady nature of the flow field, the flow can be decomposed in two parts, which are steady flow and an unsteady linear perturbation. The steady pressure coefficient can be expressed as follows:

$$\bar{c}_p(x) = \frac{\bar{p}(x) - \bar{p}_{-\infty}}{\mathring{\bar{p}}_{\infty} - \bar{p}_{-\infty}} \tag{2.7}$$

where $\bar{p}$ is the average static pressure value at points along the profile, while $\mathring{\bar{p}}_{-\infty}$ and $\bar{p}_{-\infty}$ are the average values of total and static pressure at the machine inlet. Lift, force and moment coefficients are instead evaluated as:

$$\tilde{c}_{L,A}(t) = \frac{\oint \tilde{p}^B(x,t)\{e_n e_y\}ds}{A\{\mathring{\bar{p}}_{-\infty} - \bar{p}_{-\infty}\}} \tag{2.8a}$$

$$\tilde{c}_{F,A}(t) = \frac{\oint \tilde{p}^B(x,t)\{e_n e_f\}ds}{A\{\mathring{\bar{p}}_{-\infty} - \bar{p}_{-\infty}\}} \tag{2.8b}$$

$$\tilde{c}_{M,A}(t) = \frac{\oint R_a \otimes \{\tilde{p}^B(x,t)e_n ds\}e_z}{A\{\mathring{\bar{p}}_{-\infty} - \bar{p}_{-\infty}\}} \tag{2.8c}$$

where $\tilde{p}^B$is the unsteady pressure amplitude and R_a is the radius vector. The reference surface is denoted by apex B, which may be the suction or pressure side of the blade profile. The lift coefficient is calculated in the direction orthogonal to the blade chord (e_y), while the force coefficient in the chord direction (e_f). The unit vector e_n is orthogonal to the blade profile and the integration step ds is the distance between two adjacent points describing the profile curve. It is possible to notice that all the previous coefficients are normalized by using the non-dimensional parameter A:

$$A=\frac{A_m}{c} \tag{2.9}$$

where c is the chord and A_m is the prescribed displacement amplitude. The unsteady pressure coefficient can be now introduced [12]:

$$\tilde{c}^{B}_{p,A}(x,t)=\frac{\tilde{p}^{B}(x,t)}{A(\bar{p}^{\circ}_{-\infty}-\bar{p}_{-\infty})} \tag{2.10}$$

It is thus possible to substitute equation (2.10) in equations (2.8) so as to obtain expressions as function of the unsteady pressure coefficient. The global pressure coefficient can be expressed as the summation of the steady pressure coefficient in time and the unsteady pressure coefficient:

$$\tilde{c}_p^{global}(x,t)=\bar{c}_p(x)+A\tilde{c}_p(x,t)=\frac{\{\bar{p}-\bar{p}_{-\infty}\}+\tilde{p}^{B}(x,y)}{\{\bar{p}^{\circ}_{-\infty}-\bar{p}_{-\infty}\}} \tag{2.11}$$

The unsteady pressure coefficient in time domain can be transferred to frequency domain by means of Fourier transformation in order to reduce solving efforts:

$$\begin{aligned}\tilde{c}_p(x,t)=\tilde{c}_p(x)e^{\omega t+\phi_p(x)}=\tilde{c}_p(x)e^{i\omega t}e^{\phi_p(x)}=\hat{c}_p^{complex}(x)e^{i\omega t}\\ =\left(Re\{\hat{c}_p^{complex}(x)\}+Im\{\hat{c}_p^{complex}(x)\}\right)e^{i\omega t}\end{aligned} \tag{2.12}$$

where Re and Im are real and imaginary component of the pressure coefficient. The real component is in phase with the harmonic motion, while the imaginary part is out of phase. The two-dimensional aerodynamic work per height unit performed by aerodynamic forces and moments on the blade, considered as a rigid body, is conventionally expressed by the product of the real part of the force, or the moment, and respectively of the real part of translation, or torsion of the body:

$$\tilde{c}_{w,h=}\int Re\{h(x,y,z)\tilde{c}_h(t)\}Re\{dh(x,y,t)\} \tag{2.13a}$$

$$\tilde{c}_{w,h=}\int Re\{\alpha(t)\tilde{c}_M(t)\}Re\{d\alpha(t)\} \tag{2.13b}$$

$$\tilde{c}_{w,h,\alpha=}\int Re\{h(x,y,z)\tilde{c}_{m,h}(t)\}Re\{d\alpha(t)\} \tag{2.13c}$$

$$\tilde{c}_{w,h=}\int Re\{\alpha(t)\tilde{c}_{m,\alpha}(t)\}Re\{dh(x,y,t)\} \tag{2.13d}$$

where the first two terms of equations (2.13) represent the pure works, which are bending and torsional work, while the last two terms represent the mixed work contributions. The total work can be then calculated by summing up the four contributions, as shown in the equation below:

$$\tilde{c}_w=\tilde{c}_{w,h}+\tilde{c}_{w,\alpha}+\tilde{c}_{w,h,\alpha}+\tilde{c}_{w,\alpha,h} \tag{2.14}$$

If now the degrees of freedom are decoupled, only pure bending and pure torsional work survive. By integrating the previous expressions one can obtain:

$$\tilde{c}_{w,h}=\pi h^2 Im\{\tilde{c}_h^{complex}\}=\pi h^2\tilde{c}_h sin\phi_h \tag{2.15a}$$

$$\tilde{c}_{w,\alpha}=\pi h^2 Im\{\tilde{c}_h^{complex}\}=\pi h^2\tilde{c}_M sin\phi_M \tag{2.15b}$$

$$\tilde{c}_{w,h,\alpha}=0 \tag{2.15c}$$

$$\tilde{c}_{w,\alpha,h}=0 \tag{2.15d}$$

It can be seen from equations (2.15) that aerodynamic work depends only on the phase of the force or moment coefficient. Aerodynamic work can be normalized and this allows to obtain the expression of aerodynamic damping coefficients for bending and torsion mode:

$$\Theta_h = -\frac{\tilde{c}_{w,h}}{\pi h^2} \tag{2.16a}$$

$$\Theta_\alpha = -\frac{\tilde{c}_{w,\alpha}}{\pi \alpha^2} \tag{2.16b}$$

This value is positive when the flow dampens blade vibration, while it is negative when the fluid gives energy to the blade.

Energy method directly assumes one degree of freedom for each blade and high mass ratio enabling to decouple the fluid dynamics from the structural dynamics. A simplified formulation of the unsteady work per cycle [2] for a single structural mode is written as:

$$W_{aero} = -\int_A \pi h \cdot \bar{n} p i dA \tag{2.17}$$

where h is the maximum displacement, p_i is the imaginary component of the pressure and $\bar{n}$ is the unit vector normal to the blade surface part considered. Another parameter useful to define in this analysis is the average kinetic energy of the blade, which has the following final expression:

$$KE_{ave} = \frac{\omega^2}{4} \tag{2.18}$$

This latter formulation is obtained starting from the definition of kinetic energy for a rigid body moving in a single structural mode:

$$KE_{ave} = \frac{1}{2} m v^2 \tag{2.19}$$

where m is the body mass and v is its velocity, which is the derivative of the harmonic motion:

$$x(t) = \bar{x}\cos(\omega t) \tag{2.20a}$$

$$v(t) = -\omega \bar{x}\sin(\omega t) \tag{2.20b}$$

where since the time-average value of $\sin^2(t)$ is equal to $1/2$, then equation (2.18) can be obtained. For a given mode, it is possible to get the S-shape curve, which enables to recognize stable and unstable regions. This curve can be build up by using aerodamping coefficient values as function of the IBPA or evaluating the logarithmic decrement values for each configuration. The logarithmic decrement is defined as the relative change in amplitude per cycle and is estimated by the expression below:

$$\delta = \frac{-W_{aero}}{4KE_{ave}} \tag{2.21}$$

It is important to evaluate the average kinetic energy of the blade and the aerodynamic work at the same blade amplitude in order to be consistent in the analysis.

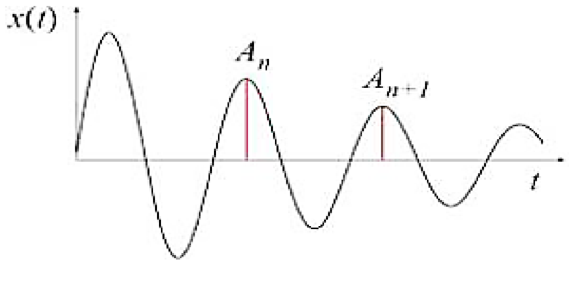

Figure 2.7: Grafical representation of the logarithmic decrement

In Figure 2.8 an example of S-shape curve obtained by a numerical analysis performed on AETR blading [18] by using energy method is shown. Under the stability line, the blade row is subject to negative aerodamping values which may lead to consequent failures if the structural damping is not adequate.

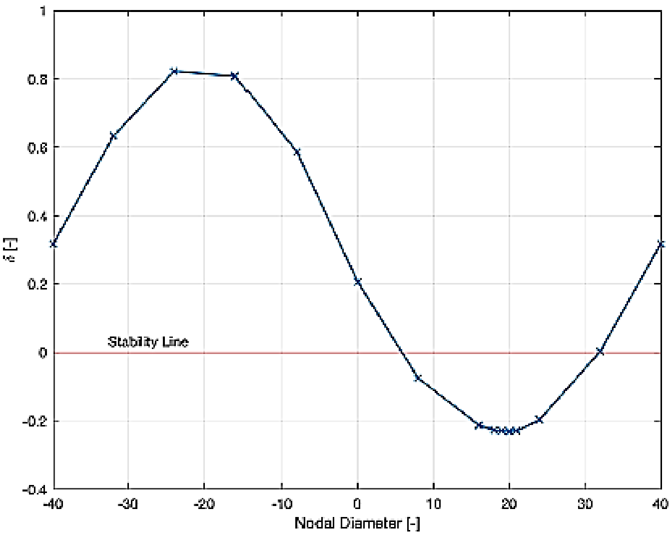

Figure 2.8: Log-dec versus ND plot for AETR blade row [18]

2.3.2 Aerodynamic Influence Coefficient method (or direct approach)

Another approach investigating on aerodynamic coupling in a blade row is the Aerodynamic Influence Coefficient method. The unsteady pressure around one blade is the composition of the unsteady pressure distribution generated by the oscillation of the blade itself and the one induced by oscillations of the other blades in the same row. It was shown that the influence of each blade on the unsteady response superimposes linearly [15] and this requires small perturbation amplitudes around a reference value. Therefore, in this case the TWM is cut down in order to analyze the single blade influence on itself and on the unsteady flow surrounding the other blades of the row.

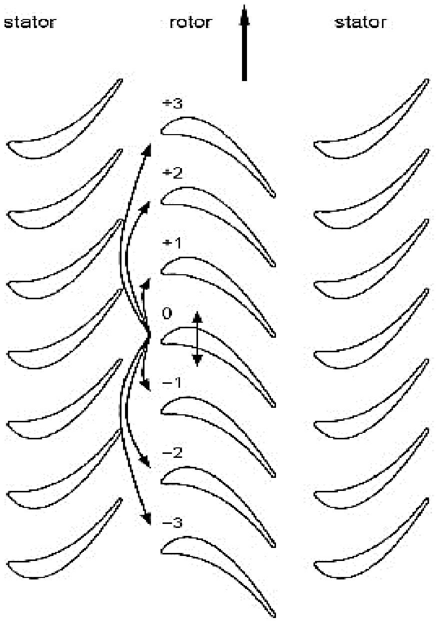

Figure 2.9: Influence between adjacent blades

If the blade m is considered to be the central blade on which the pressure is measured, experimentally it is necessary to get oscillating it and register the unsteady pressure field around it. Then a small vibration amplitude is prescribed on the blade $m + 1$ and the unsteady pressure on blade m is measured. This procedure is repeated for all the blades out of blade m to measure influences of all blades on it. TWM is cut down at blade m for influence coefficient measurements. In this case, even though structural forces are not completely dominating as in the previous case, it is possible to get reliable predictions of aerodynamic damping. In a tuned system, it is assumed that the global unsteady pressure coefficient can be written by linear combination of contributions deriving from all other blades. It is possible to derive the following formulation:

$$\tilde{c}_{p,TWM}^{m,\sigma}(t) = \sum_{n=-N}^{+N} \tilde{c}_{p,IC}^{n,m}(t)e^{i\sigma n} \tag{2.22}$$

where $\tilde{c}_{p,TWM}^{m,\sigma}(t)$ represents the aerodynamic unsteady pressure coefficient acting on the blade m, $\tilde{c}_{p,IC}^{n,m}(t)$ is the dynamic pressure coefficient imposed by the vibrating blade n on the non-vibrating blade m, the exponent σn is IBPA between blade n and blade m. Equation (2.22) can be better rewritten in another form:

$$\tilde{c}_{p,TWM}^{m,\sigma}(t) = \sum_{n=-N}^{+N} \tilde{c}_{p,ic}^{n,m}(t)e^{i\omega\sigma(n-m)} \tag{2.23}$$

and by replacing m with the reference blade index $(m = 0)$, the following expression is obtained:

$$\tilde{c}_{p,TWM}^{0,\sigma}(t) = \sum_{n=-N}^{+N} \tilde{c}_{p,ic}^{n,0}(t)e^{i\omega\sigma n} \tag{2.24}$$

When the blade with $n = 0$ influences the reference one $(m = 0)$, then the considered influence coefficient expresses the influence that the blade has on itself. Trivially, this contribution does not depend on the IBPA and is called self-influence coefficient. Once calculated, the described coefficient can be reported on a polar graph where its amplitude represents the vector length and its phase is the displacement between the unsteady aerodynamic response and the movement itself, as possible to see in Figure 2.12. If the blade receives energy from the fluid, the imaginary part is positive. Starting from this value, the contribution of the other blades is added.

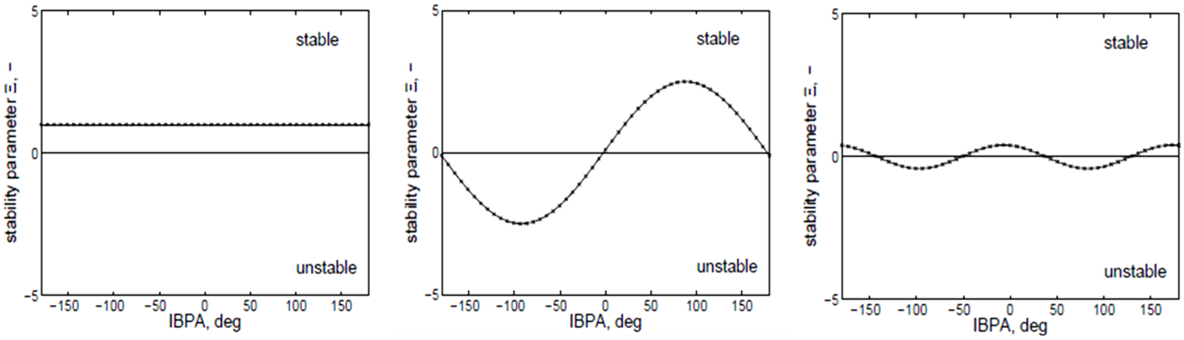

Figure 2.10: Influence of blade $0, \pm 1, \pm 2$ (from the left to the right)

By looking at influence coefficient values, it can be noticed that the influence of the vibrating blade in the row decays quickly away and is usually almost negligible after ± 2 blades [19]. The contribution from the blades ± 2 is generally of one order of magnitude less than the influence coefficient value associated to blades 0 and ± 1. Commonly the stability parameter has a characteristic S-shape, whose variation with respect to the inter-blade phase angle is single-period sinusoidal [20]. The S-curve shown in Figure 2.11 indicates that there might be a condition where the influence of the reference blade, which commonly has a stabilizing character, can be dominated by detrimental coupling influence of its neighbours and the whole blade row attains unstable conditions.

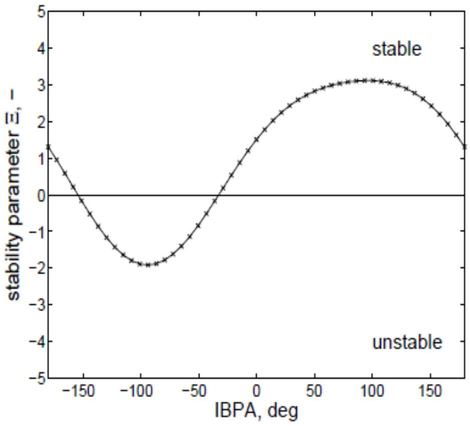

Figure 2.11: Characteristic stability curve

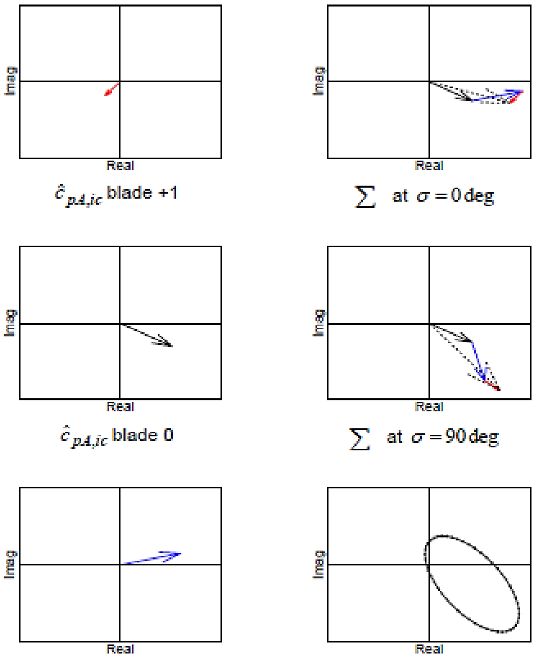

$\hat{c}_{pA,ic}$ blade +1

$\sum$ at $\sigma = 0\,\mathrm{deg}$

$\hat{c}_{pA,ic}$ blade 0

$\sum$ at $\sigma = 90\,\mathrm{deg}$

$\hat{c}_{pA,ic}$ blade -1

Loci of $\sum$ at
$\sigma = -180 \ldots +180\,\mathrm{deg}$

Figure 2.12: Polar graph and circle plot of the imaginary versus real component

3 OBJECTIVE

The proposed work herein aims at numerically investigating aerodynamic damping with focus on the first six mode shapes of the original VINK first rotor blades. Different numerical approaches currently available in ANSYS CFX software have been compared as well as the influence of several parameters on numerical predictions has been investigated.

Within the framework of a recently started H2020 project called ARIAS, a new test rig will be established at KTH. The purpose of the test facility is to generate a unique set of blade surface unsteady pressure data for validation of prediction models for aerodynamic damping in transonic compressor blades oscillating at high-reduced frequencies. The blade profile that will be used in the test rig originates from the NFFP6 project called VINK and is a 2D extrusion of a profile extracted at the 95% span of the rotor blades from the 3-stage high-speed transonic booster.

Based on the findings of the present work, different objectives will be attained:

- To broaden knowledge about mode shape sensitivity of VINK first rotor blades, with the main focus placed on investigations of unsteady surface pressure at different span locations. The investigation involves only numerical CFD simulations and can be considered as a continuation of previous aeroelastic studies conducted on the same 3-stage high-speed transonic booster;
- To provide useful data and predictions for the development of the oscillating cascade rig;
- To recommend the optimum placement of the pressure transducers for measurements of the aerodynamic response in the oscillating cascade rig;
- To get insights into different numerical setups evaluating eventual mismatches with respect to the successive experimental results.

4 TEST CASE DESCRIPTION AND PREVIOUS WORKS

The geometry under consideration in the present work is the first stage of VINK6 (Virtual Integrated Compressor), which is a transonic axial compressor composed of three booster stages. Previous aeromechanical studies were conducted on the same geometry, which have been used as starting point for this analysis.

4.1 Transonic compressor specifications

Two aircraft engines featuring $70\ klb$ of thrust at static conditions were considered as design target [21]. High efficiency and thus quite low aerodynamic loading was targeted for the high-speed booster located after the fan of each engine. In Table 4.1, design data for these first three stage are stated:

Table 4.1: High-speed booster performance data

Parameter	Value
$p_{0,23}$ [kPa]	46.69
$T_{0,23}$ [K]	282.4
$\dot{m}_{0,23}$ [kg/s]	42.68
π [-]	2.8
N [rpm]	6242
Deviation from ISA [K]	+10
Cruise altitude [kft]	35

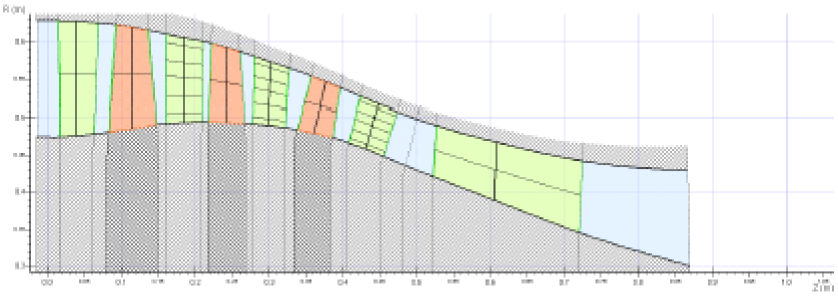

Figure 4.1: Compressor layout shown in the meridional view [21]

In Figure 4.1, it is possible to recognize the end-walls, the variable inlet guide vanes (VIGV), the three compression stages and the downstream strut (ICC). In Table 4.2, the number of blades for each stage of the high-speed booster is stated.

Table 4.2: VINK compressor blade count

Component	VIGV	R1	S1	R2	S2	R3	S3	ICC
Blade number	76	51	88	69	93	72	91	9

The focus of this work is on the first compressor stage. All data related to the latter one are summarized in Table 4.3 and 4.4 and these values have been used as the reference ones for the successive analysis.

Table 4.3: Thermodynamic parameters of the first compressor stage at the design point

Parameter	Value
Design pressure ratio	1.51
Design normalized mass flow	89.5 kg/s
Design polytropic efficiency	91%
Surge Margin at Design point	16.6%

Table 4.4: Blade geometry of the first compressor stage

Parameter	R1	S1
Chord at mean radius	98.3 mm	55.2 mm
Axial chord at mean radius	54.7 mm	49.2 mm
Aspect ratio	1.22	1.90

The aspect ratio of the blade is a geometric design parameter defined as:

$$Aspect\ ratio = \frac{b}{c} \tag{4.1}$$

where b is the blade height and c is the blade chord.

4.2 Aeromechanical assessment

The first stage of the high-speed booster was evaluated with respect to mechanical stresses after the design step [21]. Several structural analyses were performed in order to assess the blade strength under the centrifugal, aerodynamic and thermal loads at the design point. The material chosen for the rotor blades was a titanium alloy (Ti-6Al-4V). The pre-stressed blades were then subjected to modal analysis to produce the blade mode shapes. In this initial analysis, only the blade modes were considered, while the disk was not included. Potential resonances originating from the blade row interactions were monitored in a Campbell diagram over the entire operating range of the high-speed compressor.

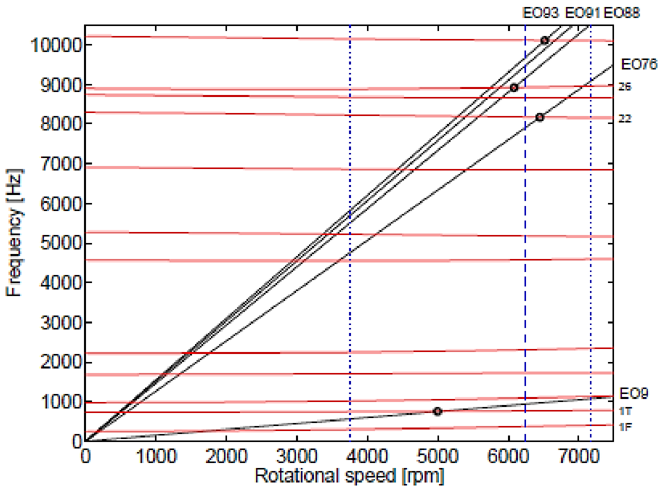

Figure 4.2: Campbell diagram for the first stage rotor blades (R1) [21]

From the Campbell diagram in Figure 4.2, it is possible to notice that no dangerous resonance crossings could be identified for the lower mode shapes except for the EO9 line. The latter one corresponds to the 9 ICC blades located in the downstream duct between the booster and HPC (high pressure compressor) and crosses the first torsion mode at about $5000\ rpm$ (80% of the nominal rotor speed). However, the position of the ICC struts is far downstream from rotor 1, thus the aerodynamic influence of these can be neglected. The potential dangerous crossings resulting from the adjacent blade row interaction might occur at higher frequencies and involve higher order mode shapes, such as modes 22 and 26 indicated in the diagram.

To assess the flutter stability of the optimized rotor blades, aerodynamic damping predictions were carried out for the two lowest mode shapes (1F and 1T). Considering a blisk configuration of the rotor, which features low structural damping, aerodynamic damping predictions are a vital for the investigation of aeromechanical stability. Steady-state flow simulations and linearized unsteady flow simulations were performed. The flow model used is the 3D URANS flow equations with the Spalart-Allmaras turbulence model, linearized for the unsteady flow simulations. The aerodynamic damping coefficient Θ is expressed as negative aerodynamic work per cycle W_{aero} normalized with the oscillation amplitude, as shown in the formula above:

$$\Theta = \frac{-W_{aero}}{\pi b h_{max}^{2} p_{ref}} \tag{4.2}$$

where b is the blade height and h_{max} is the maximum blade mode shape amplitude. The reference dynamic pressure is $p_{ref} = p_0 - p_1$, where p_0 is the average total inlet pressure and p_1 is the average static inlet pressure. In Figure 4.3, the distribution of aerodynamic damping as function of nodal diameter for the first two mode is shown.

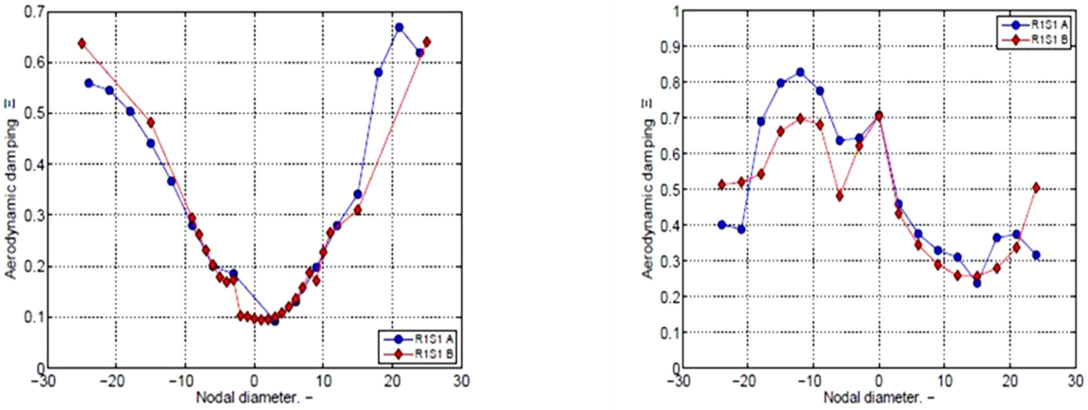

Figure 4.3: Aerodynamic damping curve for mode 1 (on the left side) and mode 2 (on the right side)

Aerodynamic damping curves for the first bending mode (1F) are rather similar for the optimized and reference geometries. The least stable mode is identified at $ND = 3$ and features an aerodamping coefficient of 0.094, which is a relatively small value. However, the rotor blades remain stable (positive aerodynamic damping) for all nodal diameters. The aerodamping curves for the first torsion (1T), instead, are slightly more different from each other, but the damping value of the least stable mode has not changed significantly comparing the two geometries. In this case, the aerodamping values for the 1T mode are higher than the ones for the 1F mode, thus 1T mode is safer from an aeromechanical stability viewpoint.

4.3 Previous work on VINK6 blading

Unsteady flow solutions and comparisons of the first three modes at design throttle and 70% speed were analysed for the first rotor in another study carried out at KTH [22]. The first mode shows the least stable mode at $ND = 3$, the second mode is least stable at $ND = 9$ and the third mode at $ND = -6$. The S-curve peak to peak amplitude appears largest for the second mode but similar to the first mode. The third mode denotes only a small peak to peak amplitude. Unsteady blade surface pressure amplitude of the least stable mode showed a similar behaviour for all three modes, mainly the magnitude varies between the different modes. First mode featured a more stable pressure on the blade surface with a low pressure amplitude, while second and third mode denoted a three to four times higher peak at the leading edge.

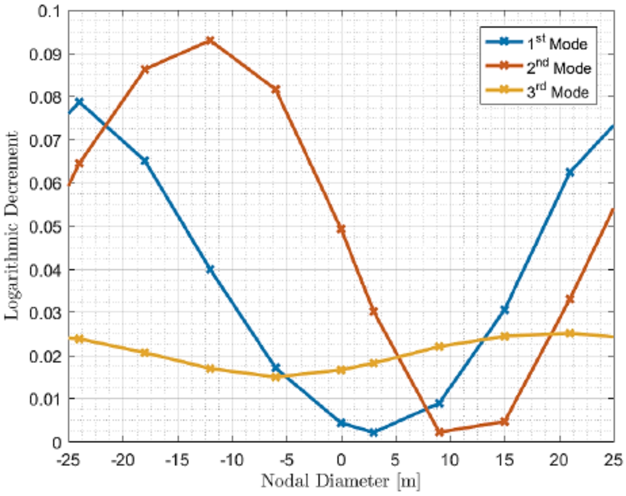

Figure 4.4: S-curve for the first three modes at design throttle and 70% speed

5 NUMERICAL METHODS

The focus of this work is on numerical techniques aiming to solve fluid flow field around compressor blades, since the structural problem can be solved separately as previously mentioned. In turbomachinery, modeling in frequency domain is usually used to predict the unsteady aerodynamics. The unsteady flow is in fact a non-linear phenomenon, but switching from time domain to frequency domain, linear unsteady flow can be assumed and this simplifies the resolution strategy. The flow can be decomposed into two parts, which are the steady flow and an unsteady linear perturbation, which in relative terms is considered less significance in value. Stationary flow is described by partial non-linear differential equations, while flow perturbation is modelled with a series of partial differential equations with linear coefficients, which turn out to be hyperbolic over time. Without losing accuracy and knowing that the unsteady flow is periodic over time, Fourier transformation can be computed involving space-dependent complex coefficients. Each coefficient is described by a series of partial differential equations, where time does not appear explicitly, making these equations linearized. Essentially the equation systems obtained from this analysis require a low computational cost without resulting in an incorrect calculation of the fluid dynamic parameters.

5.1 Computational environment

ANSYS CFX [23] is a three-dimensional finite volume method based time-implicit Navier-Stokes equation solver. A control volume is constructed around each vertex of the mesh (structured, unstructured or hybrid) elements and fluxes are computed at the integration points on the faces of these control volume [24]. The discretized equations are then solved using a bounded high-resolution advection scheme similar to Barth and Jesperson [25]. Pressure velocity coupling is carried out using the 4th order pressure smoothing Rhie and Chow algorithm [26]. Discretized equations are then solved using the coupled algebraic multi-grid method developed by Hutchinson and Raithby [27], and Raw [28]. Numerical effort of this method scales linearly with the number of grid nodes in the computational domain. Steady state calculations are performed using a pseudo-time marching approach until user defined convergence is reached. For unsteady calculations, an iterative procedure updates the non-linear coefficients within each time step while the outer loop advances the solution in time for time integration setup. Reynolds stresses can be computed by different turbulence methods.

5.2 Use of RANS equations and turbulence models

Navier-Stokes equations are partial differential equations describing a flow field from a macroscopic viewpoint. Hypothesis behind this formulation assume that the fluid is modeled as a deformable continuum and is Newtonian (viscosity remains constant regardless fluid velocity). Using a Cartesian coordinate system, continuity and Navier-Stokes equations can be written in the following compact form [29]:

$$div(u) = 0 \tag{5.1a}$$

$$\frac{\partial u}{\partial t} + div(uu) = -\frac{1}{\rho}\frac{\partial p}{\partial x} + u(divgrad(u)) \tag{5.1b}$$

$$\frac{\partial v}{\partial t} + div(vu) = -\frac{1}{\rho}\frac{\partial p}{\partial y} + vdiv(grad(v)) \tag{5.1c}$$

$$\frac{\partial w}{\partial t} + div(wu) = -\frac{1}{\rho}\frac{\partial p}{\partial z} + vdiv(grad(w)) \tag{5.1d}$$

In turbulent regime, equations (5.1) are not used in the above mentioned form because the computational calculation would require an excessive cost. In fact, on industrial scale it is usually not necessary to model exactly the turbulence phenomena, hence simplified formulation such as averaged Navier-Stokes equations are more convenient. The latter equations describe the flow field as the sum of a stationary contribution and a fluctuation contribution over time. For the sake of simplicity in the following related math, the fluid is considered incompressible and features constant viscosity but the final outcomes can be extended to the general case. Any property of the fluid ψ can be written as a sum of its average value and its fluctuating part:

$$\psi = \Psi + \psi' \tag{5.2}$$

where by definition the fluctuating part has time mean value that is zero. It is possible to substitute the average and fluctuating components in equations (5.1) to obtain the following formulation:

$$div(u) = div(U) \tag{5.3a}$$

$$\frac{\partial U}{\partial t} + div(UU) + div\overline{(u'u')} = -\frac{1}{\rho}\frac{\partial P}{\partial x} + vdiv(grad(U)) \tag{5.3b}$$

$$\frac{\partial U}{\partial t} + div(VU) + div\overline{(v'u')} = -\frac{1}{\rho}\frac{\partial P}{\partial y} + vdiv(grad(V)) \tag{5.3c}$$

$$\frac{\partial U}{\partial t} + div(WU) + div\overline{(w'u')} = -\frac{1}{\rho}\frac{\partial P}{\partial z} + vdiv(grad(W)) \tag{5.3d}$$

By comparing equations (5.3) and (5.1), except for the mass conservation, a new term appears in each new equation. These additional contributions, which are the product of two fluctuating velocities, derive from turbulent vortices and are called Reynolds stresses. These stresses are null only if the two components of fluctuating velocity are both random and independent of each other. In most cases, this never happens and, on the other hand, these terms are very high compared to purely viscous stress. Equations (5.3) are referred to as RANS equations. If the average fluctuation in time does not exceed 5%, then the density variation is not important up to Mach number equal to 3 or 5. If the threshold value is exceeded, starting from Mach number equal to 1 there are important variations in density and after integrating average and fluctuating terms in time (Favre averaging), RANS equations for a compressible fluid are obtained:

$$\frac{\partial \bar{\rho}}{\partial t} + div(\bar{\rho}\tilde{U}) = 0 \tag{5.4a}$$

$$\begin{aligned}\frac{\partial \bar{\rho}\tilde{U}}{\partial t} + div(\bar{\rho}\tilde{U}\tilde{U}) = -\frac{\partial \bar{P}}{\partial x} + div\left(\mu grad(\tilde{U})\right) + \\ + \left[-\frac{\partial \bar{\rho}\overline{u'^2}}{\partial x} - \frac{\partial \bar{\rho}\overline{u'v'}}{\partial y} - \frac{\partial \bar{\rho}\overline{u'w'}}{\partial z}\right] + S_{Mx}\end{aligned} \tag{5.4b}$$

$$\begin{aligned}\frac{\partial \bar{\rho}\tilde{V}}{\partial t} + div(\bar{\rho}\tilde{V}\tilde{U}) = -\frac{\partial \bar{P}}{\partial y} + div\left(\mu grad(\tilde{V})\right) + \\ + \left[-\frac{\partial \bar{\rho}\overline{u'v'}}{\partial x} - \frac{\partial \bar{\rho}\overline{v'^2}}{\partial y} - \frac{\partial \bar{\rho}\overline{u'w'}}{\partial z}\right] + S_{My}\end{aligned} \tag{5.4c}$$

$$\frac{\partial \bar{\rho}\widetilde{W}}{\partial t} + div\left(\bar{\rho}\widetilde{W}\widetilde{U}\right) = -\frac{\partial \bar{P}}{\partial z} + div\left(\mu grad\left(\widetilde{W}\right)\right) + \tag{5.4d}$$

$$+\left[-\frac{\partial \bar{\rho}\overline{u'^2}}{\partial x} - \frac{\partial \bar{\rho}\overline{u'v'}}{\partial y} - \frac{\partial \bar{\rho}\overline{w'^2}}{\partial z}\right] + S_{Mz}$$

To mathematically close the equation system it is necessary to add further equations to equation (5.4), represented by turbulence models. The computational cost increases with the number of extra equations used. Table 5.1 provides a quick overview of the main turbulence model used and the number of equations added.

Table 5.1: Turbulence models

Number of equations	Turbulence model
0	Mixing length model
1	Spalart-Allmaras model
2	k-epsilon
2	k-omega
2	Algebraic stress model
7	Reynolds stress model

One of the most used turbulence models in turbomachinery is certainly the SST model, conceived by Menter [30]. This turbulence model is a hybrid combination of k-epsilon and k-omega models. The first one is used in the vicinity of the walls, while the second one is used in the completely turbulent area and thus away from the wall. The k equation is the same one used by k-epsilon model, but this equation is transformed into the equation of ω by substituting $\epsilon = k\omega$. Hence, the formulation of the model is the following one:

$$\frac{\partial(\rho\omega)}{\partial t} + div(\rho\omega U) = div\left[\left(\mu + \frac{\mu_t}{\sigma_{\omega,1}}\right) grad(\omega)\right] + \tag{5.5}$$

$$+\gamma_2\left(2\rho S_{ij}S_{ij} - \frac{2}{3}\rho\omega\frac{\partial U_i}{\partial x_j}\partial_{ij}\right) - \beta_2\rho\omega^2 \ + 2\frac{\rho}{\sigma_{\omega,2}\omega}\frac{\partial k}{\partial x_k}\frac{\partial \omega}{\partial x_k}$$

Furthermore, blending functions are inserted into the turbulence model, which ensure the smooth passage between the developed turbulence zone and the one near the wall. In fact, in the computational stage the use of a single equation may cause in some cases a serious numerical instability. In the present work, k-epsilon and SST model are used both for steady and unsteady computations in order to investigate their influence on the predictions.

5.3 Fourier transformation method

Improvements in coupled CFD-FEM methods and the increase in affordable computational power have provided significant progress enabling developments of codes dedicated for specific purposes. Traditional methods involved simulations of the unsteady flows around many blades in a given row as function of the analyzed nodal diameters. Most recently more efficient computational methods have been implemented so as to capture aerodynamic phenomena with simulations of only one or two blades for each row yet yielding the full sector solution. This provides considerable savings in computing time and machine resources. All these methods are based on Fourier Transformation, which preserves frequencies occurring across the periodic surfaces [31]. Fourier Transformation (FT) method is based on phase shifted periodic boundary condition. The basic principle is that the pitchwise boundaries are periodic to one another at different instances in time. The method was modified to avoid storing the signal for a full time period on all pitchwise boundaries by using temporal Fourier series decomposition and double time and azimuthal Fourier series decomposition at the rotor-stator interface. A periodic function can be expressed as summation of Fourier series coefficients, as mathematically written below:

$$f(t) = \sum_{m=-M}^{M} A_m e^{-i\omega t} \tag{5.6}$$

The time-varying signal is decomposed into harmonics of fundamental frequency $(\omega/2\pi)$ and only Fourier coefficients (A_m) need to be stored to reconstruct the solution at an arbitrary time. FT method uses a double passage approach, where Fourier coefficients are collected at the interface between two adjacent passages, capturing a high quality time signal far from the phase shifted periodic boundaries where the signal is imposed.

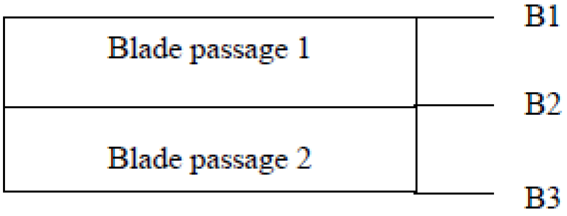

Figure 5.1: Double passage model

For stability analysis, the time shift between adjacent vibrating blades is given as:

$$\Delta T = \frac{ND}{\omega} \tag{5.7}$$

The signal $f_{B1}(t)$ on $B1$ side in Figure 5.1 is equal to signal on $B2$ side, phase shifted by $t + \Delta T$.

$$f_{B1}(t) = f_{B2}(t + \Delta T) \tag{5.8}$$

The signal $f_{B3}(t)$ on $B3$ side in Figure 5.1 is equal to signal on $B2$ side, phase shifted by $t - \Delta T$.

$$f_{B3}(t) = f_{B2}(t - \Delta T) \tag{5.9}$$

where $f_{B2}(t)$ is the reconstructed signal at $B2$ interface using the accumulated Fourier coefficients on the same boundary.

5.4 Harmonic balance analysis

When the unsteady motion assumes a greater importance, then solutions obtained by the linearized equations may not be representative of the investigated flow field. Therefore, in that case it might be necessary to apply a different numerical approach, such as the harmonic balance method, which is able to model harsh conditions of shock waves and sharp separation of the boundary layer, to get better numerical predictions. For the sake of simplicity in the following related math, the fluid is considered two-dimensional, non-viscous, non-conductive and with constant specific heat. The flow can be then modeled through two-dimensional Euler's equations [32]:

$$\frac{\partial U}{\partial t}+\frac{\partial F(U)}{\partial x}+\frac{\partial G(U)}{\partial y}=0 \tag{5.10}$$

Conservation variables and flux terms present in equation (5.10) can be expressed as follows:

$$U=\begin{bmatrix}\rho\\ \rho u\\ \rho v\\ pe\end{bmatrix}\quad F=\begin{bmatrix}\rho u\\ \rho u^2+p\\ \rho uv\\ \rho uh\end{bmatrix}\quad G=\begin{bmatrix}\rho v\\ \rho uv\\ \rho v^2+p\\ \rho vh\end{bmatrix} \tag{5.11}$$

In equations (5.11) velocity, density, pressure and total enthalpy terms appear. By considering the flow temporally periodic, equation (5.12) can be written:

$$U(x,y,t)=U(x,y,t+T) \tag{5.12}$$

where T represents the period of the unsteadiness. Space periodicity requires that the following condition is met:

$$U(x,y+G,t)=U(x,y,t+\Delta T) \tag{5.13}$$

where G is the blade pitch and ΔT is time interval related to $IBPA$. For a given frequency and given $IBPA$, the period is defined as $T=2\pi/\omega$ and thus the time interval related to $IBPA$ is defined as $\Delta T=IBPA/\omega$. Since the flow is periodic in time and in space, then the variables can be written in Fourier series, where the coefficients are space-dependent functions.

$$\rho(x,y,t)=\sum_n R_n(x,y)e^{i\omega nt} \tag{5.14a}$$

$$\rho u(x,y,t)=\sum_n U_n(x,y)e^{i\omega nt} \tag{5.14b}$$

$$\rho v(x,y,t)=\sum_n V_n(x,y)e^{i\omega nt} \tag{5.14c}$$

$$\rho e(x,y,t)=\sum_n E_n(x,y)e^{i\omega nt} \tag{5.14d}$$

In equations (5.14) summations are truncated to a finite number of terms ranging between $\pm N$. In the definition of enthalpy and pressure, implicitly used in equation (5.10), the density can appear at the denominator of each term. Expressing the latter one in Fourier series, it is possible to obtain:

$$\frac{1}{\rho(x,y,t)}=\sum_n \Gamma_n(x,y)e^{i\omega nt} \tag{5.15}$$

If equation (5.14a) is combined with equation (5.15), the following result is obtained:

$$\rho\cdot\frac{1}{\rho}=\left[\sum_n R_n(x,y)e^{i\omega nt}\right]\otimes\left[\sum_m \Gamma_n(x,y)e^{i\omega nt}\right]=1 \tag{5.16}$$

To satisfy equation(5.16) it is necessary, except for the null-frequency terms ($n + m = 0$), that the series coefficients are null. For example, if the force is modeled with N = 2 harmonics, one can get the following system to solve:

$$\begin{bmatrix} R_0 & R_{-1} & R_{-2} & 0 & 0 \\ R_1 & R_0 & R_{-1} & R_{-2} & 0 \\ R_2 & R_1 & R_0 & R_{-1} & R_{-2} \\ 0 & R_2 & R_1 & R_0 & R_{-1} \\ 0 & 0 & R_2 & R_1 & R_0 \end{bmatrix} \begin{bmatrix} \Gamma_{-2} \\ \Gamma_{-1} \\ \Gamma_0 \\ \Gamma_1 \\ \Gamma_2 \end{bmatrix} = \begin{bmatrix} 0 \\ 0 \\ 1 \\ 0 \\ 0 \end{bmatrix} \tag{5.17}$$

The system obtained in matrix equation (5.17) must also be obtained for mass, energy and momentum conservation equations. Basically, for each written equation, terms can be grouped for frequency order and each group can be placed in an equation equal to zero. It is possible to group all the equations formulated, using the following vector notation:

$$\frac{\partial \tilde{F}(\tilde{U})}{\partial x} + \frac{\partial \tilde{G}(\tilde{U})}{\partial y} + \tilde{S}(\tilde{U}) = 0 \tag{5.18}$$

where in equation (5.18) vectors $\tilde{U}$ and $\tilde{S}$ can be written again as:

$$\tilde{U} = \begin{bmatrix} R_0 \\ U_0 \\ V_0 \\ E_0 \\ R_1 \\ U_1 \\ V_1 \\ E_1 \\ \dots \end{bmatrix} \qquad \tilde{S} = i\omega \begin{bmatrix} R_0 \\ U_0 \\ V_0 \\ E_0 \\ R_1 \\ U_1 \\ V_1 \\ E_1 \\ \dots \end{bmatrix} \tag{5.19}$$

while $\tilde{F}$ and $\tilde{G}$, more complicated to write, can however be defined as non-linear functions of the Fourier series coefficients for the conservation variables $\tilde{U}$. Since $\tilde{U}$ is composed by real quantities, then the conjugate complex of the U_N must be equal to the quantity U_{-N}. The problem is now simplified because Fourier harmonic terms vary only for $N > 0$. If we assume that the sufficient number of harmonics to describe the problem is N, then for each variable we must store N coefficients for the real part, N coefficients for the complex part and one for the constant term. In total $2N + 1$ terms for each variable have to be calculated. Thus, the computational cost of this method requires the resolution of N^3 operations, so the algorithm can be very heavily weighted by increasing the number of harmonics describing the problem. Moreover, for viscous flows, the equations of turbulence are not quickly modeled in the algebraic form and this creates considerable inconveniences. To avoid this number of problems, one could think of constructing $\tilde{F}$, $\tilde{G}$ and $\tilde{U}$ by evaluating the temporal behavior of U, F and G in the equally spaced points over a period of time. In practice (5.20) can be written:

$$\tilde{U} = EU^* \tag{5.20}$$

where U^* is the vector of conservation variables in the $2N + 1$ equally spaced points, while E is the discrete matrix of Fourier transformation. Replacing equation (5.20) within equation (5.18), the following expression is obtained:

$$\frac{\partial EF^*}{\partial x} + \frac{\partial EG^*}{\partial y} + i\omega NEU^* = 0 \tag{5.21}$$

where in equation (5.21) N is a diagonal matrix in which every N entry corresponds to the N harmonic. By pre-multiplying equation (5.21) for the inverse of the matrix E, the third term assumes the following form:

$$i\omega E^{-1}NEU^{*} = S^{*} \approx \frac{\partial U^{*}}{\partial t} \tag{5.22}$$

In this way the spectral operator coming before the term U^{*} can be approximated with the operator $\partial/\partial t$. The final expression of Euler's equations, using the harmonic equilibrium method, is reduced to:

$$\frac{\partial F^{*}}{\partial x} + \frac{\partial G^{*}}{\partial y} + S^{*} = 0 \tag{5.23}$$

Using the discrete matrix of the Fourier transformation, the flow can be resolved more easily. Moreover, the method can be used not only to solve the Euler equations, but also to find a solution for Navier-Stokes equations that was not allowed by equation (5.18). A pseudo-temporal term must be introduced in order to solve the problem with the aid of conventional CFD techniques. Basically, equation (5.23) turns into (5.24):

$$\frac{\partial U^{*}}{\partial \tau} + \frac{\partial F^{*}}{\partial x} + \frac{\partial G^{*}}{\partial y} + S^{*} = 0 \tag{5.24}$$

where the term τ is seen as a dummy temporal variable. Now it is possible to use the classic method of "time-marching" to obtain a stationary solution, thus canceling the dummy term. Note that the pseudo-temporal harmonic equilibrium equation is very similar to Euler equation (5.10), with the difference that to calculate the value of S^{*} the spectral operator is used. In this way the number of operations is reduced to the order N^{2} and for the computation of the flux vector only N operations are required.

6 METHODOLOGY AND DESCRIPTION OF THE MODELS

The current work has been formulated in order to numerically investigate aerodynamic damping analyzing several mode shape influence. ANSYS CFX 19.2 is the commercial 3D CFD code employed for the whole project as tool to pre-process, solve and post-process the unsteady aerodynamic field in the transonic blade row. This code is based on three dimensional finite volume method and features a time-implicit Navier-Stokes equation solver, as aforementioned.

Three different CFD meshes generated in ANSYS TurboGrid were provided from previous studies on the same rotor blading. Hence, a sensitivity study is conducted by performing steady-state simulations in order to get mesh independence and choose the optimal refinement level. Two different turbulence models are tested for the purpose of studying how the numerical setup affects numerical predictions. Several steady blade loading curves has been compared and the optimal setups has been selected to proceed to the successive steps. From the entire first stage solution, inlet and outlet properties over the first rotor are extracted in order to carry out simulations of this rotating blade row.

Unsteady simulations has been performed on the first rotor blade row by using transient blade row model with the use of Fourier transformation method, which has the property to be frequency preserving and hence suitable for the present task. The latter method enables simulations of only two blades per row yet yielding the full sector solution and thus providing considerable savings in computing time and machine resources. Deformation of the blade was computed from a mechanical pre-stressed modal analysis for the mode shapes under consideration. Consequently, blade displacements for each mode have been prescribed for the CFD mesh and the aerodynamic flow field is solved separately. The approach employed to predict aerodynamic damping is the energy method and, after periodic unsteady solutions have been obtained, logarithmic decrement values are calculated based on the predicted blade forces and the specified blade motion for a range of nodal diameters. Simulation results have been further processed so as to assess the validity of the numerical setup extracting unsteady surface pressure coefficient, local work coefficient and several convergence studies. Time integration and harmonic balance methods are compared in order to find the optimal agreement between CPU time and prediction reliability.

6.1 Spatial discretization

In order to conduct investigations, it is necessary to define a domain and this one must comply with some quality requirements. Meshes for this study were generated in ANSYS TurboGrid. The meshing method is based on O-type mesh around blades, such as around rotor and stator blades, and H-type in other areas, such as for the plenum domain, with automatic topology optimization. Fluid elements are hexahedral in all the cases. The boundary layer resolution is important as it is an identification of an adequate mesh. In this case, a non-dimensional wall distance of $y^+ > 10$ is implemented. A mesh sensitivity study is performed at each stage to achieve a grid independent flow solution. After computing first stage steady-state solution, the medium mesh with k-epsilon turbulence model has been chosen, due to the similar results obtained using the finest mesh with same turbulence model, but with a substantial decrease in CPU time. For simulations using SST (Shear Stress Transport) turbulence model instead the finest mesh is used due to a poorer agreement between steady-state results obtained for the whole stage. In Table 6.1 details about different mesh sizes used in this study are shown. In Figure 6.1 the different mesh densities and grid types can be compared. These meshes are used for steady and unsteady computations both.

Table 6.1: Mesh specifications (node count) for the first compressor stage

Mesh Size	Inlet Plenum	Rotor 1 (R1)	Stator 1 (S1)
Coarse	7350	100200	98056
Medium	20700	249182	205841
Fine	29700	400785	445968

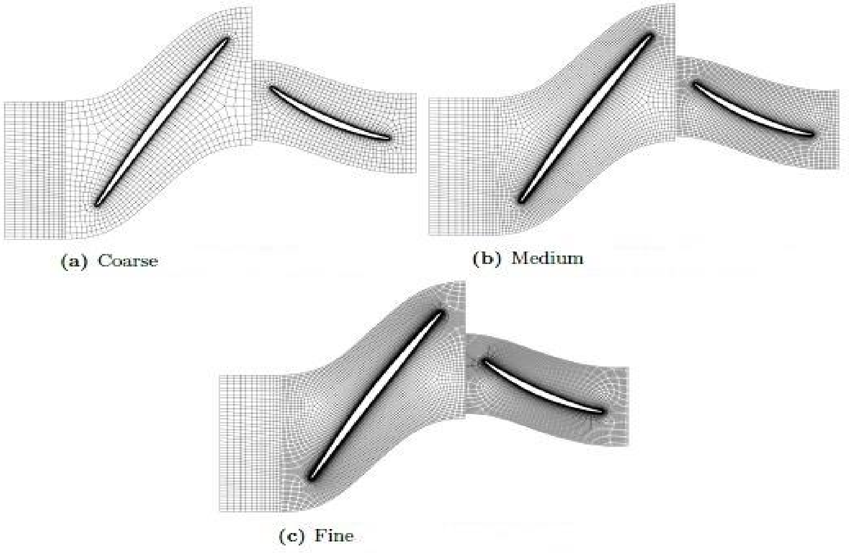

Figure 6.1: Comparison of different mesh refinements for the first compressor stage

6.2 Steady-state modeling

To obtain the aerodynamic damping of the first compressor rotor, a steady state investigation is the first step to perform. Hence, mesh domains presented in the above section have been modelled in order to set up steady-state simulations. A steady-state solution must be computed so as to be sure that the meshes are set correctly and the solution is converging to meaningful values. This steady-state solution is thus used both for a brief analysis of the transonic compressor blade row in steady conditions at design operating condition and as the initial values needed to run successive unsteady simulations. A single rotor and stator passage is used for these calculations, using a periodic boundary condition to account for the number of blade passages, which are 51 for this blade row. An inlet plenum is placed upstream the rotor passage in order to apply the inlet boundary condition. The model used for the steady state calculation is shown in Figure 6.3. Inflow conditions are specified in terms of total pressure, total temperature and velocity directions. Turbulence intensity has been set to 5% and turbulent length scale has been specified as equal to $1\ mm$. Radial distribution of total temperature, total pressure and velocity vectors at the inlet were obtained from calculations carried out in the earlier design phase [21]. Transition is not modeled and the flow is considered fully turbulent on all surfaces. The value of the inlet total temperature is constant along the span and equal to $282.4\ K$, while the static pressure at the outlet is set equal to $57200\ Pa$. Trends of the other inlet boundary conditions along the span are shown in Figure 6.2.

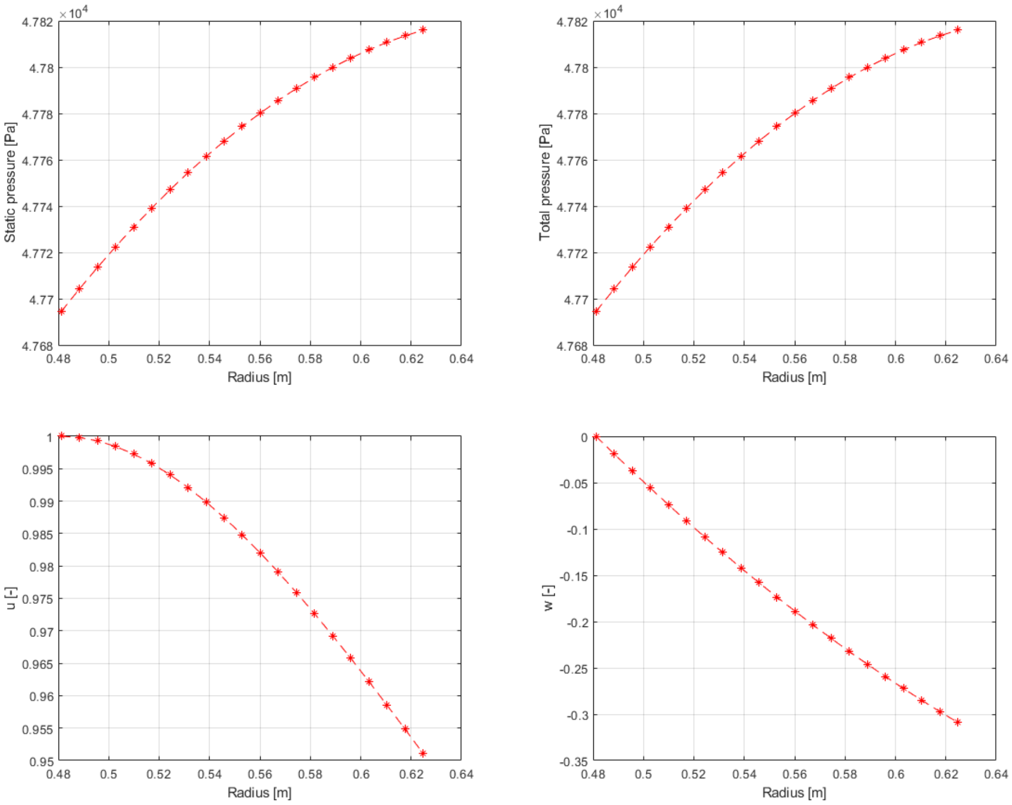

Figure 6.2: Total pressure, static pressure and velocity component trend at the machine inlet used as boundary conditions

Numerical setup in Table 6.2 is the one setting up in ANSYS CFX-Pre, which is the pre-processing software used in the present investigation. SST and k-epsilon turbulence models both are utilized in order to compare their influence on the steady-state blade loading. Fluxes at the interfaces between two different domains are pitch-averaged and transported by using the so-called mixing planes. Moreover, there are two implementations of mixing planes in CFX, referred to as constant total pressure and stage average velocity respectively. The first option has been selected since it assumes no pressure losses over the change of the reference frame, which would incur in the second case. After obtaining the solution for the first stage, inlet and outlet properties over the first rotor are extracted from CFD-post in the stationary frame of reference and are applied for first rotor simulations. Once validating the blade loading curve for the latter case with respect to stage blade loading curve, unsteady simulation can be directly performed on this rotating blade row avoiding modelling complications at the interface. K-epsilon turbulence model is chosen primarily because of its wide application in turbomachinery flows and convergence issues related to k-omega model, whose manifestation is SST model. In the first rotor, in fact, it has been necessary to modify an expert parameter (lowering tangential vector tolerance value) for computations with SST model in order to find the solution. On the other hand, SST model is recommended for accurate boundary layer simulations, but to benefit from this model, a resolution of the boundary layer of more than 10 points is required. For free shear flows, the SST model is mathematically identical to the k-epsilon model, but it exaggerates flow separation from smooth surfaces under the influence of adverse pressure gradients [23]. More into detail, SST model make use of k-omega model for boundary layer problems, where the formulation works from the inner part through the viscous sub-layer until the walls. Then the formulation switches to a k-epsilon behavior in the free-stream, which avoids the sensitivity to the inlet free-stream turbulence properties typical problem of k-omega model. In other words, this model can account for the transport of the principal shear stress in adverse pressure gradient boundary layers.

Table 6.2: Numerical setup of Stage 1 and Rotor 1 for steady-state simulation

Blade row configuration	Stage 1 (Plenum, Rotor 1, Stator 1)	Rotor 1
Material	Air Ideal Gas	
Heat transfer model	Total Energy	
Turbulence model	k-epsilon and SST	
Advection scheme	High resolution	
Turbulence numerics	First order	
Walls	Adiabatic – No slip Walls	
Reference pressure	0 atm	
Angular velocity	-6242 rpm	
Interfaces		
Plenum to Rotor 1	Mixing plane (constant total pressure)	-
Rotor 1 to Stator 1	Mixing Plane (constant total pressure)	-
Inlet Boundary Condition	Total pressure, Total temperature, Velocity components, Turbulence Kinetic Energy and Dissipation (Medium 5%)	Total pressure, Total temperature, Velocity components (Stationary Frame)
Outlet Boundary Conditions	Static Pressure	
Convergence criteria	1e-08	
Max iterations	700	

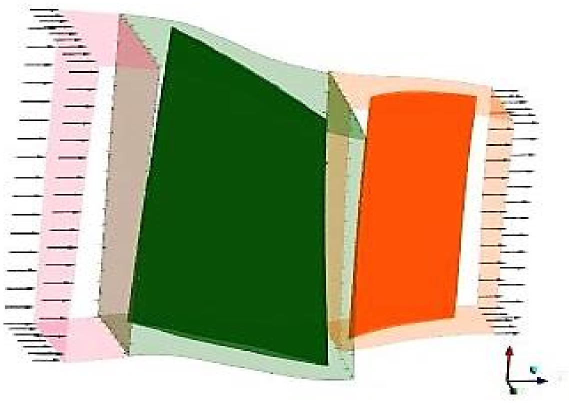

Figure 6.3: Model of plenum, rotor and stator for steady-state calculations

6.3 Transient blade row modeling

Transient blade row models available in ANSYS CFX [23] are:

- Profile Transformation (PT) method, which overcomes the unequal pitch problem by scaling the flow profile across the blade row interfaces;
- Time Transformation (TT) method, which overcomes the unequal pitch problem by applying a time transformation to the flow equations. This transformation enables the use of simple periodic boundary conditions on the pitchwise boundaries;
- Fourier Transformation (FT) method, which uses a phase-shifted boundary condition with Fourier data compression to account for the unequal pitch between blade rows.

Unlike the time transformation pitch-change method, the Fourier transformation pitch-change method does not have any known limitations on the pitch ratio and works with both compressible and incompressible flows. The Fourier transformation method can be used in cases involving:

- Rotational flow boundary disturbances;
- Blade flutter (or forced response);
- Transient rotor stator interactions (single stage only).

Blade flutter and damping calculations can be performed in ANSYS CFX by solving for flow over vibrating blades with prescribed blade displacements. Blade flutter usually occurs at the natural frequency of the blade-disc assembly. This natural frequency can be determined along with blade displacements (mode shapes), using ANSYS Mechanical APDL prior to performing a flow analysis on the blade. In general, the natural disc frequency of a rotor-disc assembly consists of many mode shapes and only first six modes has been analyzed in this study. For blade flutter calculations, it is important to consider the aerodynamic effects of adjacent blades. For a rotor-disc assembly consisting of given blade number, there is a finite number of disc nodal diameters. At nodal diameter $ND = 0$, all the blades vibrate in phase with an $IBPA = 0$. However, for other nodal diameters, each blade will be out of phase with respect to the others by a finite Inter-Blade Phase Angle value. The inter-blade phase angle can be computed from the nodal diameter, as previously shown in equation (2.5). Starting from one-passage model in the steady state case it is necessary to create a two-passage model in order to apply the phase-shifted boundary conditions, typical of Fourier transformation method. The double passage is set while importing the mesh into ANSYS CFX-Pre. An additional internal interface between the two passages is created, which is necessary to store time step information during every simulation.

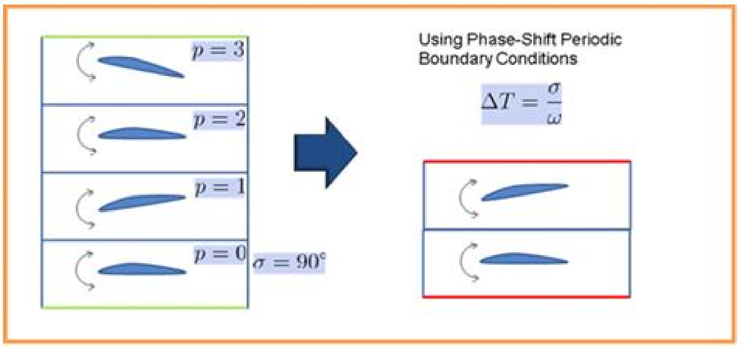

Figure 6.4: Application phase-shifted boundary conditions to a blade flutter case [23]

The main objective of a blade flutter analysis is to obtain the aerodynamic damping, or work per vibration cycle. Once a transient periodic solution is achieved, the energy balance method is used to perform the logarithmic decrement calculation. This calculation yields a measure of the system stability at each nodal diameter and blade vibration frequency. The work per vibration cycle is computed in ANSYS CFX as:

$$W_{cycle} = \int_{t_0}^{t_0+T} \int_{A} p\vec{v} \cdot \hat{n} dA dt \tag{6.1}$$

where $T = 2\pi/\omega$ is the period of one vibration cycle, t_0 is the initial time of the vibration cycle, ω is the vibration frequency, p is the fluid pressure, v is the velocity of the blade due to the prescribed structural displacements, A is the blade surface and $\hat{n}$ is the normal surface vector. Positive values for aerodynamic work indicate that the vibration is damped, while negative values indicate that the vibration is undamped for the frequency being studied. This convention is opposite to the one stated for the energy method in the theoretical approach. In CFX-Solver aerodynamic damping monitors can be used to monitor aerodynamic damping during a run. The monitor value is calculated according to equation (6.1). Other monitors can be set for checking the evolution in time of desired quantities. In this case, torque for both blade has been monitored, which has been used to check the convergence level of each simulation.

6.4 FEM structural analysis

After defining all the geometrical and material properties, a pre-stressed modal analysis was carried out with ANSYS Mechanical APDL on a single rotor blade using fixed support at the hub and cyclic symmetry displacement boundary conditions. Natural frequencies (eigenvalues) and mode shapes (eigenmodes) used in this investigations were yielded from this previous FEM analysis. The first six mode shapes data have been exported into a .csv file format, which is used as profile data function initialized in unsteady simulation. It is important to consider that the .csv file extracted must contain the following values as ANSYS CFX will make use of them:

- maximum displacement and natural frequency of the mode under consideration;
- nodal coordinates in X, Y and Z;
- displacements in X, Y and Z direction for each node and its correspondent node identification;
- a sector tag identifier, which results from expanding the original displacement values in order to take into the account the double passage needed for the unsteady CFD simulation.

Only the displacements of external nodes has been extracted from the FEM analysis, since interactions between fluid and blade surface are analyzed. In this way, it possible to reduce the computational effort as the mesh results lightened. FEM analysis and CFD analysis are using a different meshing system, which results in a mismatch between nodal displacement information and TurboGrid nodal positions. In other words, it has been necessary to map the FEM nodal displacement onto the CFD mesh. This can be solved by rotating FEM mesh of 90 degrees with respect to CFD mesh and then expanding it to 360 degrees in order to get a complete matching between meshes. Thus, FEM environment communicates to CFD environment how blades has to vibrate during unsteady simulations. When all the necessary data from FEM analysis have been collected, it is time to proceed with the setup of unsteady simulations.

6.5 Unsteady numerical modeling (time integration method)

Starting from the numerical setup of the steady-state, it is necessary to make some changes mainly to integrate blade motion in the analysis. Basically, from a null mesh motion, the mesh deformation option switches to regions of motion specified. It is then possible to insert the displacement profile data and set the periodic displacements of the mode shape under consideration for the blade domain. The mode frequency is equal to the natural frequency present in the blade displacement file. In Table 6.3 the modal frequency and reduced frequency for each simulated mode is stated. The reduced frequency is defined by the time t needed for a fluid particle to travel across the blade chord c divided by the oscillation period T, as previously expressed in equation (2.3). The chord value at mean radius used in the reduced frequency calculation is equal to $0.0983\ m$, while v_{ref} is the mass-averaged relative velocity, extracted at rotor inlet from its steady state analysis and equal to $376.27\ m/s$.

Table 6.3: Reduced frequency for the first six mode shapes of rotor 1 VINK compressor

Mode	Modal frequency [Hz]	Reduced frequency [-]
1	370.60	0.61
2	766.18	1.26
3	1090.9	1.79
4	1718.31	2.82
5	1852.88	3.04
6	2305.07	3.78

The scaling factor used in CFD computations for each mode shape can be expressed as:

$$Scaling = \frac{0.01 \cdot chord}{Maximum\ Modal\ Displacement} \tag{6.2}$$

Imposing this scaling factor means setting an amplitude of motion in CFX equal to 1% of the blade chord as shown in equation (6.2). This value is prescribed according to ANSYS CFX recommendations, useful to avoid negative volume issues arising when high displacements are set up. For each simulation, it is necessary to select the nodal diameter and the sign of TWM. The positive direction of TWM (forward) corresponds to the imposed direction of rotation in case of a rotating blade row.

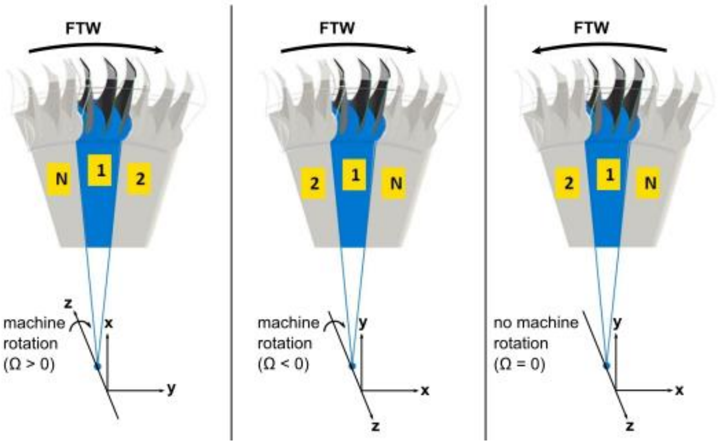

Figure 6.5: TWM convention in ANSYS CFX [23]

All the other domain mesh motions are set to stationary, except for the shroud, which has an unspecified mesh motion. In order to achieve converged solutions a numerical setup study has to be performed. The transient method used is Time Integration, which allows to set up values for the time period, time steps and time duration. Due to high CPU cost of unsteady simulations, ANSYS CFX recommendations for the number of periods and time steps per period are practiced. In particular a minimum of 6 periods and 50 time steps are recommended. Another recommendation is to ensure that blades experience same deformations for each time step. This is achieved by respecting the following equation:

$$Time\ Steps\ Per\ Period = \frac{4 \cdot 2\pi}{IBPA} \tag{6.3}$$

The number of time steps has to set equal to a multiple of the value yielded from equation (6.3). The numerical setup in terms of time steps and period employed for the investigated mode shapes and turbulence model are shown in Table 6.4, taken from a previous study on the same blading. The transient scheme used is Second Order Backward Euler. For the convergence control, the max coefficient loops is placed equal to 15 and the residual target is set to $1e-05$.

Table 6.4: Time steps for different NDs [22]

ND	Time Steps	ND	Time Steps	ND	Time Steps	ND	Time Steps	ND	Time Steps
$0=0$	80	$10=-41$	102	$20=-31$	51	$30=-21$	68	$40=-11$	51
$1=-50$	204	$11=-40$	204	$21=-30$	68	$31=-20$	204	$41=-10$	204
$2=-49$	102	$12=-39$	85	$22=-29$	102	$32=-19$	51	$42=-9$	68
$3=-48$	68	$13=-38$	204	$23=-28$	204	$33=-18$	68	$43=-8$	204
$4=-47$	102	$14=-37$	102	$24=-27$	68	$34=-17$	24	$44=-7$	102
$5=-46$	204	$15=-36$	68	$25=-26$	204	$35=-16$	204	$45=-6$	68
$6=-45$	68	$16=-35$	51	$26=-25$	102	$36=-15$	68	$46=-5$	102
$7=-44$	204	$17=-34$	84	$27=-24$	68	$37=-14$	204	$47=-4$	204
$8=-43$	51	$18=-33$	68	$28=-23$	51	$38=-13$	102	$48=-3$	68
$9=-42$	68	$19=-32$	204	$29=-22$	204	$39=-12$	68	$49=-2$	204
								$50=-1$	102

6.6 Harmonic Balance method

ANSYS CFX Harmonic Balance (HB) method is implemented within a pressure-based solution approach [23]. In this method, the transient flow variation is represented by a Fourier series for a prescribed fundamental frequency ω. Typically, M harmonics (or modes) are retained in the Fourier series for this approximation. The unsteady period is equally divided into $N=(2M+1)$ time levels on which the time derivative is evaluated using the spectral approximation, and the system of non-linear equations coupling all N time levels are solved iteratively. For example, if one harmonic is retained $M=1$, then 3 time levels are required. If 3 harmonics are retained $M=3$ then 5 time levels are required. A pseudo-time marching approach similar to the steady-state solution method is used to solve these N time levels coupled equations. In general, complex transient flows containing sharp discontinuities may require a larger number of harmonics to be retained in order to resolve the flow features, while simpler smooth flows require a smaller number of harmonics. The smaller the number of retained harmonics, the more efficient the Harmonic Analysis (HA) method is with respect to the time-marching solution. Therefore, it is essential to use the smallest number of harmonics at which the solution accuracy is acceptable. The efficiency of the solution calculation is also affected by the size of the specified pseudo-time step. Typically, the size of the pseudo-time step is determined as the period of the unsteadiness divided by the intended number of pseudo-time steps per period. A large number of pseudo-time steps per period (that is, a small time step size) makes the solution converge slowly and inefficiently with respect to a time-marching solution. A lower number of pseudo-time steps per period (that is, a large time step size) advances faster towards the converged solution and is more attractive, but may cause numerical stability issues. It has been found that 15 to 30 pseudo-time steps per period typically results in a good balance between calculation efficiency and solution stability.

A blade flutter simulation using HB method is set up alike a blade flutter simulation using TI method, except for some features. Transient method switches to Harmonic Balance and the number of modes used is $M = 1$ in this case. Few trials have been carried out retaining a larger number of harmonic ($M = 3$), but the increase in computational time with respect to Time Integration method is significant. Max number of iterations is placed equal to 1000 and the size of the pseudo-time step is set to Physical Timescale. This latter value is imposed equal to the period of the vibration cycle divided by 15 pseudo-time steps per period. The residual target is fixed to $1e - 8$, necessary in this case to reach a convergenced condition.

7 RESULTS AND DISCUSSION

Steady and unsteady results obtained by numerical simulations are discussed in the present section. Firstly, steady-state blade loading curve and Mach number flow field results are shown for the three mesh refinements and for two different turbulence models at different span heights. Afterwards S-shape curve, unsteady pressure surface coefficient (amplitude and phase) and local work coefficient distribution on the blade surface for different mode shapes are presented and discussed. In these latter unsteady cases, results at hub are not significant as the deformation is almost zero, while 50%, 90% and 95% span results are taken into account and compared. Additionally, figures of blade displacements and unsteady pressure flow field are shown in order to better understand the trends of the predicted quantities. Peak-to-Peak (P2P), Steady-Value (SV) torque errors and discrepancies in aerodamping between blades for higher modes (fourth, fifth and sixth mode) have been stated and compared with cases characterized by longer simulation time since convergence and single aerodamping value are tougher to attain for these modes. Deeper investigations has been performed for the first mode, where unsteady predictions for more nodal diameters and different turbulence model are analyzed. Scaling factor and convergence investigations have been carried out for the fourth mode in order to validate the employed numerical setup. Moreover, Fourier transformation has been implemented for the first four modes in MATLAB by extracting pressure values at each time step so as to check out the goodness of ANSYS CFX prediction making use of this pre-implemented transformation. Discrepancies between MATLAB and CFX predictions have been stated in significant points on the blade surface. Lastly, different transient method results (TI and HB) have been compared in order to find a trade-off in computational effort. ANSYS CFD-post and MATLAB are the tools utilized for post-processing data coming from ANSYS CFX Solver and developing every shown result.

7.1 Steady-state results for first stage computation

A transonic rotating blading features a supersonic inlet region where the flow velocity is above the speed of sound and, after the increase in pressure due to the compression, the flow becomes subsonic. The passage from the supersonic region to the subsonic one gives rise to a shock, which is the only discontinuity in nature and acts as a prompt response. The shock distribution helps the compressor to decelerate the flow and increase the static pressure, which is the main advantage of a transonic machine. However, as a drawback the total pressure decreases due to an increase in losses. Steady state results presented in this section are the ones obtained from the entire stage simulation. Only the first rotor blade loading have been analyzed. The general trend of each blade loading curve for the rotating blading shown in figures below is characterized by a pressure peak at the leading edge due to the frontal impingement of the flow and an almost constant pressure on the pressure side downstream. On the suction side, a normal shock with a rapid increase in pressure close to the mid-chord section is visible. Blade loading trend is expected to match the Mach number flow field in the rotor passages, which allows to realize how the flow is evolving over the suction and the pressure side of the rotor VINK blades. The suction side shows a higher Mach number as the flow is being accelerated, while along the pressure side the increase in pressure is higher. The presence of wakes at the trailing edge creates a decrease in the local Mach number, as possible to see in these contour plots. Wakes reflect total pressure losses, which affect the machine performance and thus efficiency. Moreover, Mach number flow field presents a bow shock at the inlet, which is caused by the leading edge thickness and is expanding to the suction side of the adjacent blade until mid-chord position.

The solution dependence on turbulence model, k-epsilon or SST, and mesh refinement level, previously presented in Table 6.1, has been investigated. In Figure 7.1, 7.2 and 7.3, blade loading curve comparisons for the two different turbulence models are depicted. For all mesh refinements, a qualitative good agreement between k-epsilon and SST model has been found 50% span steady predictions. The same agreement has been found for 5% span steady predictions, but these figures show only 50% and 95% span for the sake of simplicity. Larger differences in rotor blade loading curve between the two models are visible at 95% span, where the shock predicted with SST model is clearly less sharp than the one predicted with the k-epsilon model. For this reason, SST model have been further investigated by performing in turn unsteady computations. In Figure 7.4 and 7.5, a sensitivity study based on the mesh refinement at the same turbulence model is represented. A refined mesh captures flow gradients better, which may be smeared in a coarsely resolved mesh, reason why sensitivity investigations are conducted [33]. The number of nodes along the blade profile increases proportionally to the total number of nodes. Rotor blade loading curves show a mesh independence for the k-epsilon model at each span location. Some slight variations on the suction side are noted, but these are insignificant compared to the level of refinement. This means that the near-wall pressure distribution is determined by the turbulence model and no significant local variations are registered as the mesh is refined. From here on out, successive investigations have been conducted using the medium refinement mesh for this turbulence model in order to optimize accuracy and computational effort. In fact, as function of the mesh refinement, computational time increases and it is necessary to choose the minimum grade of refinement suitable for the investigation enabling to get better performances. In case of SST turbulence model, mesh independence is not completely verified, as the finest mesh shows a different pressure trend with respect to the coarse and the medium one at each span location, which are comparable. For this reason, the finest mesh is chosen in order to accurately investigate this model in the successive steps. Blade loading curves at different span heights are depicted in Figure 7.6 and this gives a quantitative idea of the pressure variation along the normalized streawise coordinate on rotor blades. The shock position along the suction side moves from 40% axial chord at the hub to about 48% at the mid span and to 50% axial chord at the tip. Higher span sections are thus more fore-loaded than the hub section. Steady pressure distributions along the pressure side are quite unaffected by the shock, except for leading edge zone. The stator loading is a bit simpler and shows more loading at higher spans, however for the sake of simplicity is not presented in this study [34].

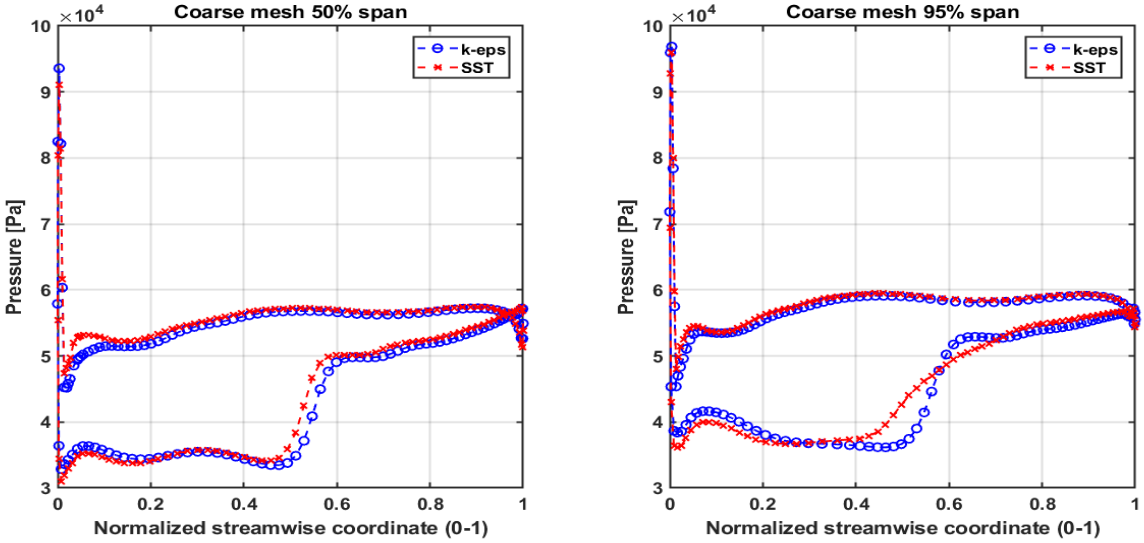

Figure 7.1: Blade loading comparison between k-epsilon and SST turbulence model for the coarse mesh

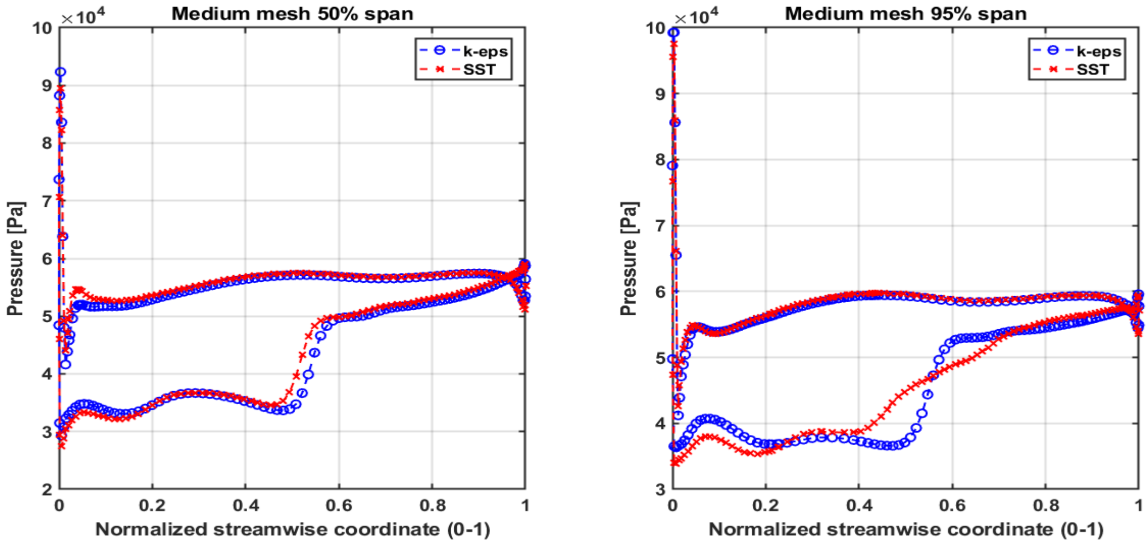

Figure 7.2: Blade loading comparison between k-epsilon and SST turbulence model for the medium mesh

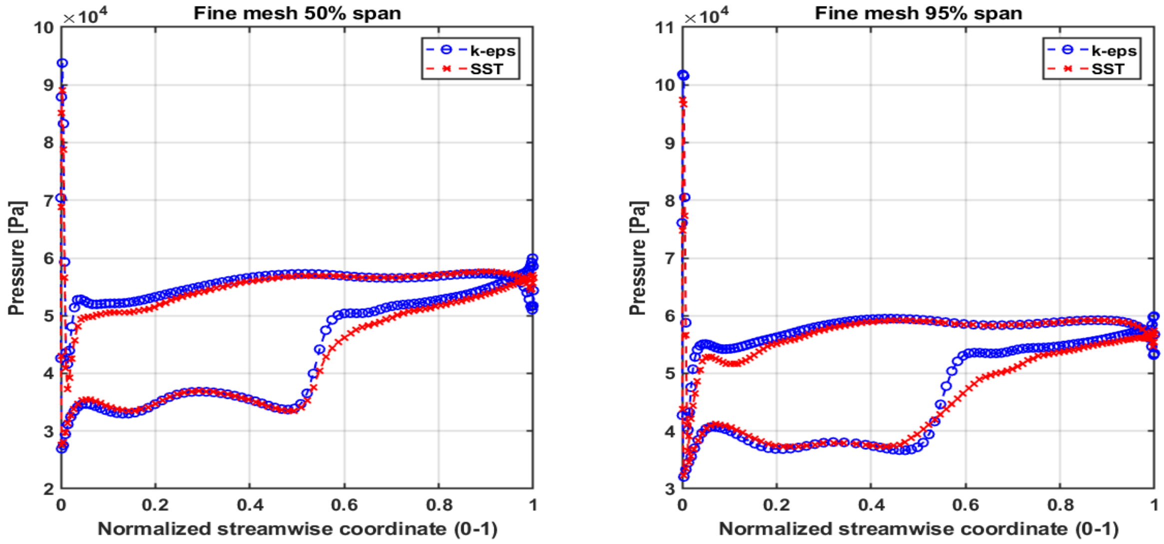

Figure 7.3: Blade loading comparison between k-epsilon and SST turbulence model for the fine mesh

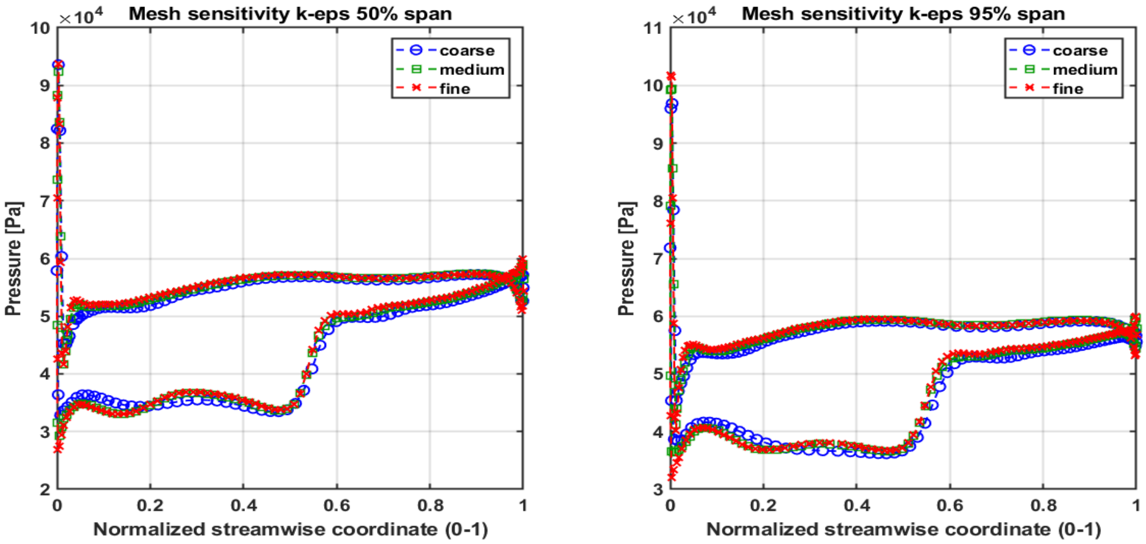

Figure 7.4: Blade loading comparison with the three different mesh refinements in the model with k-epsilon turbulence model

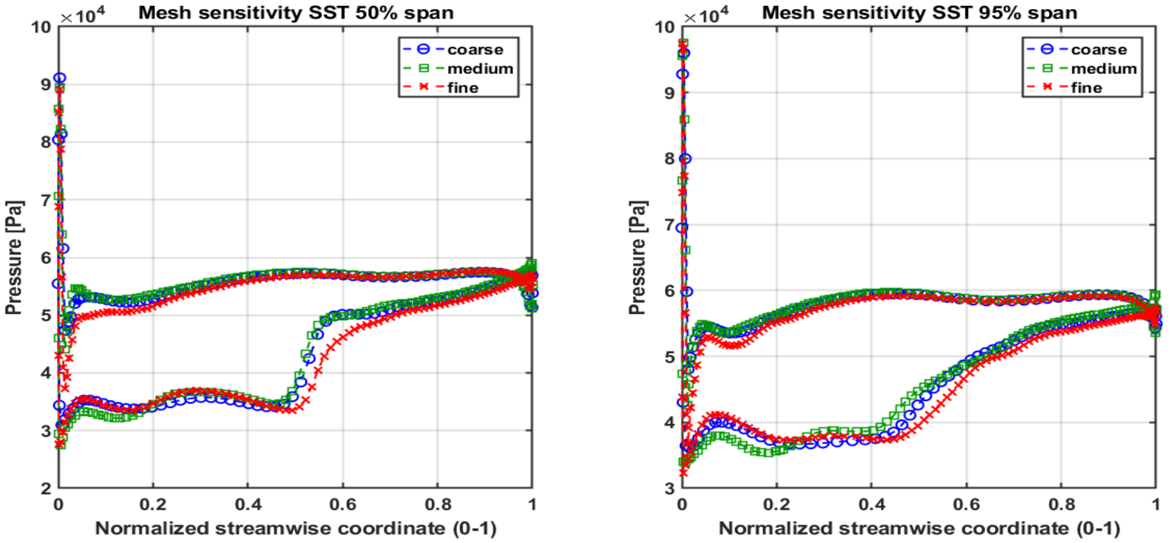

Figure 7.5: Blade loading comparison with the three different mesh refinements in the model with SST turbulence model

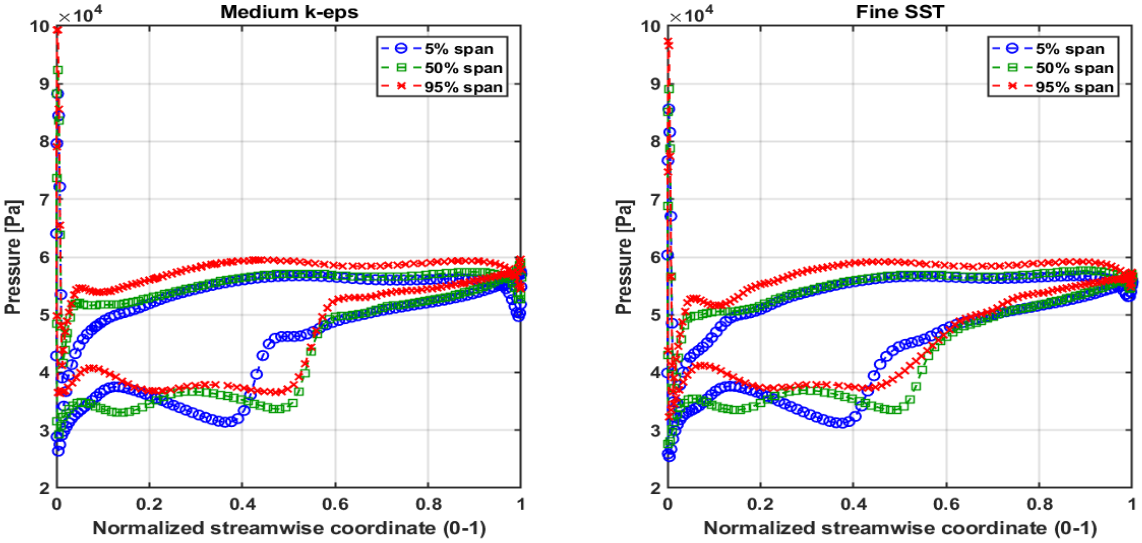

Figure 7.6: Blade loading comparison at different span locations for the chosen steady setups

Aerodynamics in blade passages is better understood with the steady Mach number contours represented in Figure 7.7 and 7.8. Looking at the suction side, the inflow being supersonic at the leading edge accelerates first and then starts decelerating due to change in the passage area, thus, experiencing a shock near the mid-stream position. The passage shock is not affecting the pressure side of the blade at this operating point, which features nominal rotational speed at design throttle. The maximum Mach number does not exceed 1.4. Moreover, comparisons between the two turbulence models for all the mesh refinements at 95% span do not show significant differences that means numerical setups are not generating disturbances in the analysis and all the configurations are exactly referred to the same operating condition in the compressor map. The only change is related to the magnitude of the shock on the suction side, differently predicted in these two cases. Changes not only in blade geometry, but also the operating conditions such as the inlet Mach number, inflow direction or back-pressure highly affect the shock pattern of the passage and thus the aerodynamics of these passages [35].

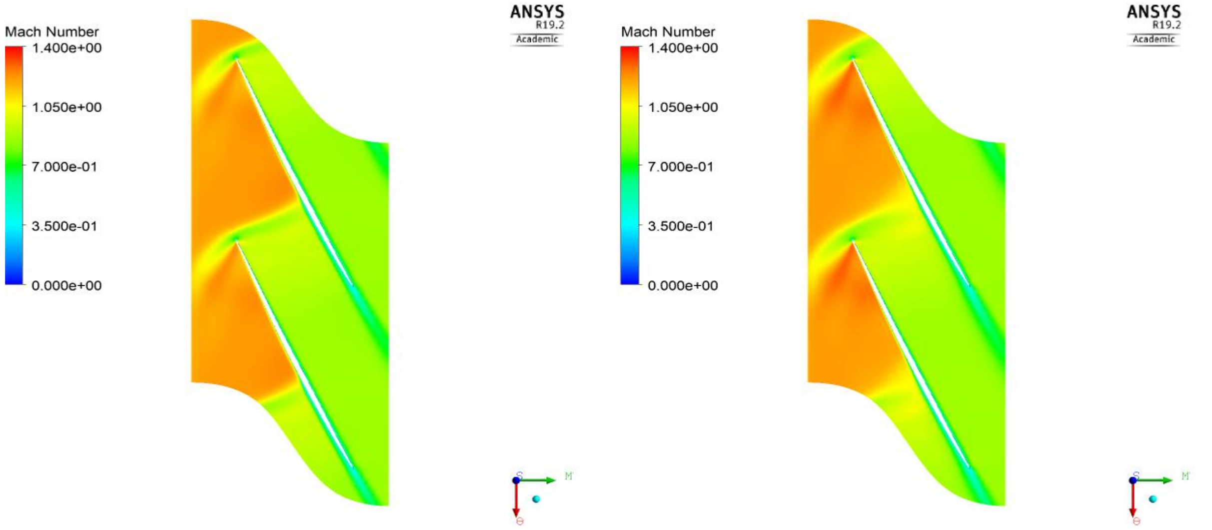

Figure 7.7: Comparison Mach number flow field for the medium mesh between k-epsilon (on the left) and SST (on the right) turbulence model at 95% span

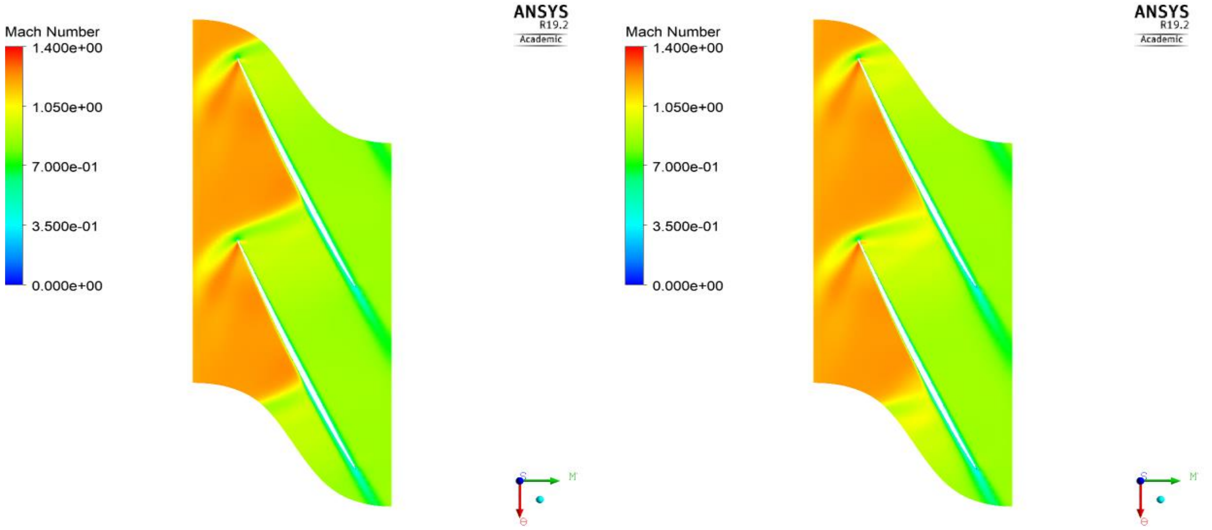

Figure 7.8: Comparison Mach number flow field for the fine mesh between k-epsilon (on the left) and SST (on the right) turbulence model at 95% span

7.2 Steady-state results for first rotor computation

In order to proceed with unsteady investigations aiming to predict aerodynamic damping, steady computations of the first rotor alone have been conducted and are compared with the previous rotor predictions extracted from the entire stage computation. In particular, after taking inlet and outlet properties over the rotor in the stationary frame of reference from the stage solution, it has been possible to set up steady simulations on the rotor with results shown in Figure 7.9, 7.10 and 7.11. As aforementioned, after the mesh sensitivity study the medium mesh for k-epsilon model and the finest mesh for SST model have been utilized as optimal models. The finest mesh with k-epsilon model gives almost the same steady predictions but with an increased computational time and thus it is not taken into account. One can be noticed that steady predictions of the blade loading for the stage and for the rotor case are entirely in agreement at each span height. On the suction side of the blade, some mismatches between the two curves for each span location can be found, but these differences are not significant. Plots of the Mach number flow field also show an agreement between the two scenarios but they are not reported for the sake of simplicity. This simplifies the computational effort of unsteady simulations in modelling and time because only the rotor will be processed without the initial plenum. The rotor solution will be provided in unsteady simulations as initial condition. It is necessary to duplicate the passage in order to be consistent with the transient method applied in the unsteady analysis.

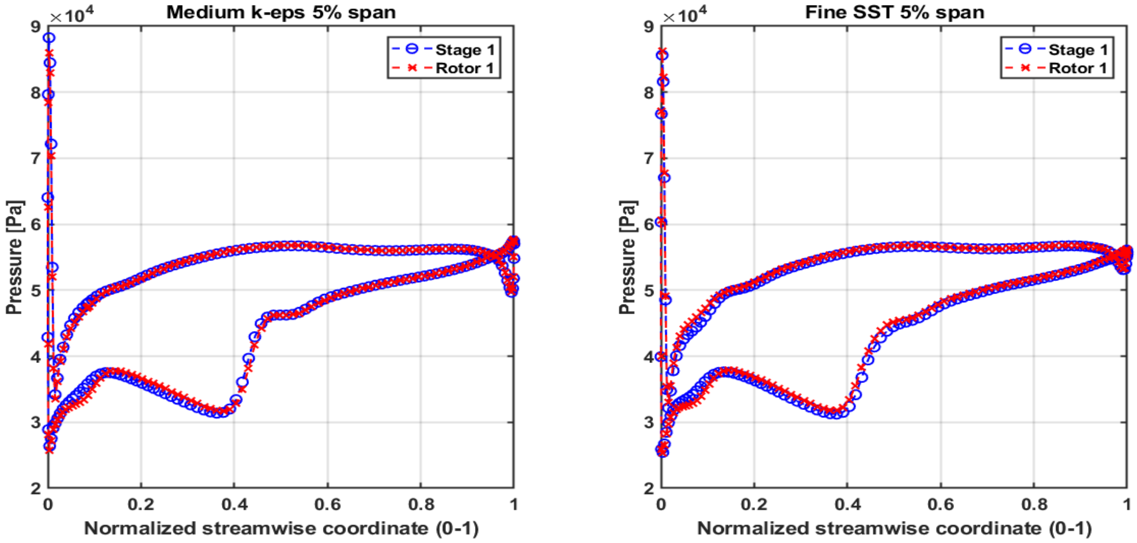

Figure 7.9: Comparison between stage 1 and rotor 1 blade loading at 5% span

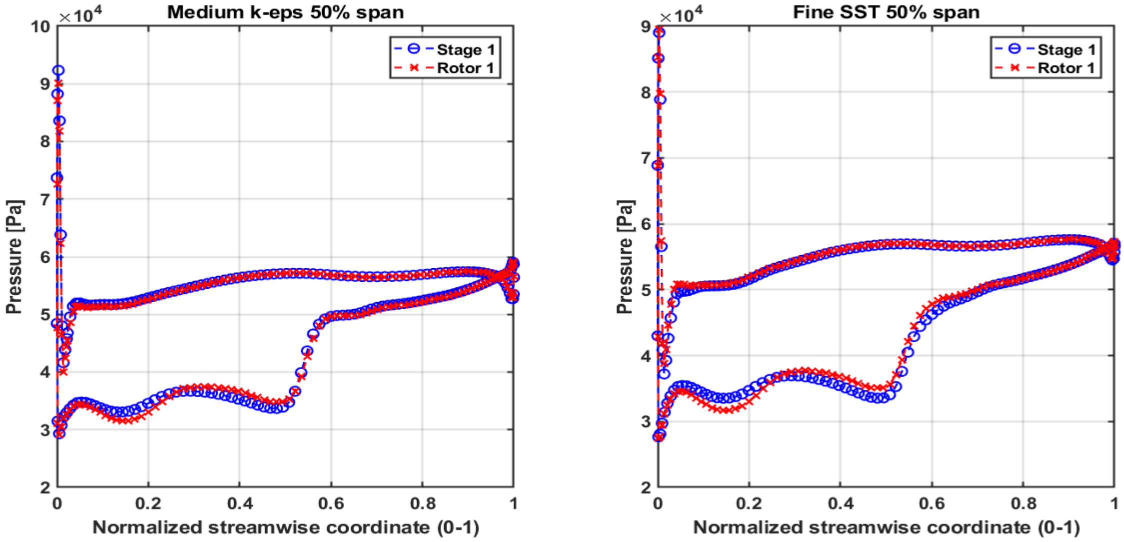

Figure 7.10: Comparison between stage 1 and rotor 1 blade loading at 50% span

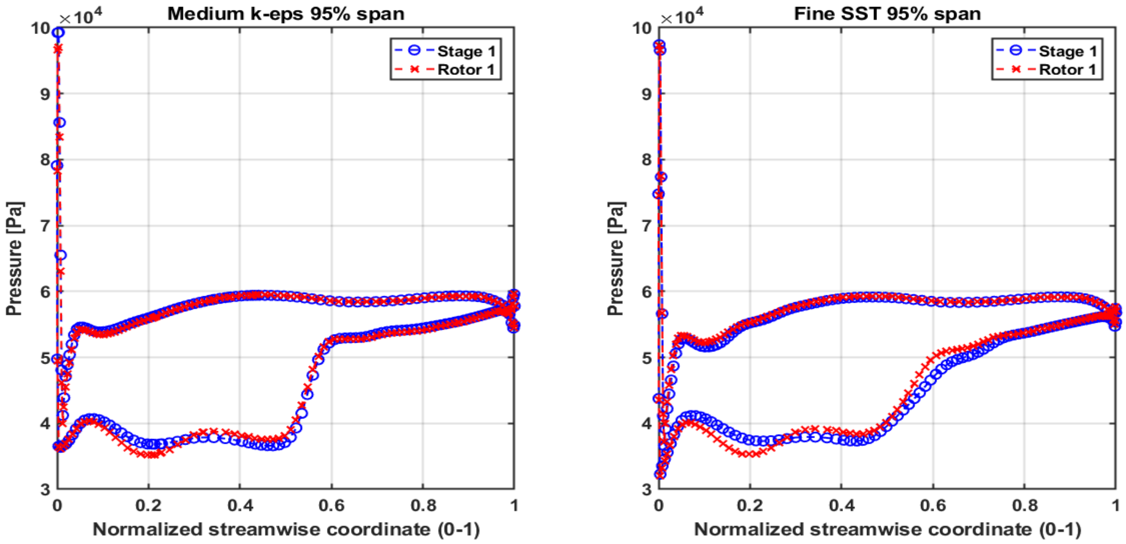

Figure 7.11: Comparison between stage 1 and rotor 1 blade loading at 95% span

7.3 Unsteady results

For computations and analysis of the unsteady flow solution for each mode, Fourier Transformation and energy method have been employed, as previously described in the theoretical approach and methodology sections. This latter approach gives results in terms of aerodynamic damping, expressible in terms of logarithmic decrement or aerodamping coefficient. Afterwards, further investigations have been carried out aiming to find local work coefficient and unsteady pressure coefficient distributions in order to get insights into aerodamping values for each configuration. The logarithmic decrement δ is a global scalar for a quantitative comparison of aerodamping results. This one is positive when the amplitude is going to be reduced and negative when amplitude is increasing, as in case of flutter. Logarithmic decrement value is related to the aerodynamic work done by the blade on the fluid and the average kinetic energy of the vibrating blade, as shown in the following expression:

$$\delta = \frac{W_{aero}}{4 \cdot K_{ave}} \tag{7.1}$$

It should be mentioned that equation (7.1) is the same as equation (2.21), except for the negative sign. This because CFX gives directly positive or negative W_{aero} in case of stabilizing or detrimental effect respectively, while the opposite convention is used in the theoretical approach. W_{aero} can be directly taken from a dedicated monitor previously set in CFX-Pre or can be alternatively calculated by extracting from CFD-post the Transient Averaged Wall Work Density and applying the following formula:

$$W_{aero} = arealnt(Wall\ Work\ Density.Trnavg) \cdot Time\ Steps\ Per\ Period \tag{7.2}$$

where $arealnt$ is a CFX function computing the numerical integration over the blade surface. It is important to refer W_{aero} and K_{ave} at the same blade amplitude that means the average kinetic energy of the blade has to be scaled, as possible to see in the following expression:

$$KE_{ave} = \frac{Scaling^2 \cdot \omega^2}{4} \tag{7.3}$$

where the scaling factor definition, in turn, is the same expressed in equation (6.2). To evaluate the distribution of work done by the blade on the fluid at different span heights, local work coefficient distributions have been computed at 50%, 90% and 95% span. This investigation has been performed for the least stable nodal diameter of each mode. Wall Work Density distribution has been extracted along the streamwise coordinate at the different span heights. In particular, the Transient Averaged Wall Work Density value is used in the computation as it is calculating the transient average value per time step. Thus, the local work coefficient, which is meant as a normalization of W_{aero}, is defined as:

$$w = \frac{Wall\ Work\ Density.Trnavg \cdot Time\ Steps\ Per\ Period}{\pi \cdot \alpha^2 \cdot c \cdot p_{ref}} \tag{7.5}$$

where $\alpha = h_{max}/c$ and is equal to 0.01 for a blade amplitude of 1% of the chord, time steps per period depend on the numerical transient setup for each configuration and p_{ref} is the dynamic pressure calculated as difference between inlet total pressure in the relative frame of reference, equal to $89.7\ KPa$, and inlet static pressure, equal to $39.5\ KPa$, both extracted from the steady-state solution. By looking at the local work coefficient distribution at different span heights, stable and unstable regions with respect to the stability line can be identified, responsible of the logarithmic decrement value in a certain configuration for a given mode shape.

A deeper investigation of unsteady pressure originally generated by blade displacements and characterizing W_{aero} value for each configuration has been performed by computing unsteady surface pressure coefficient distribution, which is representative of the harmonic pressure perturbations around the average pressure value due to harmonic motion of the blade. As widely discussed in theoretical approach [10], this coefficient, normalization of the unsteady surface pressure, can be calculated as:

$$c_p = \frac{\hat{p}}{\alpha \cdot p_{ref}} \tag{7.6}$$

where $\hat{p}$ is the complex unsteady pressure amplitude extracted from each unsteady solution, normalized by the maximum oscillation amplitude α, equal to 1%, and the dynamic pressure at the machine inlet taken as reference. The unsteady pressure perturbation can be expressed as:

$$\tilde{p} = p.A1 - ip.B1 \tag{7.7}$$

where $p.A1$ and $p.B1$ are the first harmonic pressure coefficients of the Fourier series, representing respectively the real and the imaginary part of the signal. CFX Fourier transformation retains up to 7 Fourier coefficients, but the first one should be a fair enough approximation of the entire pressure signal as it is the harmonic containing more information. The unsteady pressure amplitude of the first harmonic can be expressed as:

$$\hat{p} = \sqrt{(p.A1^2 + p.B1^2)} \tag{7.8}$$

Unsteady pressure phase with respect to the harmonic motion can be also evaluated as it is a useful mean for evaluation of changes in amplitude between different cases.

7.4 S-shape overview for Time Integration method

Logarithmic decrement distribution has been calculated for first, fourth, fifth and sixth mode since second and third mode were previously analyzed in other studies. Several unsteady simulations have been set up for the range of nodal diameters under consideration. The rotating row has 51 blades, thus the number of nodal diameters ranges between ± 25, following the approach previously exposed in the theoretical section. Initially, unsteady simulations have been performed with a step of 5 nodal diameters; afterwards in correspondence of least stable regions the step has been progressively reduced in order to get the least aerodamping value. Every simulation is performed at the design operating condition that means design throttle and nominal rotational speed and the steady-state solution has been used as initial condition. Discrepancies in logarithmic decrement values between the two simulated blades have been evaluated for each case in order to assess the goodness of CFX predictions.

In Figure 7.12 and 7.13, the logarithmic decrement distribution of the first mode with k-epsilon and SST turbulence model respectively are shown. In Figure 7.14, a comparison between the two previous curves for blade 1 is shown. The transient parameters used in this case are number of time steps equal to 50 and number of periods equal to 6 for each configuration, except for some NDs whereby to reach a higher convergence level and lower discrepancies in aerodamping values the number of periods is extended to 9. In this way, it has possible to reduce CPU time for those configurations in which a fair convergence level have been obtained faster as well as low discrepancies in aerodamping values between the two blades. For each S-shape curve, in fact, the deviation between aerodamping values for the two blades is stated for each nodal diameter. For first mode with medium k-epsilon, the least stable mode is $ND = 2$, characterized by a log-dec value of 0.153% for blade 1 and 0.141% for blade 2. The deviation value in this configuration is 8.37%. In case of SST model, the least stable mode is still $ND = 2$, characterized by a log-dec value of 0.114% for blade 1 and 0.103% for blade 2, with a deviation value equal to 9.67%. It can be noticed that in the least stable condition reaching an agreement between aerodamping values of the two blades is nearly always trickier than in the other cases. By comparing deviation in Figure 7.12 with the one in Figure 7.13, it is possible to see differences in aerodamping between blades driven by the turbulence model. The deviation value in the least stable condition is always the highest one for both cases, but moving towards negative nodal diameters deviation values are quite different in the two cases. This can be related to the convergence level, which is not lower than 1% calculating a Peak-to-Peak torque error and leads to more discrepancies in the k-epsilon case. Looking at the discrepancy between k-epsilon and SST prediction for blade 1 in Figure 7.14, the highest values have been found in correspondence of the least stable mode confirming that predictions in this area differ due to lower numerical robustness. Further investigations of local work coefficient and unsteady pressure coefficient distribution will be conducted for the first mode in order to compare the influence of these two different turbulence models.

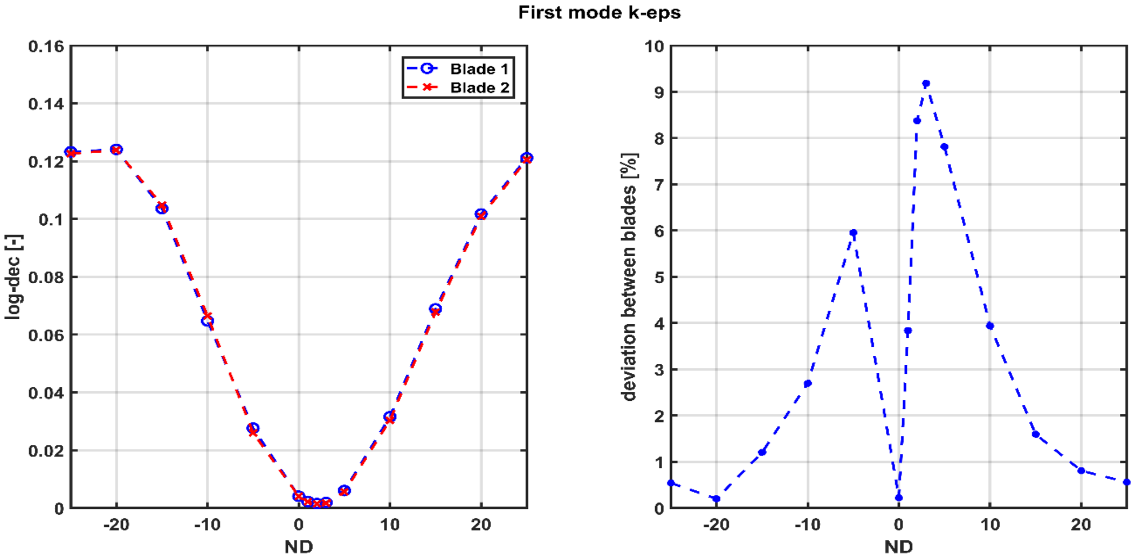

Figure 7.12: Logarithmic decrement distribution for the first mode using k-epsilon turbulence model and deviation in predicted values between the two blades

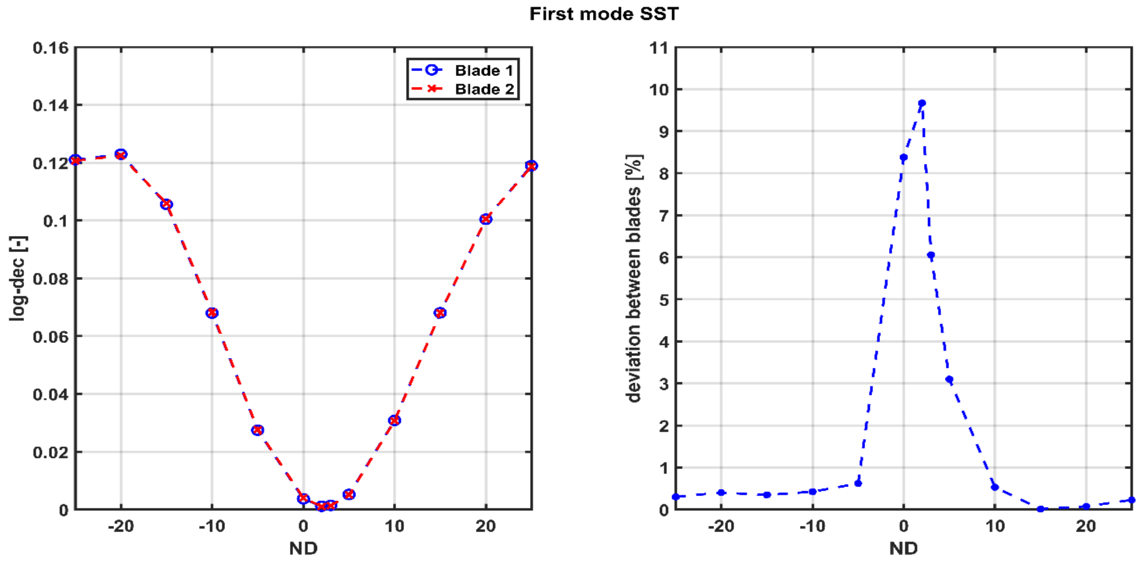

Figure 7.13: Logarithmic decrement distribution for the first mode using SST turbulence model and deviation in predicted values between the two blades

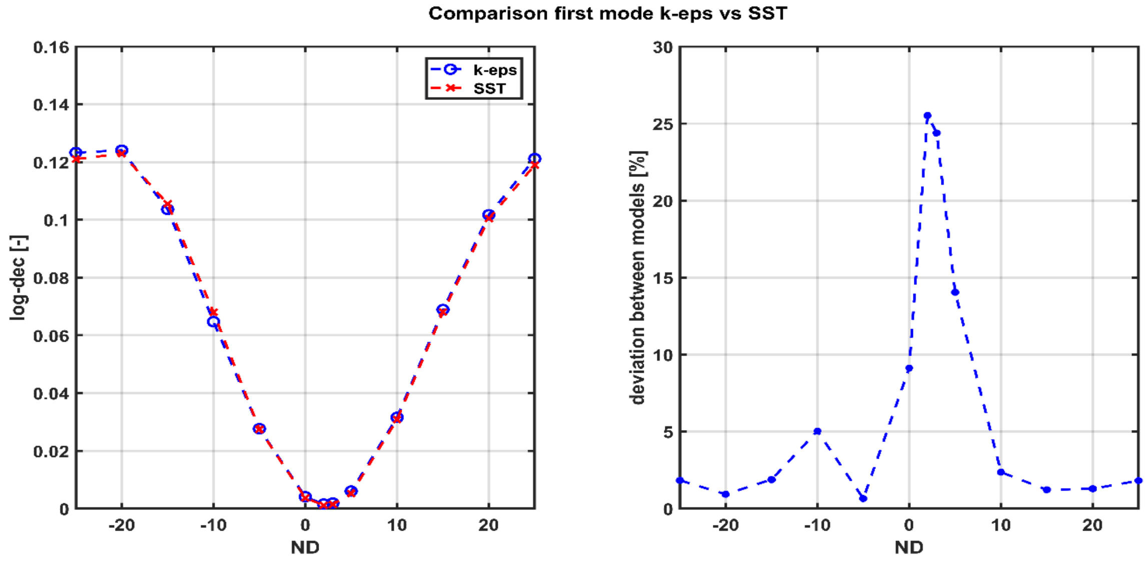

Figure 7.14: Logarithmic decrement distribution for the first mode comparing k-epsilon and SST turbulence model and deviation in predicted values between the two models

Fourth, fifth and sixth mode shape feature higher reduced frequencies that means they are far away enough from the flutter limit with respect to the first mode, which is characterized by the least stable mode on the border with the stability line. This is verified by computing the S-shape curve also for these modes, only using k-epsilon model, since SST model tested for the first mode has not considerable influence and shows almost the same trend of the case with k-epsilon model. Several simulations have been computed to build up the curves; each of them can be more or less computationally expensive as function of the analyzed nodal diameter and the number of time steps employed in the investigation, determined by following values in Table 6.4. In Figure 7.15, 7.16 and 7.17 logarithmic decrement distributions and deviation in aerodamping predictions between the two blades are depicted for fourth, fifth and sixth mode. The number of periods has been set up to 9, thus stopping simulations at a certain convergence level. In this way, it has been possible to reduce CPU time getting a certain discrepancy in aerodamping values of the two blades. As mentioned before, the requirement of modeling two blades arises from the use of Fourier transformation transient method and every case shows a discrepancy between blades aerodamping. For each mode shape the least stable condition can be stated, which corresponds to the minimum logarithmic decrement value in the S-shape curve:

- for the fourth mode the least stable condition is $ND = 3$, characterized by a log-dec value of 2.26% for blade 1 and 2.23% for blade 2;
- for the fifth mode the least stable condition is $ND = 10$, characterized by a log-dec value of 1.80% for blade 1 and 1.63% for blade 2;
- for the sixth mode the least stable condition is $ND = -4$, characterized by a log-dec value of 0.62% for blade 1 and 0.63% for blade 2.

In each analysed case, the deviation in aerodamping values between two blade values is higher for the configurations in which lower logarithmic decrement values have been found. Moreover, for $ND = 0$ aerodamping predictions seem quite accurate in every case since deviation values are always quite limited.

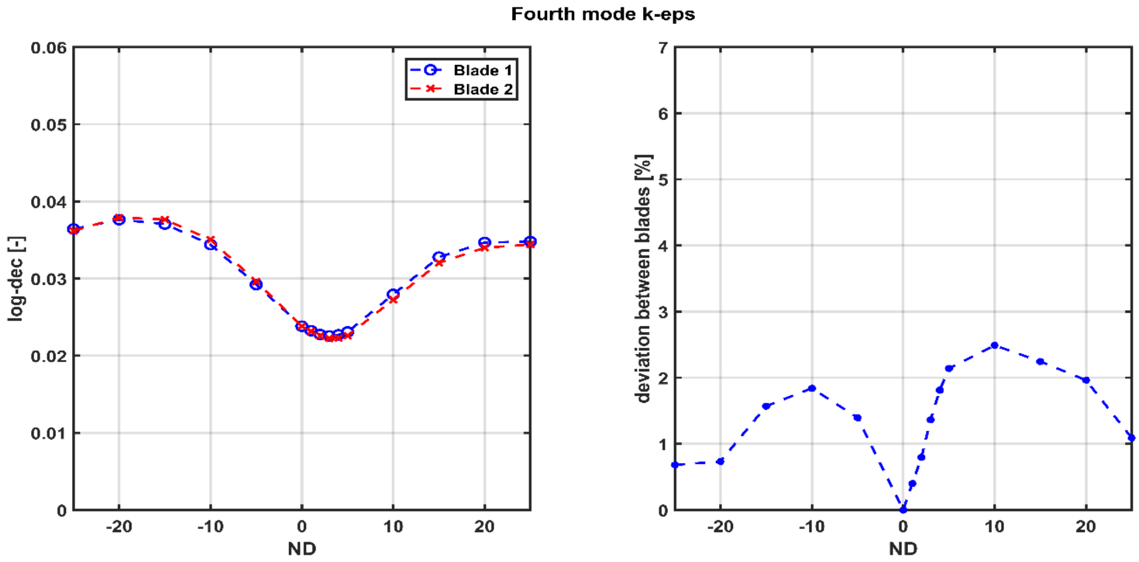

Figure 7.15: Logarithmic decrement distribution for the fourth mode using k-epsilon turbulence model and deviation in predicted values between the two blades

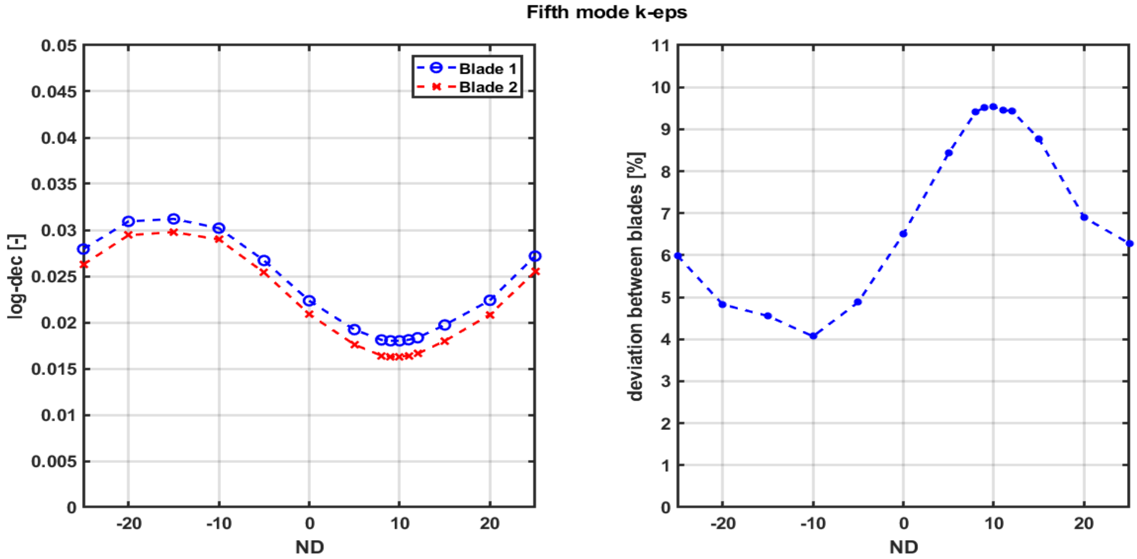

Figure 7.16: Logarithmic decrement distribution for the fifth mode using k-epsilon turbulence model and deviation in predicted values between the two blades

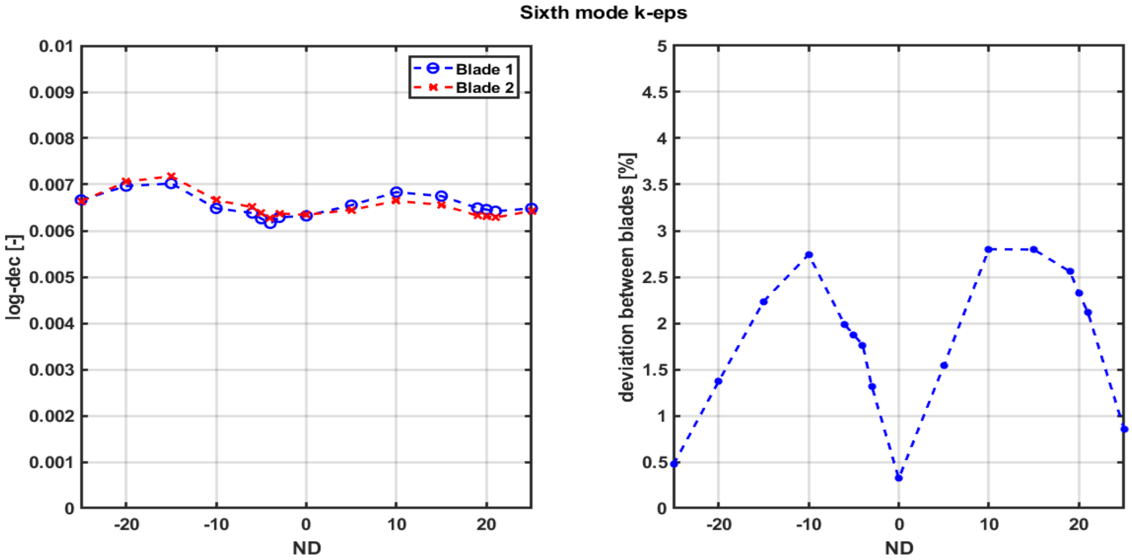

Figure 7.17: Logarithmic decrement distribution for the sixth mode using k-epsilon turbulence model and deviation in predicted values between the two blades

In Figure 7.18, the overview of logarithmic decrement distribution for every investigated mode is shown. Peak-to-Peak amplitude of the S-shape curve decreases with the order of the mode; in other words, higher is mode frequency, lower is the amplitude between two consequent peaks. Another important observation is that the average value of the curve is lower as much as higher is the mode. The only mode featuring flutter risk is the first mode as the least stable condition is approaching the stability line, which is the horizontal line passing through the origin. In fact, the reduced frequency for the first mode is within the critical reduced frequency range found in literature. All these predictions are dependent on the numerical setup and the turbulence model used. Varying one of these parameters leads to slightly different values if the numerical setup is robust enough or can cause a large change in aerodamping for unstable setups. It is thus important to conduct a sensitivity study in which number of time steps and number of periods are changed in order to assess the aerodamping values. This procedure has been carried out to assess convergence level and discrepancy in aerodamping in the least stable condition for each mode.

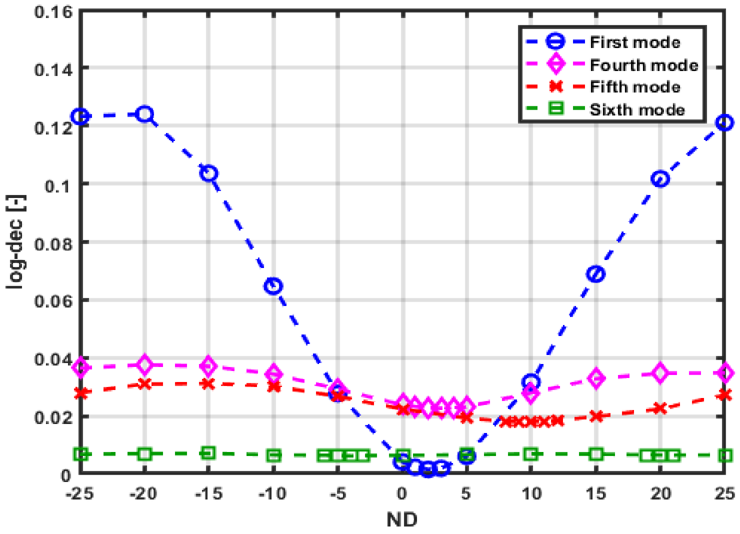

Figure 7.18: S-shape curve overview of all investigated modes for k-epsilon turbulence model

7.5 Convergence and discrepancy for higher mode predictions

In order to check the convergence level a torque monitor has been set up. Two different kinds of error have been evaluated in order to properly monitor the evolution in time of the torque, which are Peak-to-Peak error ($P2P$) and Steady-Value error (SV), estimated as a percentage error between the second-last and the last period of each simulation. Low convergence levels can be easier attained for the first, second and third mode, while for higher modes simulations present tougher behaviours. Therefore in these cases, convergence level has been evaluated in the least stable condition for the numerical setup used to obtain S-shape curves (P=9) and has been compared with the one in the same condition, but P=35. The following values have been calculated for P=9:

- fourth mode ($ND = 3$): $P2P = 0.454\%$ and $SV = 0.0461\%$;
- fifth mode ($ND = 10$): $P2P = 0.168\%$ and $SV = 0.0574\%$;
- sixth mode ($ND = -4$): $P2P = 1.56\%$ and $SV = 0.0752\%$.

For P=35, instead, Peak-to-Peak error and Steady-Value error are equal to 0% for each simulation in the least stable condition. Discrepancy in aerodamping between the two blades in the least stable condition can be found from the previous plots at P=9 and can be compared with the one at P=35 for higher modes. For P=9, the deviation assumes the following values:

- fourth mode ($ND = 3$): $deviation\ between\ blades = 1.365\%$;
- fifth mode ($ND = 10$): $deviation\ between\ blades = 9.536\%$;
- sixth mode ($ND = -4$): $deviation\ between\ blades = 1.764\%$.

For P=35, deviation values reduces, but there is still a difference in aerodamping values:

- fourth mode ($ND = 3$): $deviation\ between\ blades = 0.721\%$;
- fifth mode ($ND = 10$): $deviation\ between\ blades = 7.202\%$;
- sixth mode ($ND = -4$): $deviation\ between\ blades = 0.212\%$.

Therefore, it is possible to conclude that even for a Peak-to-peak error and Steady-Value error equal to 0%, discrepancy in aerodamping values between blades is always present. This can be related to numerical error propagations regarding reflective boundary conditions. Standard boundary conditions, when imposed on the boundaries of an artificially truncated domain, result in reflections of the outgoing pressure waves. As consequence, the internal domain may contain spurious wave reflections and thus it is required a precise control of these reflections to obtain more accurate flow solutions, but no special attention has been paid to these issues in this work.

7.6 Unsteady results for each mode

For each investigated mode and, additionally for the second and third mode taking into account only the least stable condition stated in previous studies, unsteady pressure coefficient and local work coefficient distribution have been computed at different span heights. In this way, it possible to get insights into the origin of the aerodynamic damping values previously found and to have a complete overview of the force on the blade for the first six modes. Each plot is supported with blade displacements and unsteady pressure flow field so as to better go through these quantities. In fact, every unsteady pressure variation is led by the displacements deforming the blade at that span location. All the modes involved in this analysis feature the same turbulence model, which is k-epsilon. Investigations have been conducted at 50%, 90% and 95% span, since displacements at the hub are much lower due to structural constraints and thus lower pressure distribution as well. This study has been developed using simulation solutions with a high level of convergence, that means P=9 for the first mode, P=14 for second and third mode and P=35 for the higher modes.

7.6.1 First mode with k-epsilon model

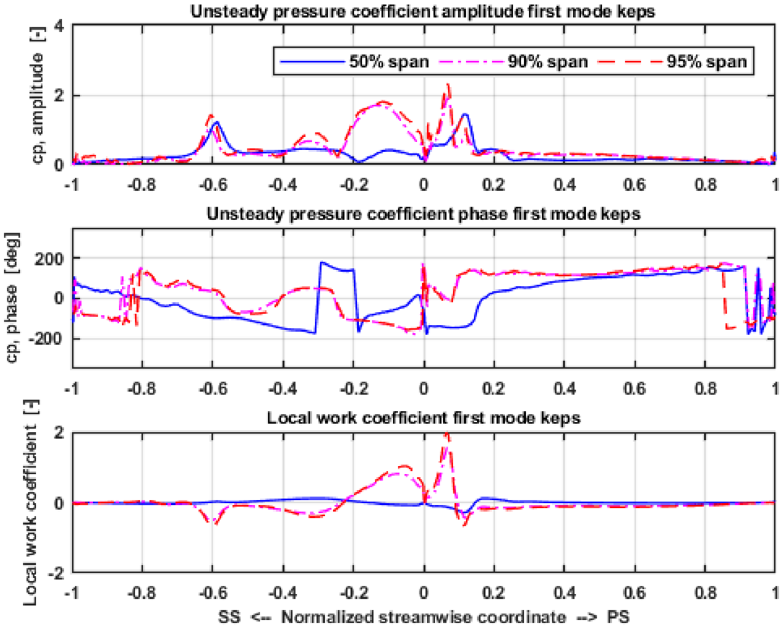

Figure 7.19: Unsteady pressure coefficient (amplitude and phase) and local work coefficient distribution for the first mode with k-epsilon model at 50%, 90% and 95% span

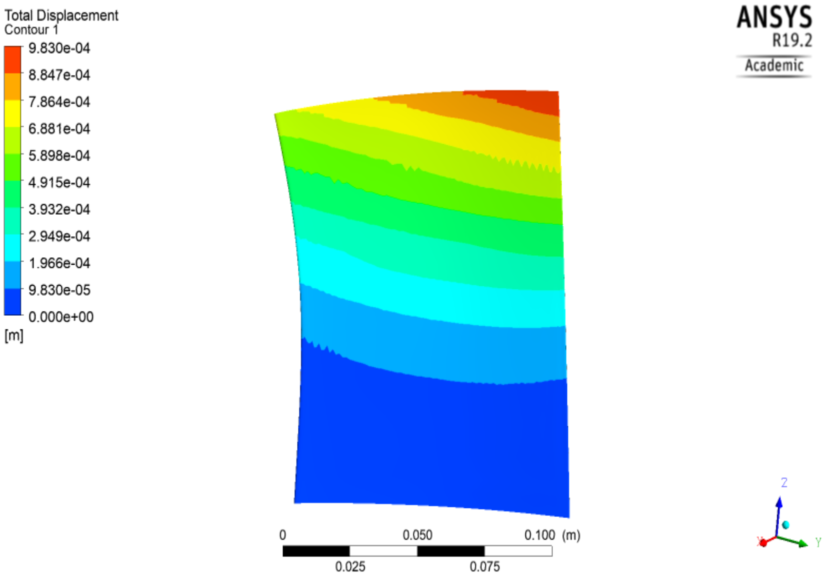

Figure 7.20: Blade displacements for the first mode

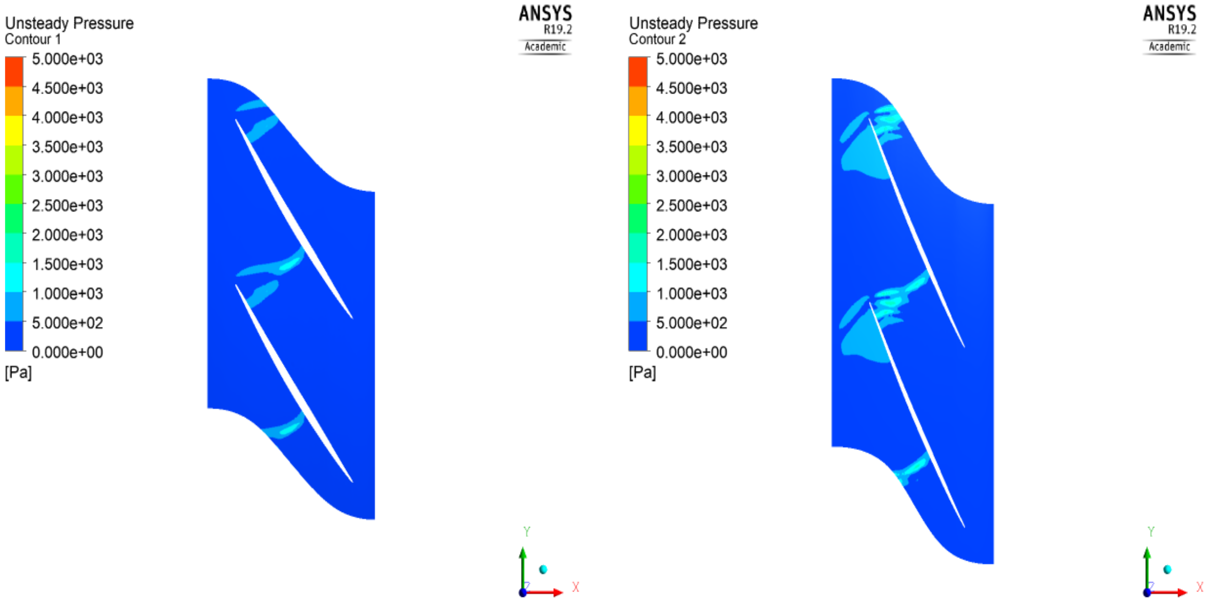

Figure 7.21: Unsteady pressure flow field for the first mode at 50% span (on the left) and 95% span (on the right)

In the first mode investigation, the highest unsteady pressure peak is visible in the region of the leading edge and is higher for higher span locations, as evident in Figure 7.19. After this one, the pressure side has not considerable unsteadiness for any span location. On the suction side, instead, different significant pressure peak are present as the one located at about -0.6 along the normalized streamwise coordinate related to the normal shock, which features a high value for each span height. This peak leads to instabilities as possible to see at the same span location in the local work coefficient distribution. There are no significant influences of tip leakage and mode shape between prediction at 90% span and 95% since the relative unsteady pressure and local work distributions follow the almost same trend. Predictions at 50% span, instead, are quite different with respect to higher span locations. In fact, as visible in Figure 7.20, displacements at 50% span are half of those near the tip, where the maximum displacement is found and also displacement direction is not creating large pressure unsteadiness for this particular case. This mode is supposed to be a first bending (1B). It should be noticed that every shift in amplitude between 50% span and 95% span is driven by a phase shift at the same streamwise position. Ultimately, more instabilities and unsteady pressure peaks can be seen at higher span location, while at mid-span for this mode pressure unsteadiness are quite limited, except in the area of the mid-chord shock.

7.6.2 Second mode with k-epsilon model

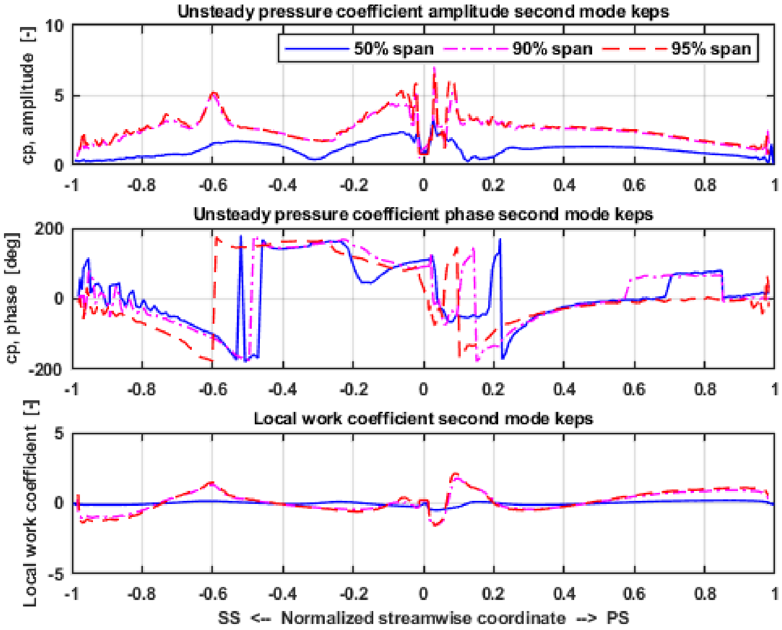

Figure 7.22: Unsteady pressure coefficient (amplitude and phase) and local work coefficient distribution for the second mode with k-epsilon model at 50%, 90% and 95% span

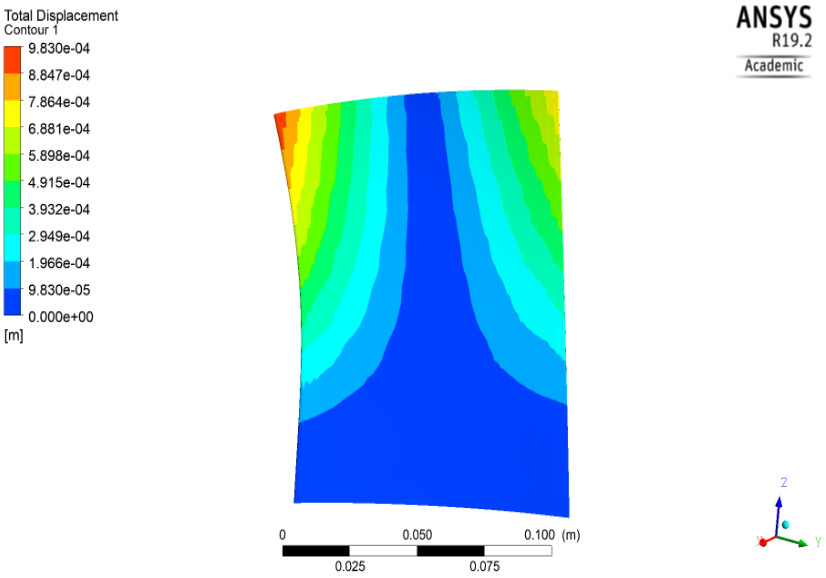

Figure 7.23: Blade displacements for the second mode

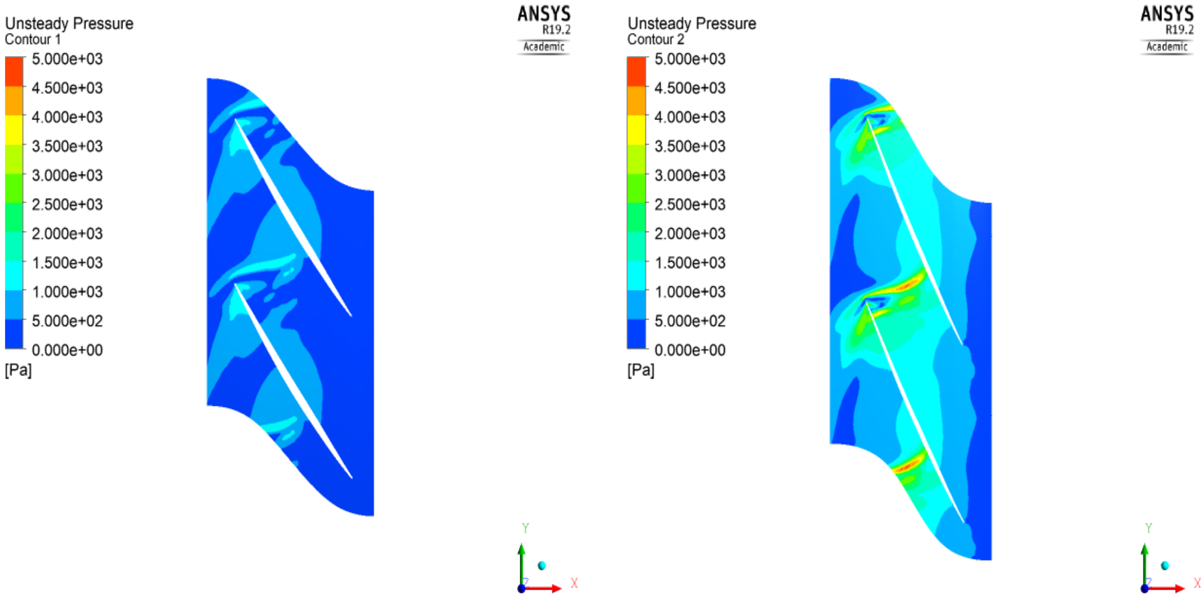

Figure 7.24: Unsteady pressure flow field for the second mode at 50% span (on the left) and 95% span (on the right)

In the second mode investigation, the highest unsteady pressure peak is again visible in the leading edge region due to the bow shock, as evident in Figure 7.22. This latter region is constituted by an alternating stable and unstable areas, as possible to see in the local work distribution. On the pressure side for this mode unsteady pressure has negligible values. At 90% and 95% span, a peak is present along the suction side at about -0.6, representative of the normal shock at mid-chord present in the aerodynamic flow field of this transonic compressor. This area does not seem leading to unstable conditions in this case. After the shock, unsteady pressure decreases on the suction side and unstable regions can be found. Again, comparing 50% span and 95% span distributions, unsteady pressure is lower in the first case and this is related to low displacements at mid-span and displacement directions working in opposition as some regions open the channel and other close it. This mode is supposed to be a first torsion (1T), as shown in Figure 7.23. The maximum displacement is found at the tip, while at 50% span displacements are halved.. Distribution at 90% span and at 95% span are very similar to each other that means low influences of tip leakage and mode shape in the top area of the blade. With respect to the first mode, unsteady pressure values are higher for this case, but this may depend on the investigated nodal diameter as it will be shown in a successive analysis.

7.6.3 Third mode with k-epsilon model

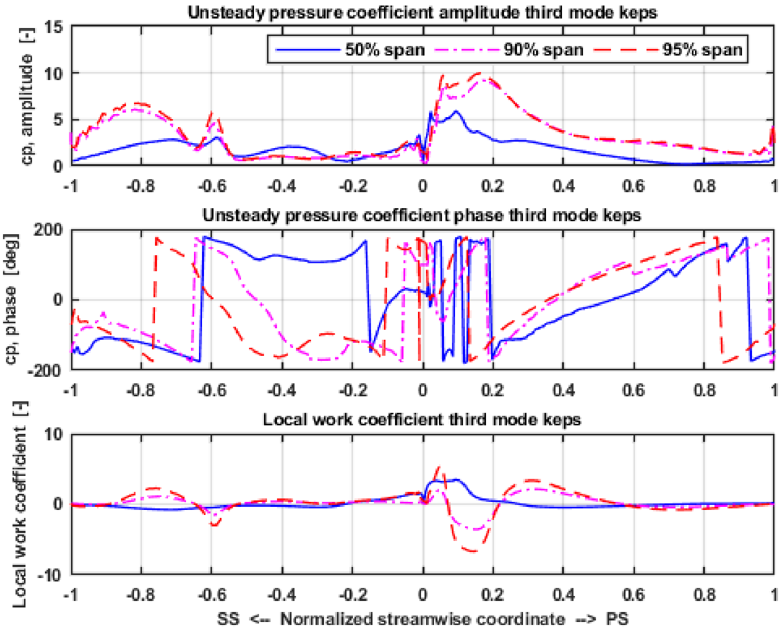

Figure 7.25: Unsteady pressure coefficient (amplitude and phase) and local work coefficient distribution for the third mode with k-epsilon model at 50%, 90% and 95% span

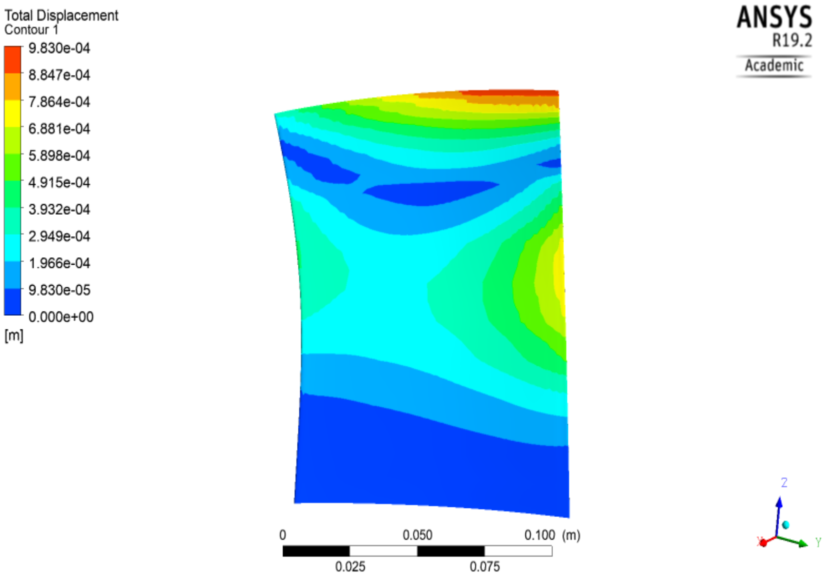

Figure 7.26: Blade displacements for the third mode

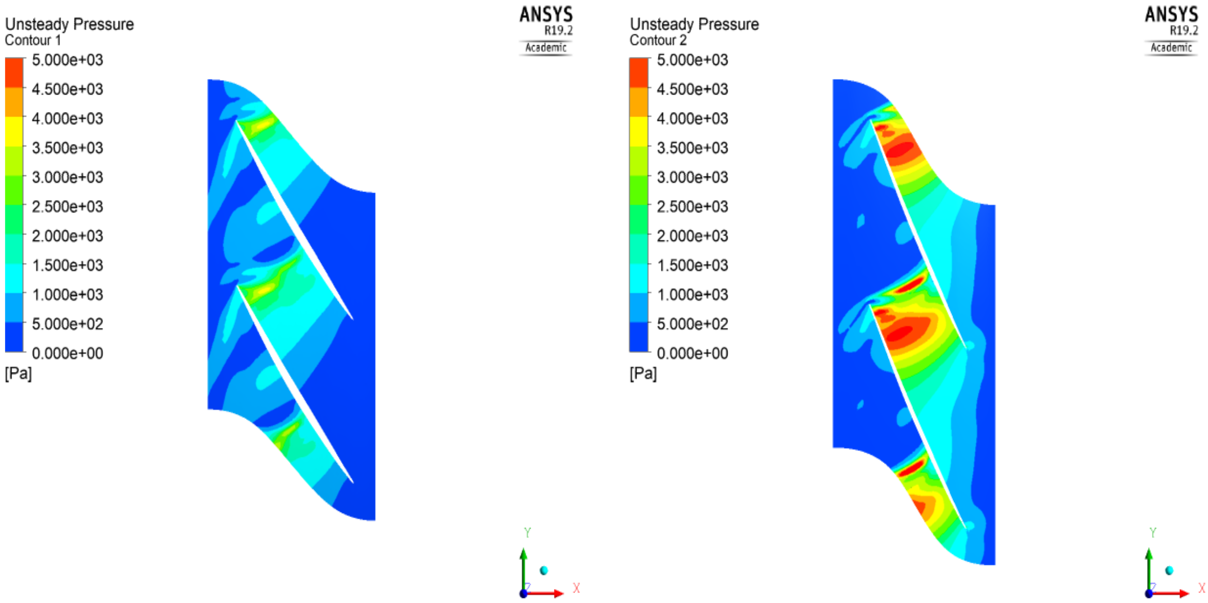

Figure 7.27: Unsteady pressure flow field for the third mode at 50% span (on the left) and 95% span (on the right)

In the third mode investigation, the highest unsteady pressure is visible at the leading edge and is higher in magnitude than the one for the other modes analyzed so far at each span location, as possible to see in Figure 7.25. In fact, pressure values showed in the unsteady pressure coefficient distribution are confirmed in Figure 7.27, where the unsteady pressure flow field is depicted. At 50% span unsteady pressure is lower in value than the ones at 90% and 95% span. At 50% a stable regions is associated to the peak at the leading edge, while an alternating region corresponds to this area for higher span locations, as possible to learn from the local work coefficient distributions. On the pressure side, pressure unsteadiness is lower than the one along the suction side for each span height. In fact, on the suction side there is again a peak at about -0.6 corresponding to the normal shock present in the steady-state analysis. At the same streamwise location, an unstable region is found. Pressure amplitude changes are driven by change in phase at the different investigated span locations. Looking at the blade displacements for the third mode, a high deformation is found at 50% span going in the opposite direction with respect to the displacement found at the tip, which is the highest one, as shown in Figure 7.26. This mode is supposed to be a second bending (2B). Differences between predictions at 90% span and 95% span is slight that means there are no influences of mode shape and tip leakage in this area. Ultimately, unsteady predictions at 50% span feature quite high unsteadiness with respect to the previous mode and this is related to the high displacement found at half blade.

7.6.4 Fourth mode with k-epsilon model

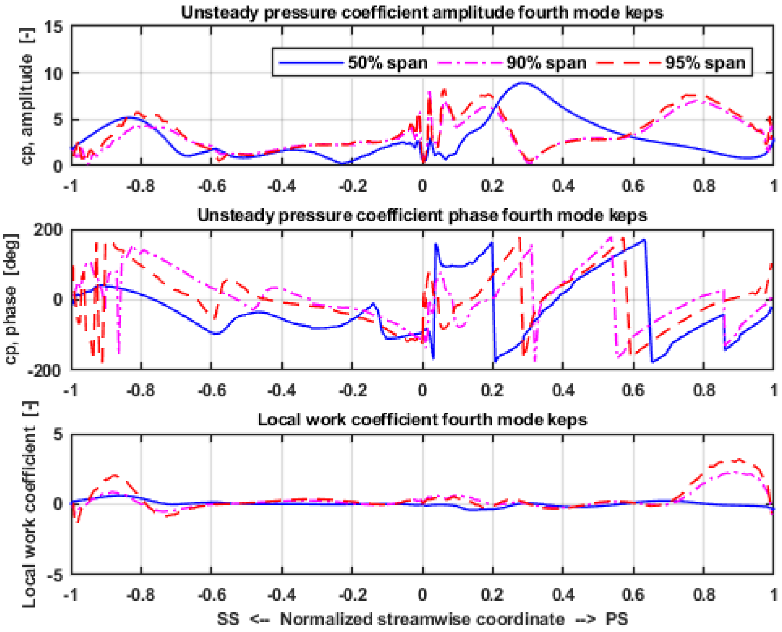

Figure 7.28: Unsteady pressure coefficient (amplitude and phase) and local work coefficient distribution for the fourth mode with k-epsilon model at 50%, 90% and 95% span

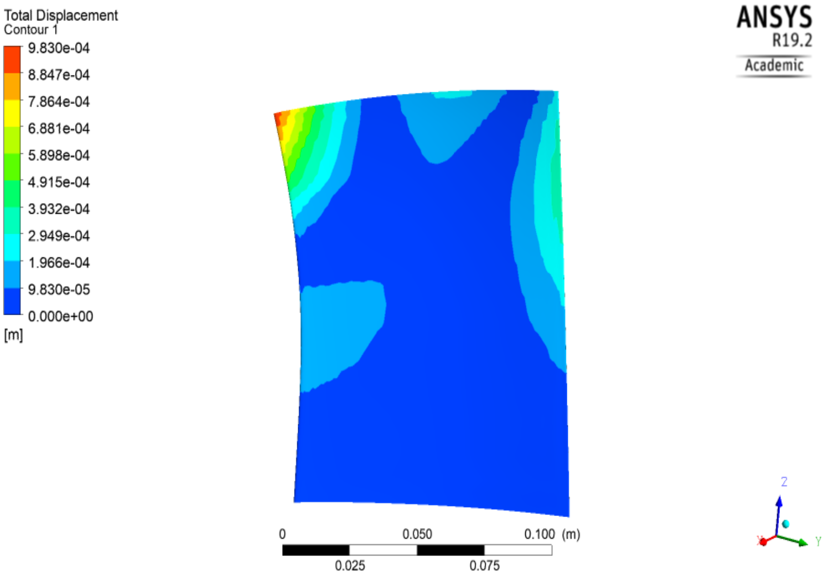

Figure 7.29: Blade displacements for the fourth mode

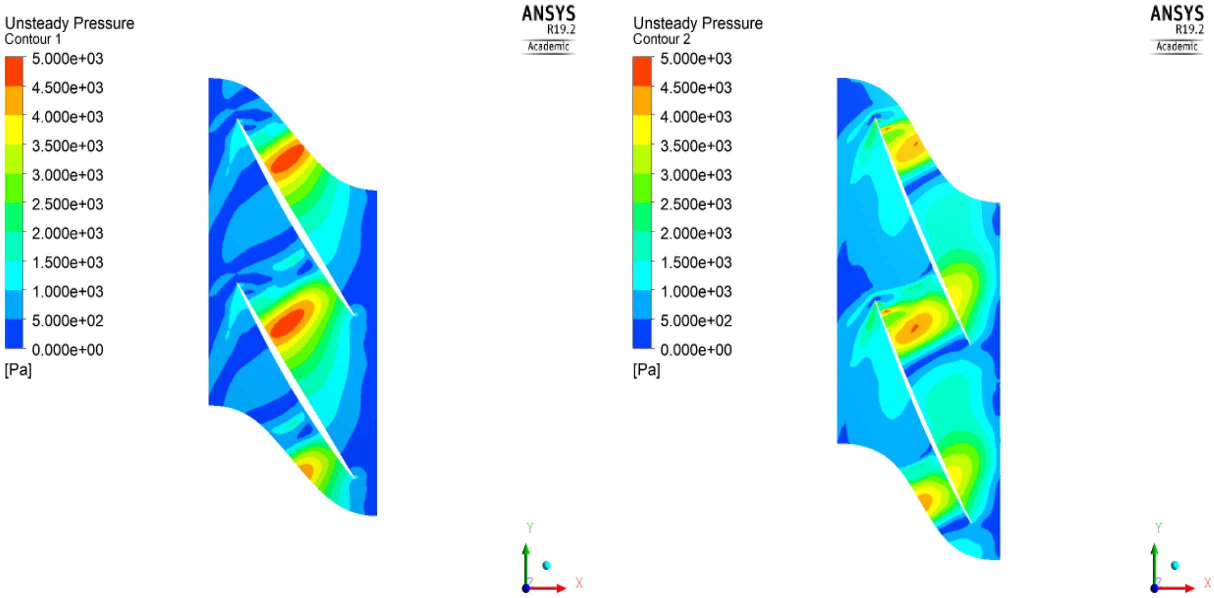

Figure 7.30: Unsteady pressure flow field for the fourth mode at 50% span (on the left) and 95% span (on the right)

In the fourth mode investigation, high unsteadiness in pressure has been found on the pressure side, as shown in Figure 7.28. For this specific case, unsteady pressure is higher at 50% span than at 95% span. This is related to blade displacement directions, typical of this mode shape, and the inter-blade phase angle equal to 21.2 degrees for $ND = 3$. In particular, at 50% span and about 0.3 along the pressure side a high unsteady pressure is found due to high displacement at the trailing edge of the previous blade, which opens the channels, Figure 7.30. Magnitude of displacements, visible in Figure 7.29, is quite low at mid-span, but in this case, displacements direction leads to a very high pressure unsteadiness. Another peak of comparable magnitude at 95% span and about 0.8 along the pressure side is identified. Along the suction side unsteadiness appears lower in values, except for another peak found at- 0.8 almost equal in magnitude for each span height. This mode is supposed to be edgewise bending (1E). In the local work coefficient plot, it is possible to notice two peaks in the stable region for 90% and 95% span predictions, one at about 0.9 along the pressure side and the other at about -0.9 along the suction side. This means at this location displacements and unsteady pressure values are the highest one, as it is possible to notice form the blade displacements and unsteady pressure flow field.

7.6.5 Fifth mode with k-epsilon model

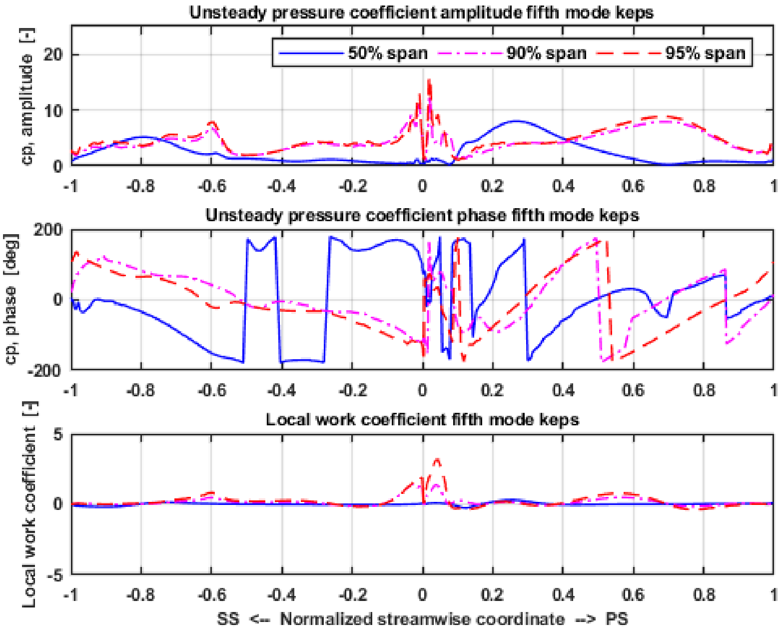

Figure 7.31: Unsteady pressure coefficient (amplitude and phase) and local work coefficient distribution for the fifth mode with k-epsilon model at 50%, 90% and 95% span

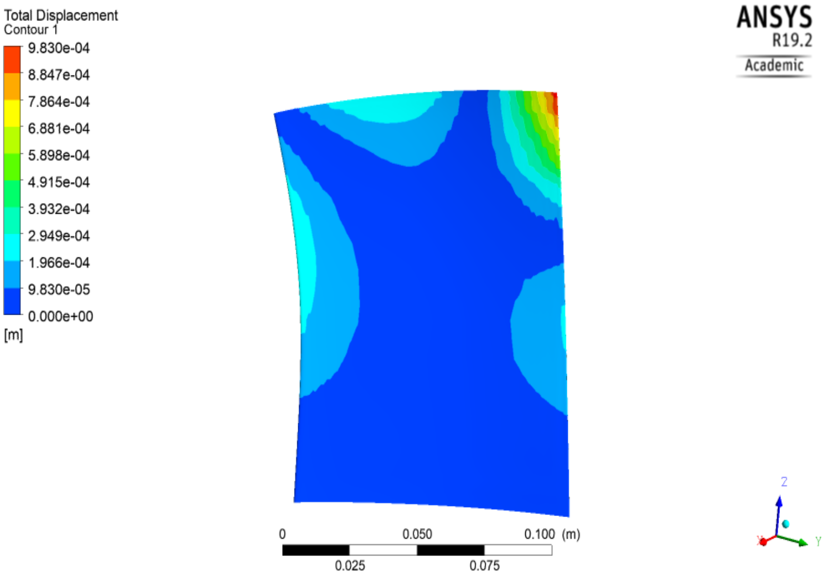

Figure 7.32: Blade displacements for the fifth mode

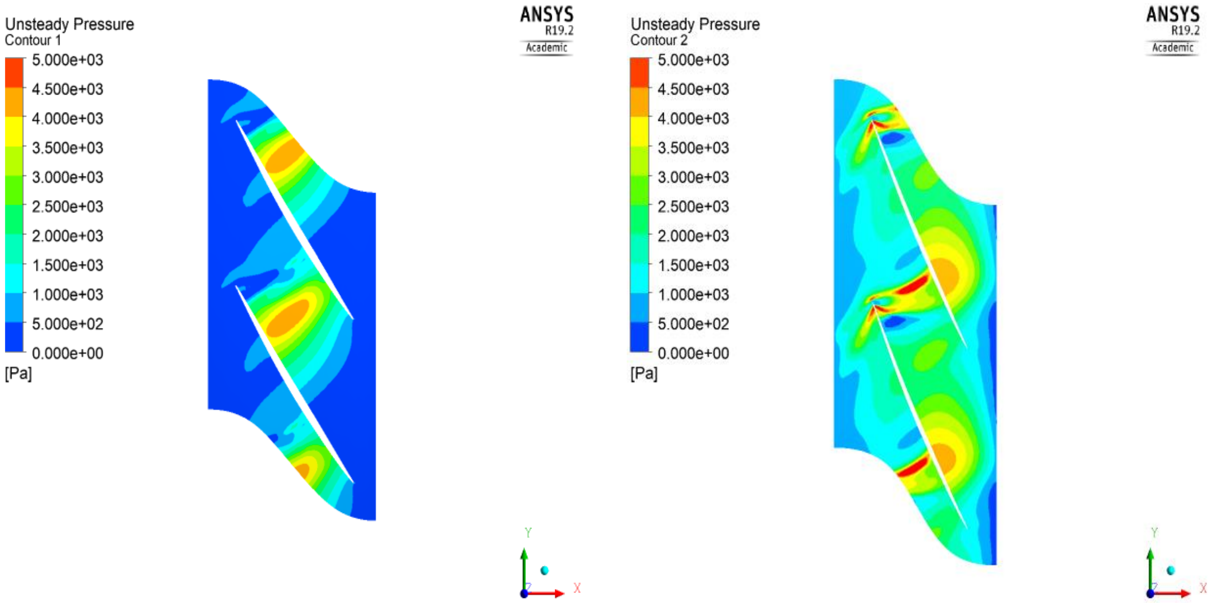

Figure 7.33: Unsteady pressure flow field for the fifth mode at 50% span (on the left) and 95% span (on the right)

In the fifth mode investigation, the highest pressure peak is found at 90% and 95% span in the leading edge region, as evident in Figure 7.31. Another peak is identified at around 0.7 along the normalized streamwise coordinate for the same span locations. At 50% span, lower unsteady pressure values have been found, except at 0.3 along the pressure side due to the inversion of the motion and an opening in the channels, as possible to see in Figure 7.31. At the leading edge for this span location there is no direct impingement of the flow. This mode shape is supposed to be a second torsion (2T), with an inversion of displacement vectors near mid-span location. In Figure 7.33, the overview of the unsteady pressure flow field is depicted, useful to assess the previous plots. The suction side at 50% span features lower unsteady pressure values, except at -0.8, where the same unsteadiness present on the pressure side at around 0.3 of the adjacent blade is found. For higher span location, there is still a peak at -0.6 along the pressure side due to the normal shock at mid-chord.

7.6.6 Sixth mode with k-epsilon model

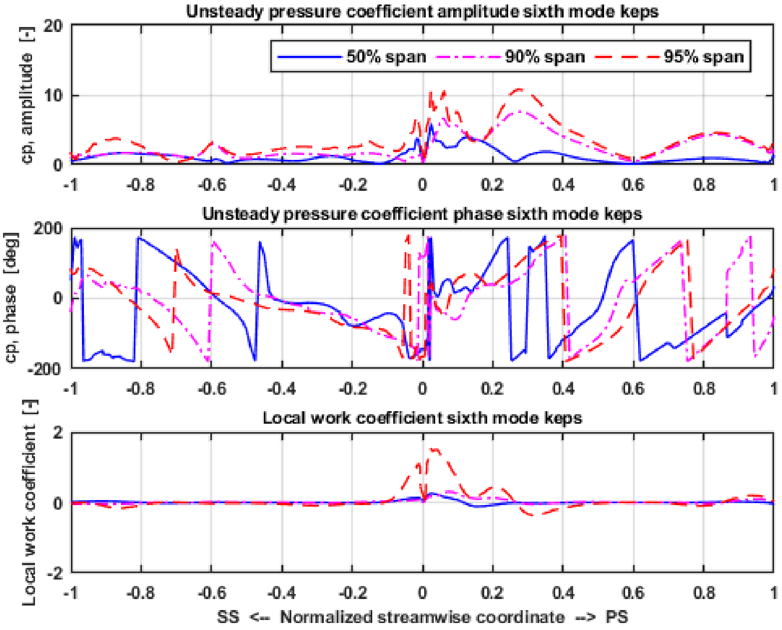

Figure 7.34: Unsteady pressure coefficient (amplitude and phase) and local work coefficient distribution for the sixth mode with k-epsilon model at 50%, 90% and 95% span

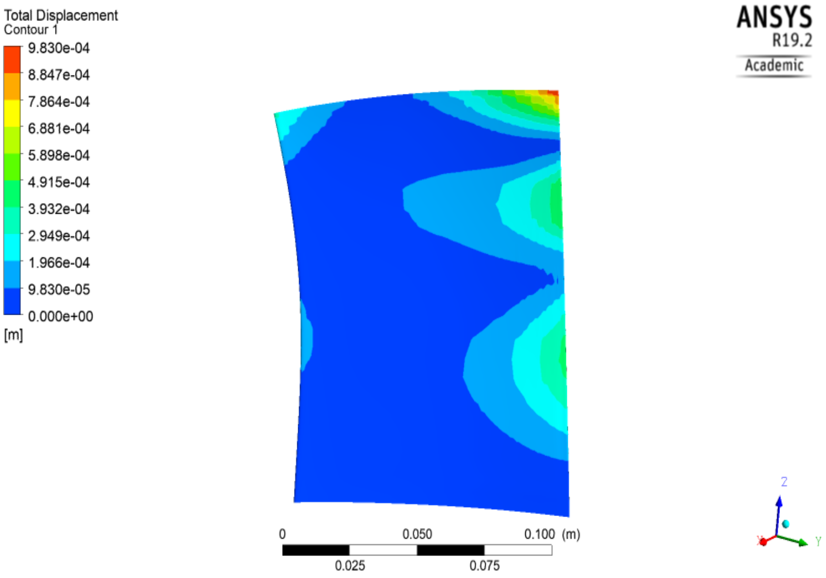

Figure 7.35: Blade displacements for the sixth mode

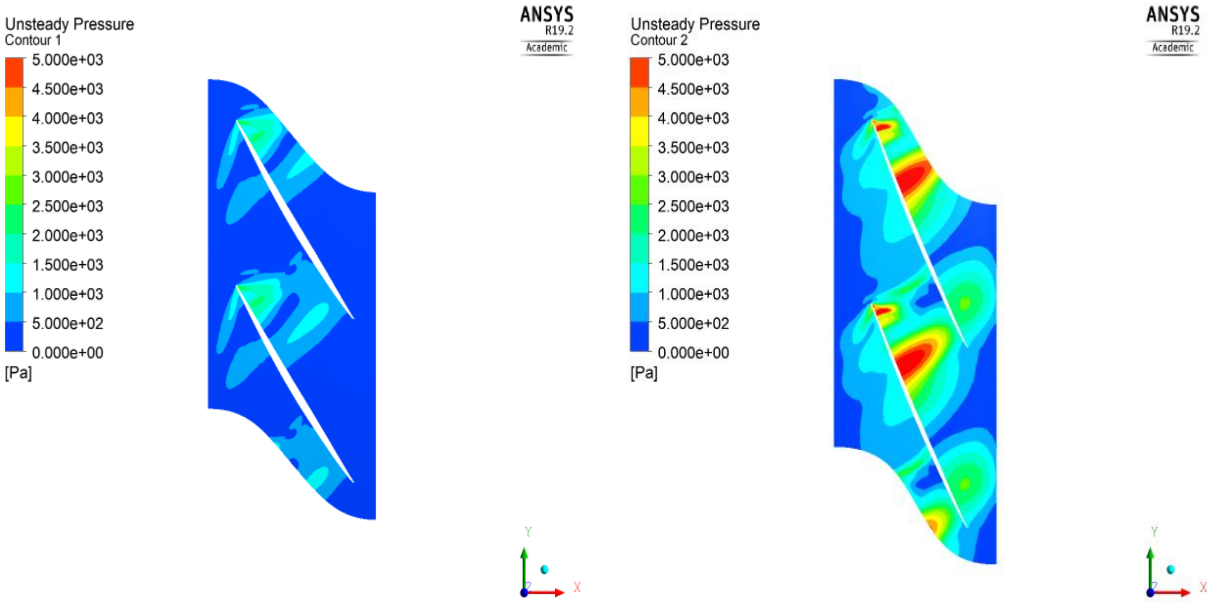

Figure 7.36: Unsteady pressure flow field for the sixth mode at 50% span (on the left) and 95% span (on the right)

In the sixth mode investigation, higher unsteady pressure peaks have been found at leading edge and at 0.3 along the pressure side at 95% span, as possible to see in Figure 7.34. Another peak with lower magnitude is identified at about 0.8 on the same blade side and span location. Predictions at 50 % span feature lower values due to low displacement in this case, as evident in blade displacements in Figure 7.35. This mode is supposed to be third bending (3B). In Figure 7.36, the unsteady pressure flow field for the sixth mode is presented and it is evident as the unsteady pressure values at 50% span are lower in magnitude than values at 95% span. Another feature could be noticed by looking at the local work coefficient distribution. In particular there is considerable difference between 90% span and 95% span and this is related to the mode shape. In fact, displacements are higher in correspondence of the tip and become lower at 90% span leading to a lower unsteady pressure. The peak at leading edge is less pronounced for this span location.

7.6.7 Unsteady pressure overview for all the modes

For all the modes presented in the previous paragraphs, unsteady pressure distributions can be plotted in a compact version in order to discuss about differences among the different cases at different span locations. As possible to see in Figure 7.37 and 7.38, at 50% span the fourth mode presents the highest unsteadiness at about 0.3 along the pressure side, with a value around $4500\ Pa$. Higher pressure amplitudes at this span location are representative of the cases in which the coupling between amplitude and direction of the mode shape is such as to produce these values. At 95% span, instead unsteady pressure magnitudes should be more comparable as the highest amplitude has been found for all the modes. In Figure 7.39 and 7.40, these latter comparisons are depicted. An interesting issue is related to the first mode, which is the only case featuring lower amplitude than in the other cases. This can be linked to the particular configuration, in which the coupled system, disk and blade, is involved, in terms of the analyzed nodal diameter (least stable condition) and unsteady pressure phase. Further investigation has been successively performed for this case. The highest pressure value at the tip is around $8000\ Pa$ for the fifth mode case.

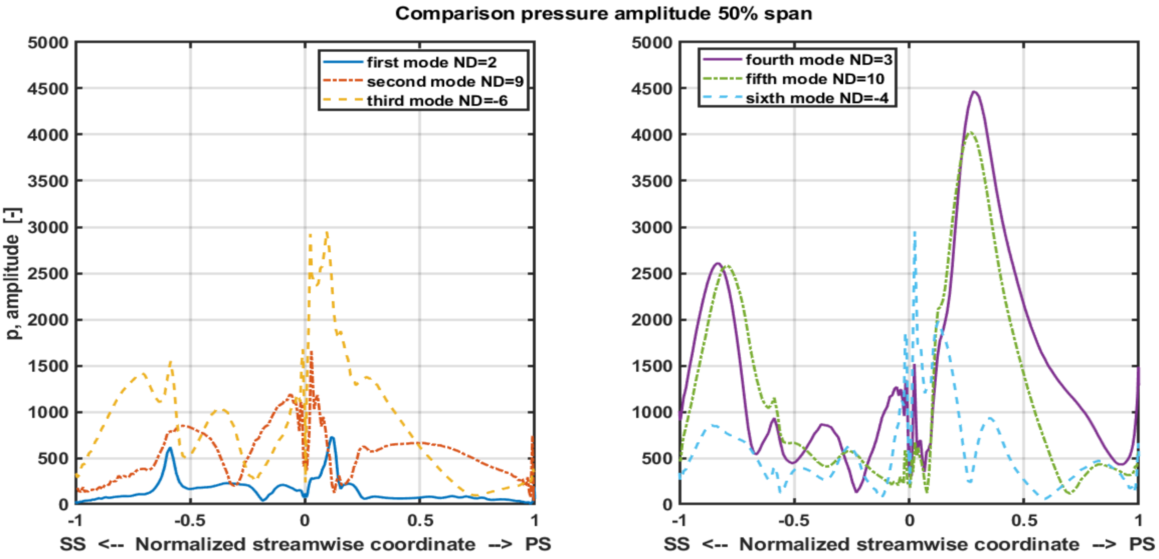

Figure 7.37: Unsteady surface pressure amplitude overview for all modes at 50% span

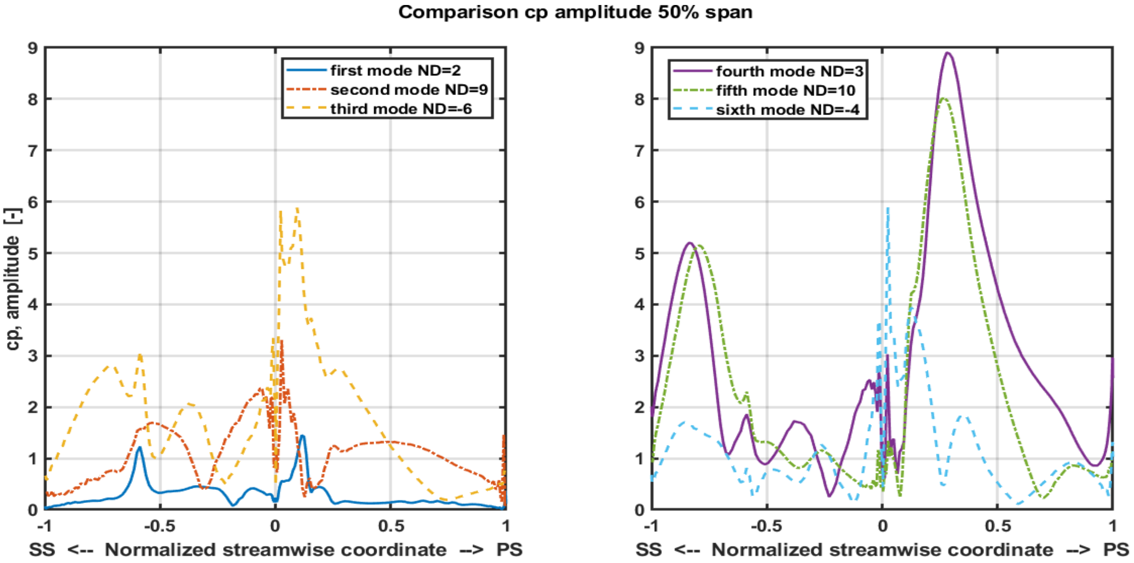

Figure 7.38: Unsteady surface pressure coefficient amplitude overview for all modes at 50% span

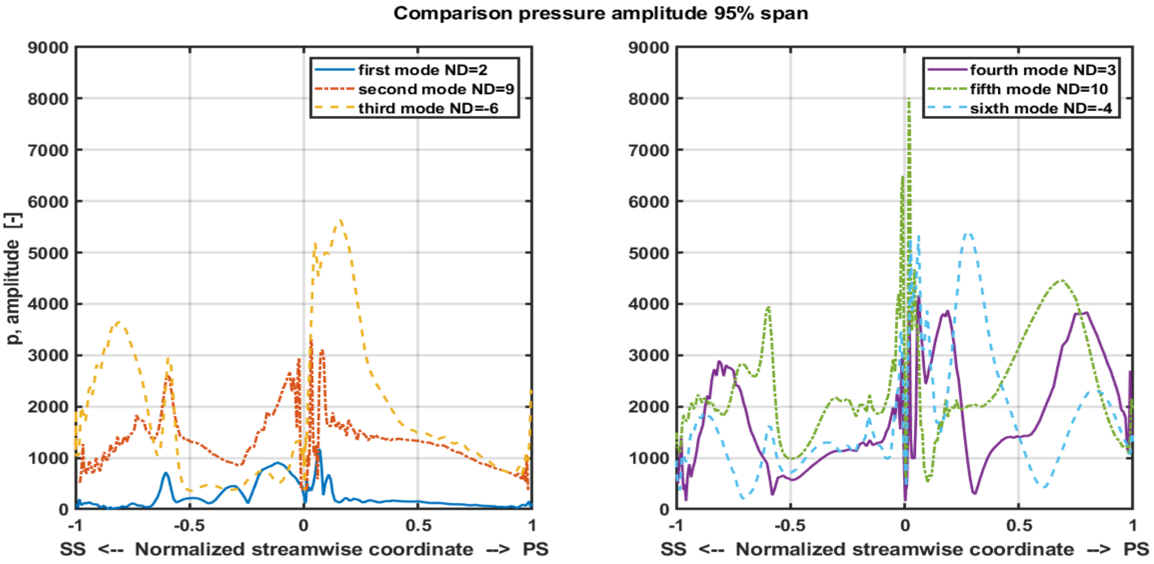

Figure 7.39: Unsteady surface pressure amplitude overview for all modes at 95% span

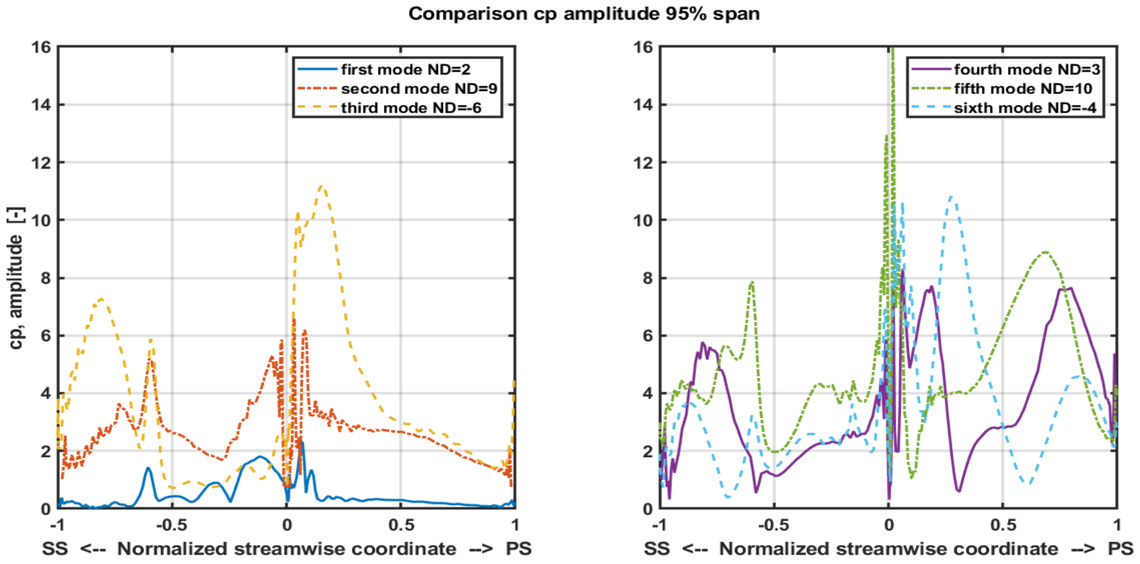

Figure 7.40 : Unsteady surface pressure coefficient amplitude overview for all modes at 95% span

7.7 First mode investigation

Due to the previous comparison for all the modes showing lower values of the unsteady pressure coefficient amplitude for the first mode at 95% span, several nodal diameters have been investigated at the same blade displacement in order to get a fair overview of the unsteady pressure magnitude in this case. Another investigation, performed for the first mode, is the one varying the turbulence model, as previously shown for the S-shape curve. In this latter case, unsteady pressure and local work coefficient distribution have been further computed for the least stable condition $(ND = 2)$ in order to understand the influence of the turbulence model on these predictions.

7.7.1 ND investigation

As evident in Figure 7.40, when IBPA is higher and far away from the least stable condition unsteady pressure amplitude gets higher. It is possible to notice that first mode case features unsteady pressure amplitude even higher than the cases compared in the previous overview. Further phase investigations have been carried out for $ND = 3$ and $ND = -15$ with respect to the least stable mode $(ND = 2)$ in order to try to get insights into the causes related to this large shift in magnitude. In fact, unfavorable phase usually can drive to changes in amplitude and may cause unstable conditions if the pressure vector changes quadrant in the imaginary plane, such in the flutter case, where unsteady pressure leads to an increase in displacements.

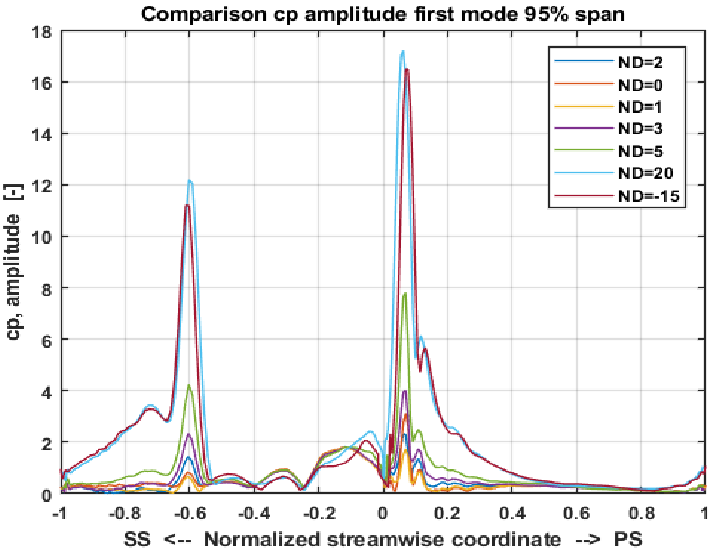

Figure 7.41: Comparison for the first mode at 95% span for different nodal diameters

In Figure 7.42, a first comparison between $ND = 2$ and $ND = 3$ is depicted. These two configurations are close to each other and feature almost the same $IBPA$, equal to $14.12°$ and $21.18°$ respectively; thus changes in amplitude, phase and local work are quite small. In particular, the case of $ND = 3$ features higher peaks, but with the same trend of the quantities under consideration. In Figure 7.43, instead, a considerable phase shift has been identified between the two configurations. IBPA is equal to $-105.88°$ for $ND = -15$. At about -0.6 and 0.1 along the normalized streamwise coordinate, larger amplitude changes have been found. These two areas are the most critical ones, which feature for the least stable condition unstable regions, as possible to see in the local work coefficient distribution. For $ND = -15$, these regions get more stable and thus farther away from the flutter limit, as confirmed in the S-shape curve as well. Therefore, it can be concluded that as function of the nodal diameter, amplitude and phase are combined together giving certain values; it is meaningful to compare several configurations in order to get a better overview of unsteady pressure value for a certain mode.

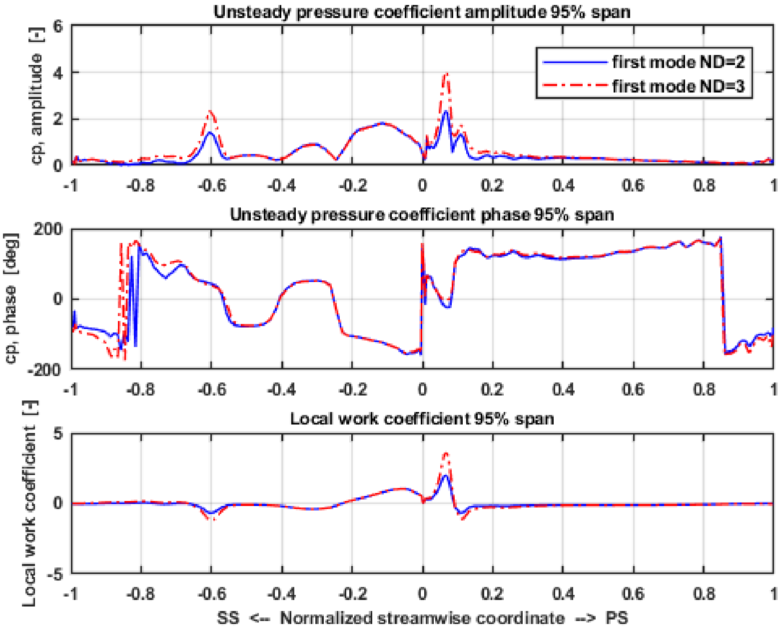

Figure 7.42: Unsteady comparison for the first mode at 95% span between $ND = 2$ and $ND = 3$

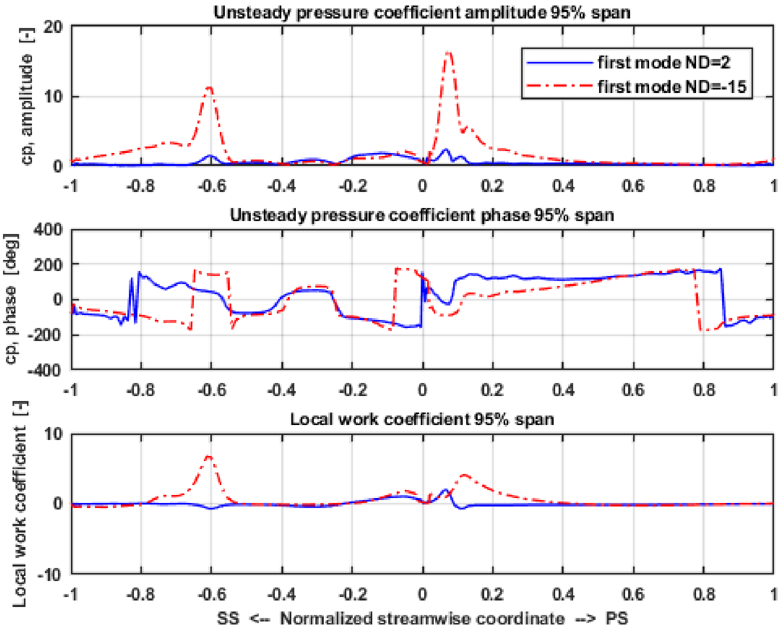

Figure 7.43: Unsteady comparison for the first mode at 95% span between $ND = 2$ and $ND = -15$

7.7.2 Turbulence model investigation

Since the shocks at mid-chord on the suction side and at leading edge predicted in the steady-state analysis result less sharp when SST model is used, an unsteady investigation has been performed for the least stable mode. In the previous logarithmic decrement comparison, a deviation higher than 25% has been found between the two aerodamping values in the same configuration. In Figure 7.44, it is possible to see almost the same trend for both turbulence model, but in general lower unsteady pressure values at each span height for the SST model case. This is confirmed in Figure 7.45, where the local work coefficient distribution shows lower peaks for SST model case. Therefore, the unsteady prediction supports the steady state prediction for shocks at leading edge and at -0.6 along the suction side, which feature lower values. Moreover, since the unsteady prediction for the first mode in terms of S-shape curve, unsteady pressure and local work coefficient distribution is similar for both cases and no significant differences can be pointed out, this comparison is limited to this case.

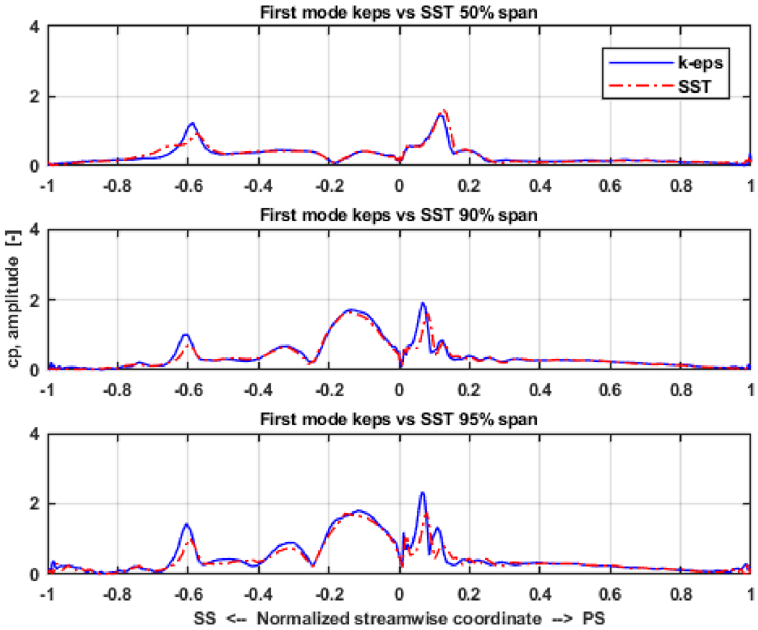

Figure 7.44: Unsteady pressure coefficient distribution for the first mode comparing k-epsilon and SST turbulence model

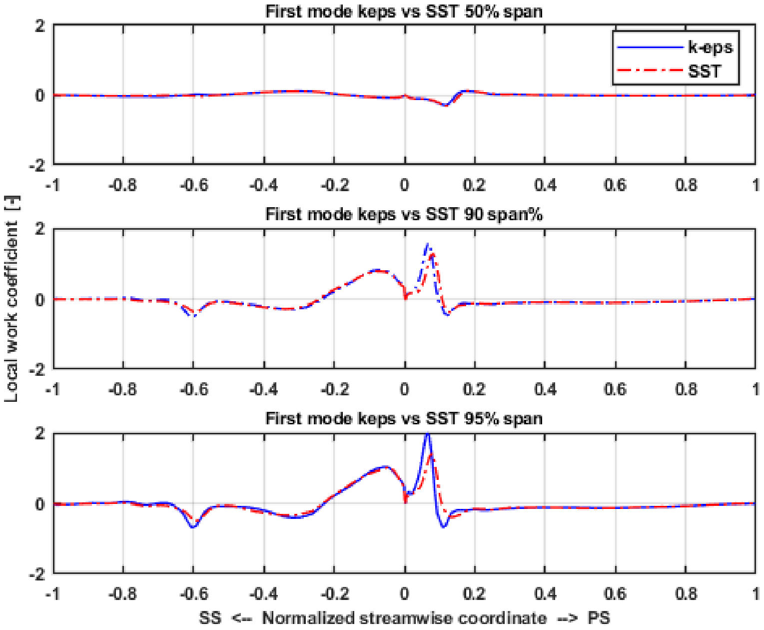

Figure 7.45 : Local work coefficient distribution for the first mode comparing k-epsilon and SST turbulence model

7.8 Fourth mode investigation

Different unsteady investigations have been conducted for the fourth mode in the least stable condition $(ND = 3)$ in order to assess the unsteady pressure prediction at 95% span previously discussed. In particular, a convergence study based on CFX predictions and a scaling factor analysis are the most relevant results obtained for this case.

7.8.1 CFX convergence study

Several simulations have been performed for the fourth mode using the same number of time steps, equal to 68, but stopping each simulation at a different simulation period. This analysis enables to compare different convergence levels with the one at P=35, which features a Peak -to-Peak and a Steady-value torque error equal to 0. A convergence error study has been performed by taking into account the highest point at about 0.2 along the normalized streamwise coordinate for each simulation period, as possible to see in Figure 7.46.

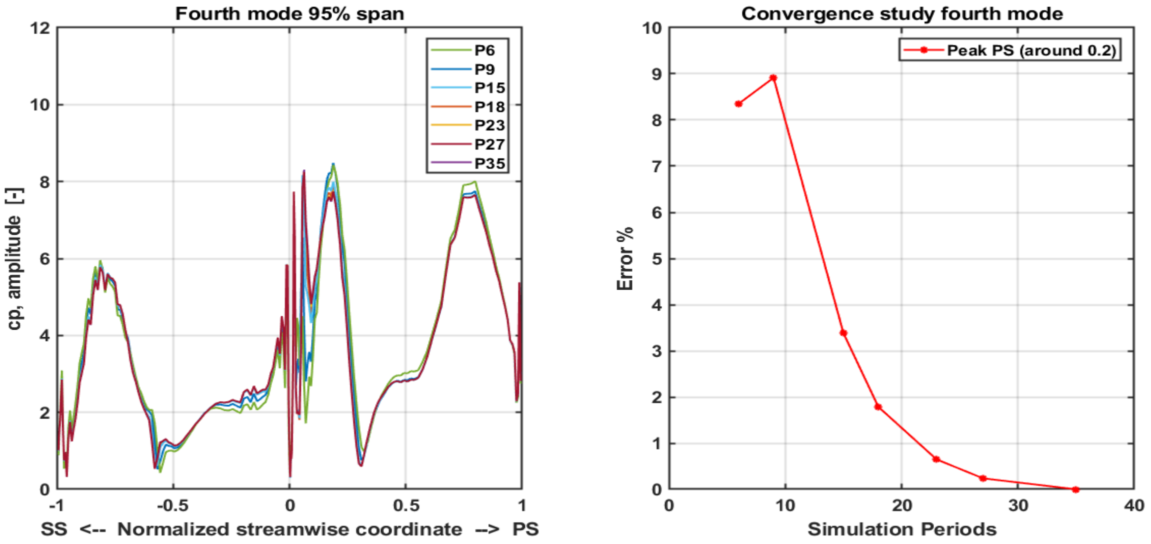

Figure 7.46: Unsteady pressure predictions for several periods in the fourth mode case

In particular, it is possible to state that after P=15 a fair convergence level is going to be reached. In fact, the unsteady pressure prediction starts to become the same even extending the simulation for more periods. A deeper investigation has been carried out by computing Peak-to-Peak and Steady-Value torque error for each of these simulations, which quantify the convergence level. As expected and evident in Figure 7.46, lower values start to occur for P=18, characterized by $P2P = 0.03\%$ and $SV = 0.012\%$. In particular for P=18, it is possible to see the last marked variation in the torque steady value, after which an high convergence tending to 0% is being reached and the aerodynamic damping deviation between the two adjacent blades becomes smaller.

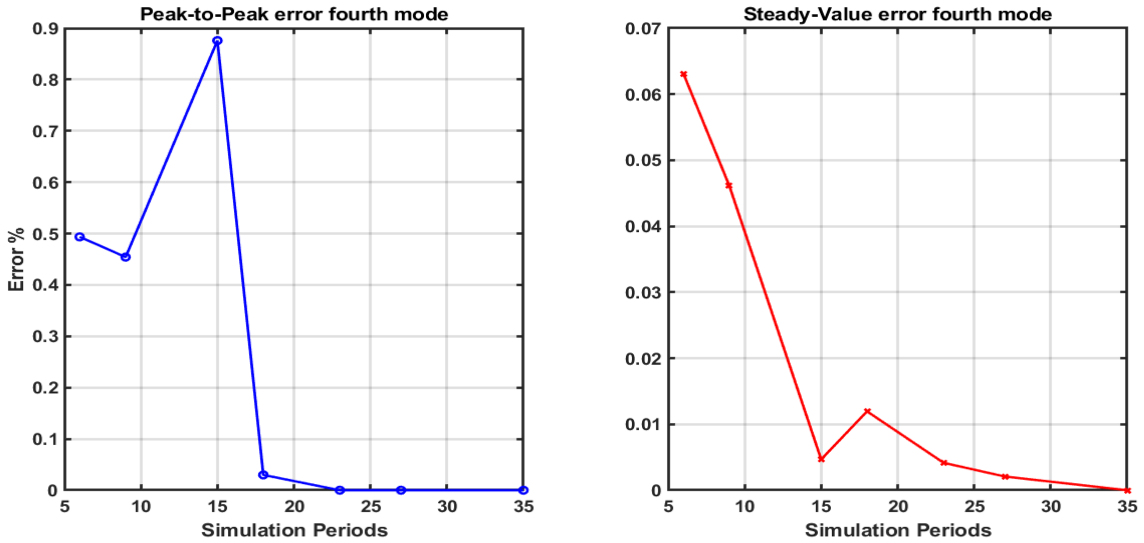

Figure 7.47: Peak-to-Peak and Steady-Value torque error for fourth mode simulations

7.8.2 Scaling factor analysis

Blade motion is prescribed in ANSYS CFX by setting the scaling factor, which allows to substitute the modal displacement with another one, suitable for the software. For each simulation so far, this parameter has been set equal to 1% of the blade chord. This creates pressure unsteadiness in the transonic flow field, proportional to the displacement value. In line with this principle, doubled or halved unsteady pressure values should be obtained by setting a doubled or halved scaling factor. Hence two further simulations with the same setup, except for the scaling factor equal to 2% and 0.5% of the chord respectively, have been performed. Unsteady pressure results at 95% span are shown in Figure 7.47.

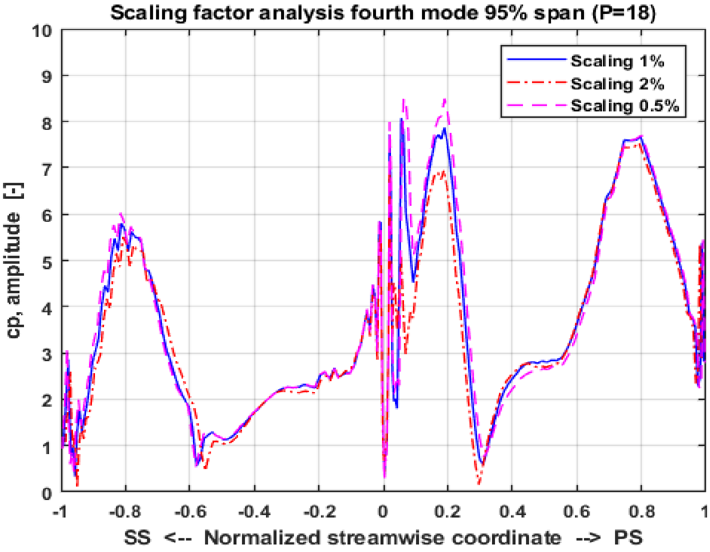

Figure 7.48: Unsteady pressure predictions for several scaling factors in the fourth mode case

This analysis shows some mismatches in the unsteady pressure coefficient distributions, which should be completely in agreement since each prediction has been scaled with the respective scaling factor used for simulating. At about 0.2 along the normalized streamwise coordinate, the mismatch with respect to the reference prediction has been quantified for both cases. These discrepancy values are 0.56% for a halved scaling factor and 1.62% for a doubled scaling factor. The interesting issue is that even though CFX is a linearized CFD code, some non-linearities are highlighted in this study, therefore future investigations can focus on these numerical phenomena.

7.9 Fourier transformation investigation

All the predictions showed so far have been obtained with the Fourier transformation method implemented in ANSYS CFX. In the present analysis, these results have been compared with the ones obtained extracting quantity values in time and computing Fourier transformation in MATLAB, in order to monitor the goodness of CFX predictions. A MATLAB function computes the discrete Fourier transform (DFT) of a vector using a fast Fourier transform (FFT) algorithm. The flow field solution varying in time has been extracted from CFX-Solver by saving backup files at each time step. Every quantity of interest has been after transformed from time to frequency domain. Two different strategies have been implemented for each simulation. In particular, CFX unsteady pressure prediction has been compared with the one obtained either by the Fourier transformation of the last period or by the Fourier transformation of the complete time evolution filtering out the first 3 periods. Discrepancy between CFX and MATLAB predictions has been evaluated taking as reference CFX prediction in certain reference location for each mode:

- first and second mode: highest pressure as reference;
- third mode: pressure at leading edge as reference;
- fourth mode: pressure at 0.8 along the pressure side as reference.

In light of these investigations it is possible to state that for convergence below a certain value CFX prediction is equal to the MATLAB one taking the last period values for performing Fourier transformation. This means CFX predictions are quite reliable because they make use of converged pressure values.

7.9.1 Fourier transformation for first mode

Backup files have been collected for the first mode until P=9. The agreement is better for the first strategy, where the Fourier transformation is computed only on the last period and when the convergence level is higher in each case, as possible to see in Figure 7.48 ad 7.49. Percentage errors calculated with respect to CFX prediction for the reference point are equal to:

- Last-period strategy at P=6: error % = 9.02%
- Complete range strategy at P=6: error % = 13.42%
- Last-period strategy at P=9: error % = 0.20%
- Complete range strategy at P=9: error %= 0.96%

The discrepancy gets below 0.5% at P=9 for the last-period strategy, thus the simulation can be considered converged at this level.

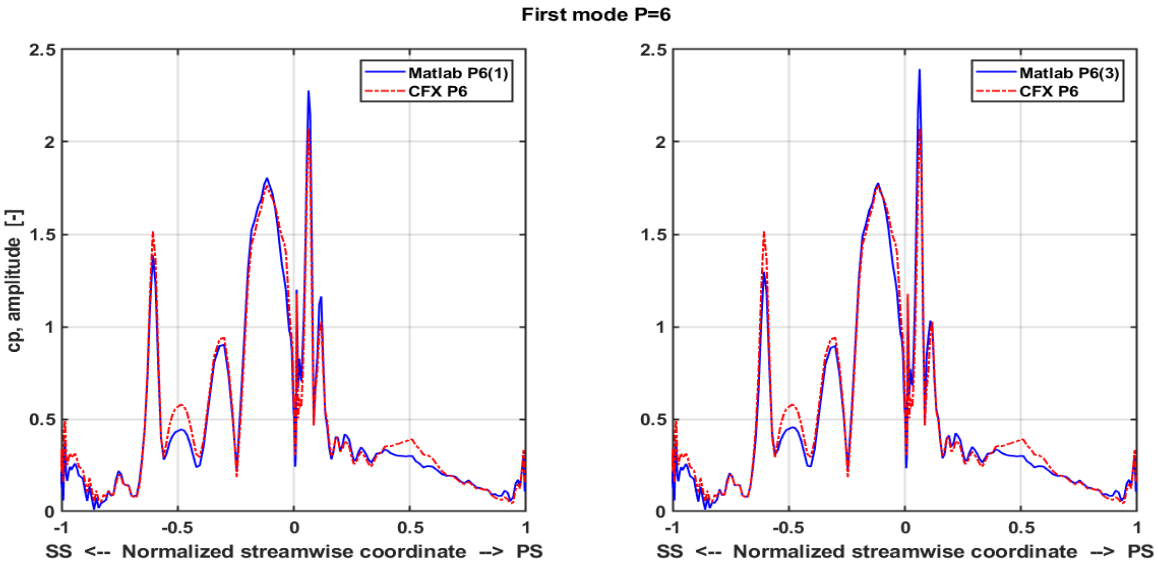

Figure 7.49: Fourier transformation comparisons for the first mode at P=6

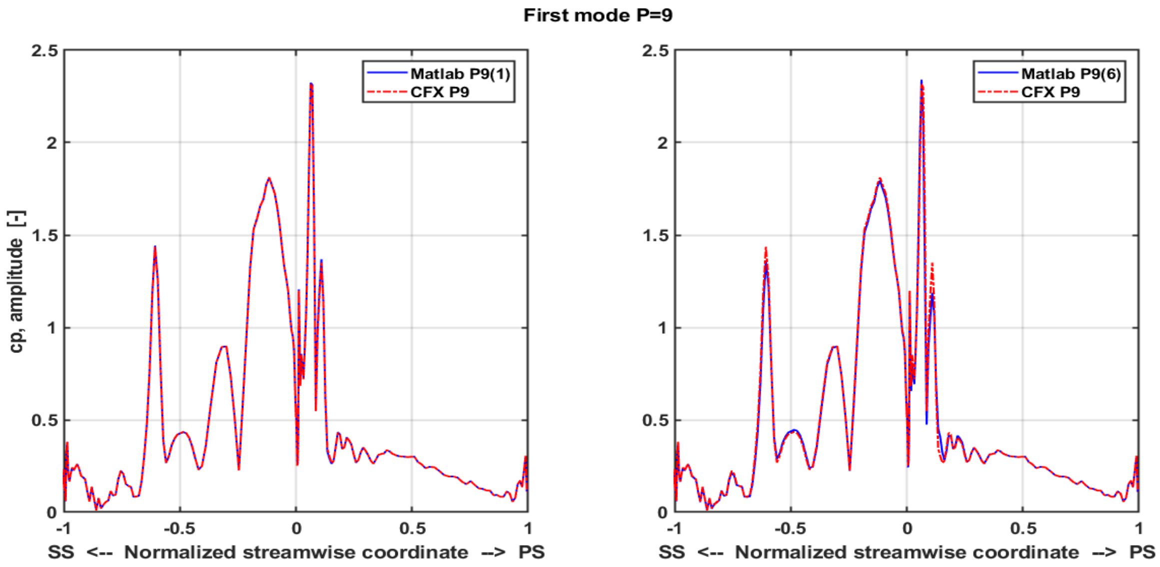

Figure 7.50: Fourier transformation comparisons for the first mode at P=9

7.9.2 Fourier transformation for second mode

Backup files have been collected for the second mode until P=14. The agreement is better for the first strategy, where the Fourier transformation is computed only on the last period and when the convergence level is higher in each case, as possible to see in Figure 7.50 ad 7.51. Percentage errors calculated with respect to CFX prediction for the reference point are equal to:

- Last-period strategy at P=9: error % = 0.42%
- Complete range strategy at P=9: error % = 2.95%
- Last-period strategy at P=14: error % = 0.07%
- Complete range strategy at P=14: error % = 2.64%

The discrepancy gets below 0.5% at P=9 and below 0.1% at P=14 for the last-period strategy, thus the simulation can be considered converged at this level.

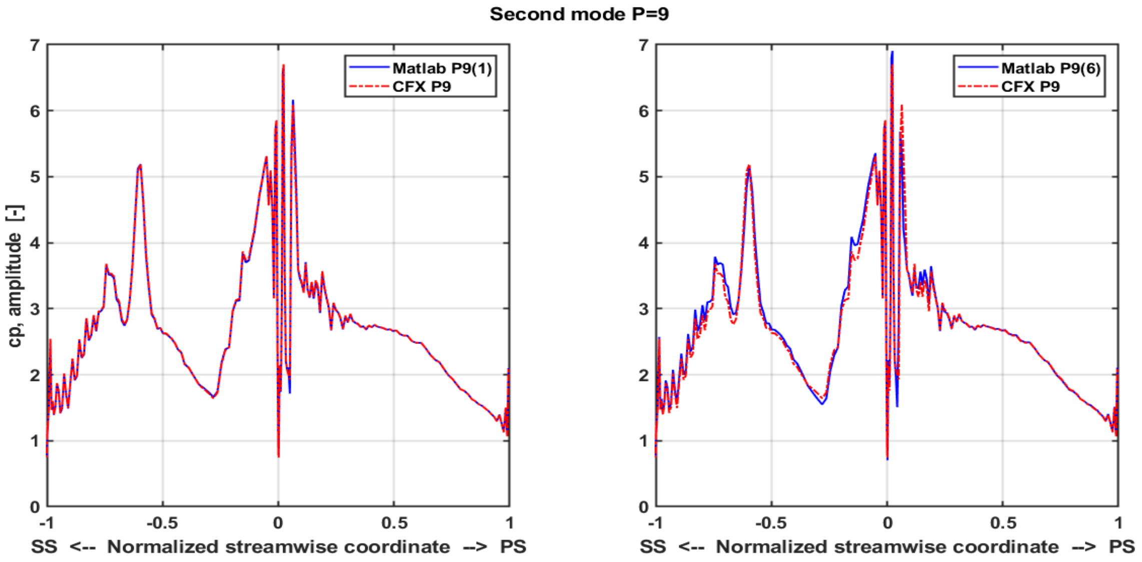

Figure 7.51: Fourier transformation comparisons for the second mode at P=9

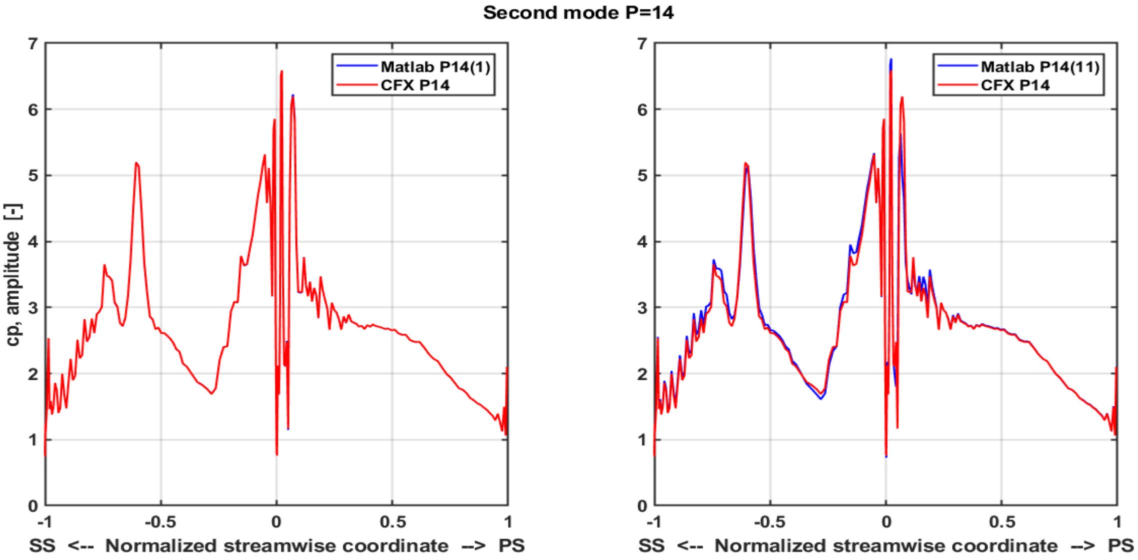

Figure 7.52: Fourier transformation comparisons for the second mode at P=14

7.9.3 Fourier transformation for third mode

Backup files have been collected for the third mode until P=14. The agreement is better for the first strategy, where the Fourier transformation is computed only on the last period and when the convergence level is higher in each case, as possible to see in Figure 7.52 ad 7.53. Percentage errors calculated with respect to CFX prediction for the reference point are equal to:

- Last-period strategy at P=9: error % = 2.24%
- Complete range strategy at P=9: error % = 10.84%
- Last-period strategy at P=14: error % = 0.51%
- Complete range strategy at P=14: error % = 12.39%

The discrepancy gets around 0.5% at P=14 for the last-period strategy, thus the simulation can be considered converged at this level.

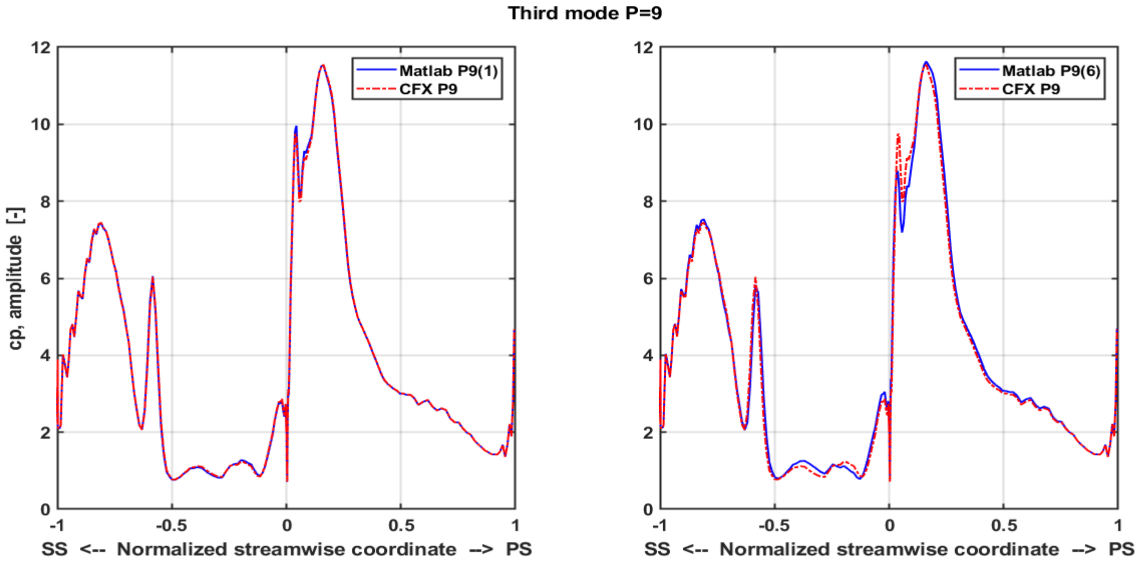

Figure 7.53: Fourier transformation comparisons for the third mode at P=9

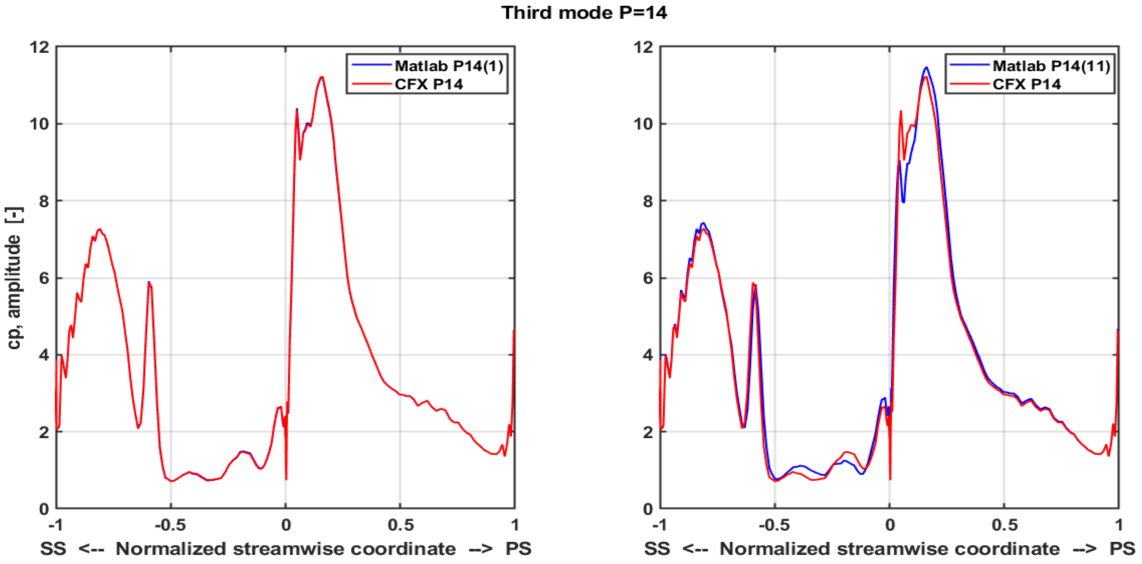

Figure 7.54: Fourier transformation comparisons for the third mode at P=14

7.9.4 Fourier transformation for fourth mode

Backup files have been collected for the fourth mode until P=23. The agreement is better for the first strategy, where the Fourier transformation is computed only on the last period, and when the convergence level is higher in each case, as possible to see in Figure 7.54, 7.55, 7.56, 7.57 and 7.58. Percentage errors calculated with respect to CFX prediction for the reference point are equal to:

- Last-period strategy at P=6: error % = 1.64%
- Complete range strategy at P=6: error % = 2.99%
- Last-period strategy at P=9: error % = 0.26%
- Complete range strategy at P=9: error % = 3.18%
- Last-period strategy at P=15: error % = 0.03%
- Complete range strategy at P=15: error % = 2.31%

- Last-period strategy at P=18: error % = 0.02%
- Complete range strategy at P=18: error % = 1.98%
- Last-period strategy at P=23: error % = 0.002%
- Complete range strategy at P=23: error % = 1.54%

The discrepancy gets below 0.5% at P=9, below 0.05% at P=15 and lastly one order of magnitude less at P=23 for the last-period strategy. The simulation can be considered converged after P=15, as previously stated in the convergence study performed for the fourth mode.

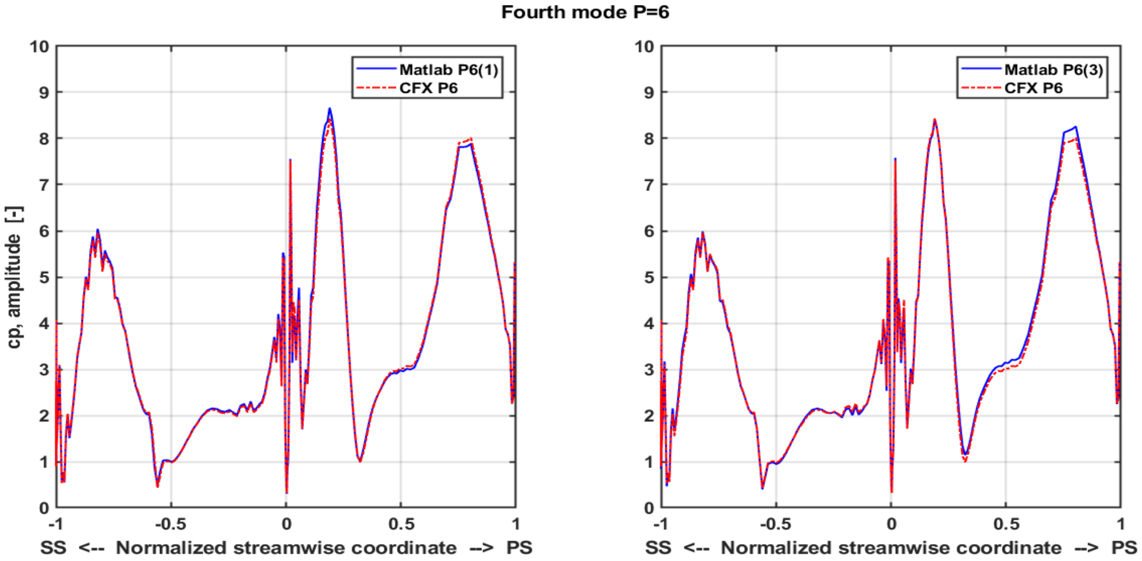

Figure 7.55: Fourier transformation comparisons for the fourth mode at P=6

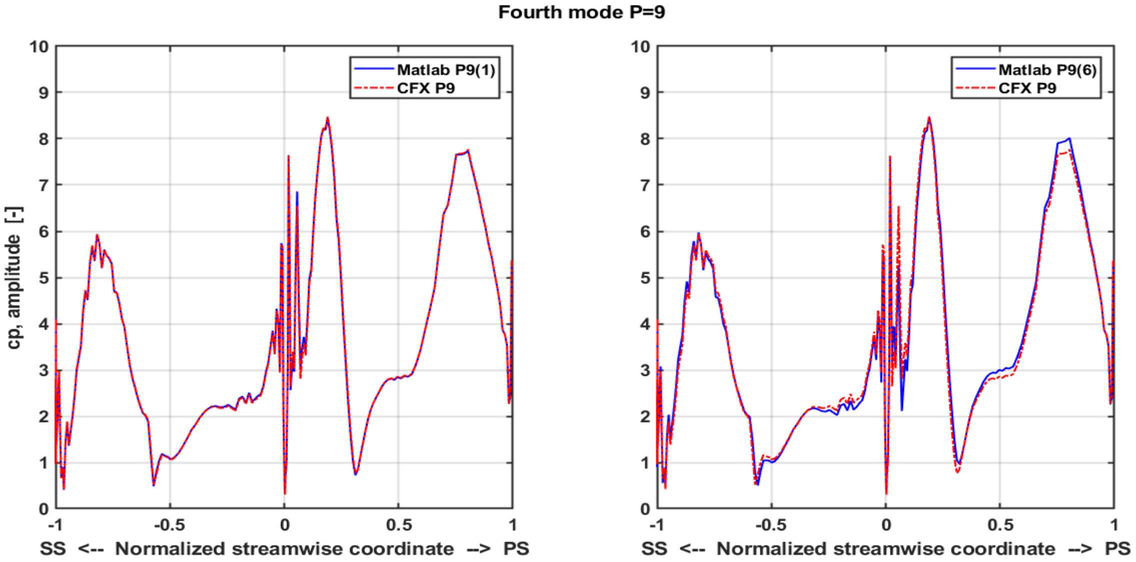

Figure 7.56: Fourier transformation comparisons for the fourth mode at P=9

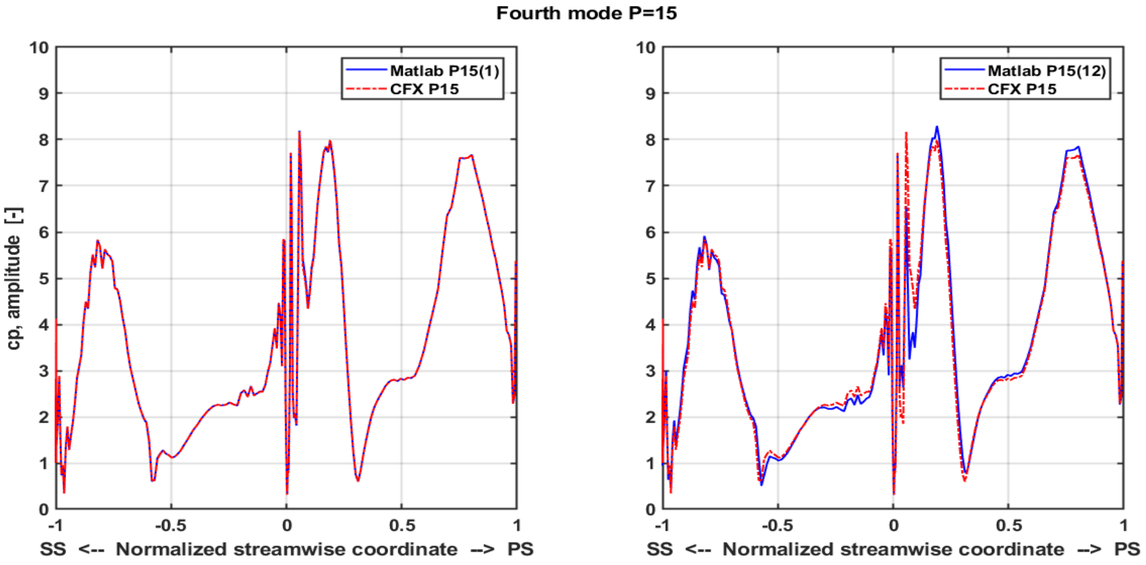

Figure 7.57: Fourier transformation comparisons for the fourth mode at P=15

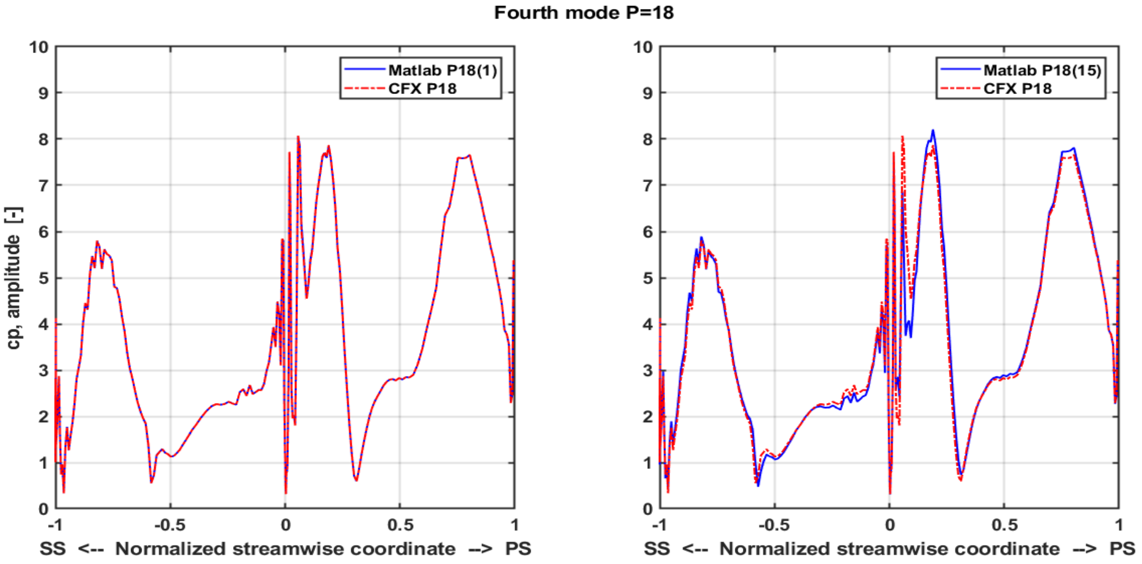

Figure 7.58: Fourier transformation comparisons for the fourth mode at P=18

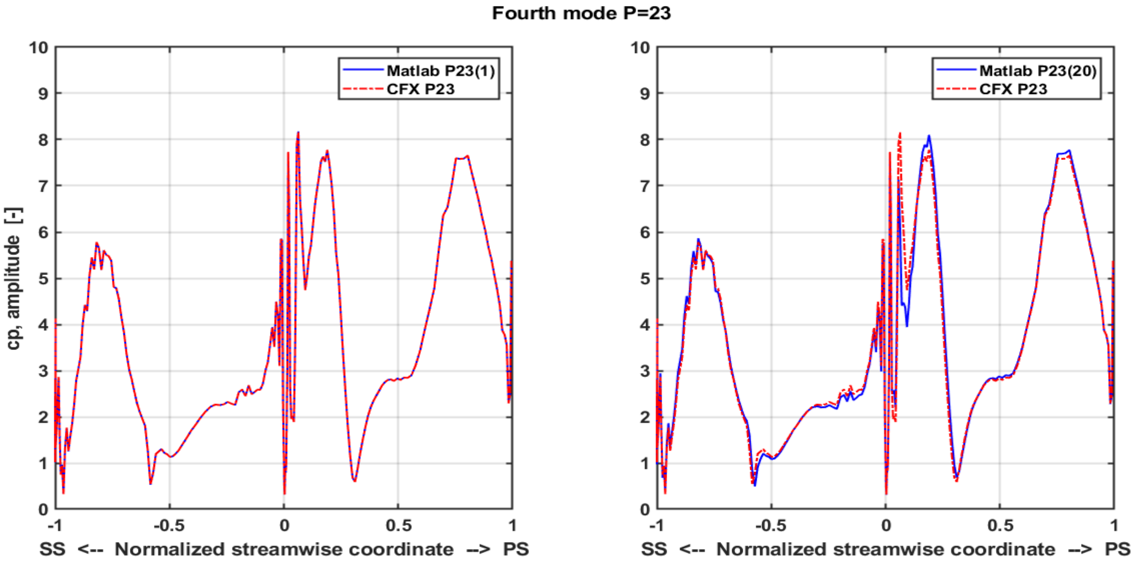

Figure 7.59: Fourier transformation comparisons for the fourth mode at P=23

7.9.5 Other Fourier transformation trials for first mode

Another issue is that when convergence level is not that high (discrepancy value above 0.5% for last-period strategy as discussed in Paragraph 7.9.1), as possible to see in Figure 7.48 of the previous paragraph about the first mode, agreement between CFX and MATLAB unsteady pressure predictions is poorer than in case in which the convergence level is higher. Several strategies have been implemented in order to try to get the CFX Fourier transformation, but some divergences have been found. In particular, Fourier transformation of the last period, the last two periods, the last three periods and the last four periods have been compared with the CFX one.

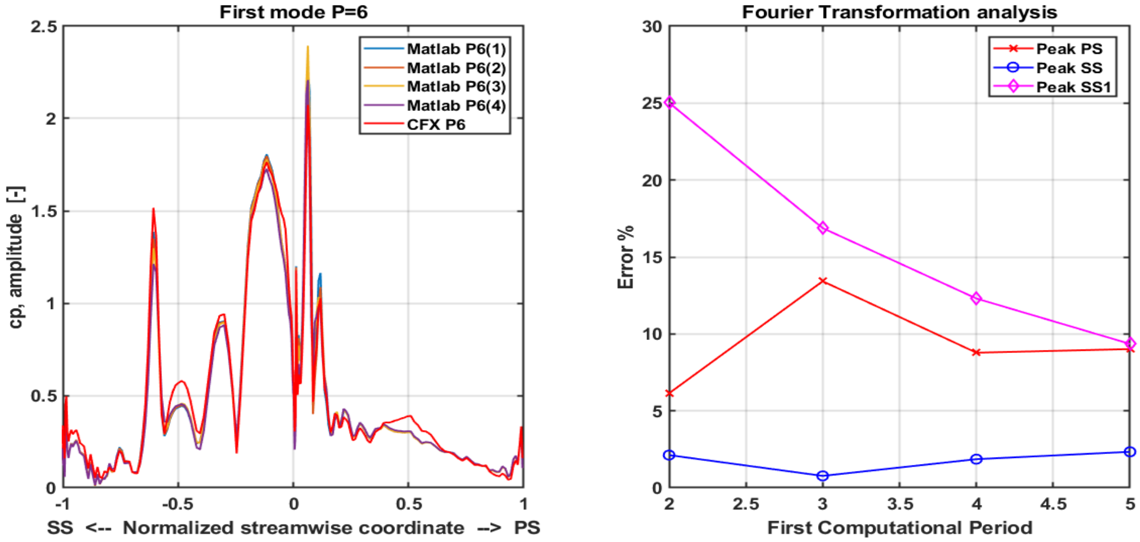

Figure 7.60: Other Fourier transformation comparisons for the first mode at P=6

In Figure 7.59, Peak PS is the point on the pressure side at around 0.2, Peak SS is the point on the suction side at around -0.2 ad Peak SS1 is the one on the suction side at about -0.6. First computational period means the first period, where Fourier transformation starts to be computed in MATLAB. For example, the trial “Matlab P6(4)” in the plot on the left corresponds to the percentage error computed for a first computational period equal to 2 in the plot on the right. None of these trials is in complete agreement with the CFX prediction, taken as reference to calculate the percentage error. Peak SS is the point where the agreement is better, while the other points feature larger discrepancies. By computing the Fourier transformation of the last period, it is possible to find the optimal case, even if for a first computational period of 4, lower errors have been found for Peak PS and Peak SS with respect to the last case.

7.10 Harmonic balance comparisons

The previous numerical predictions have been performed using the Time Integration transient method, in which the flow solution obtained via a time-marching method with a large frequency content and captures most of the flow characteristics. The amount of frequency content and flow details captured by transient flow are controlled by the true time-step size or the number of time steps per period. In the Harmonic Balance case, the solution contains only the frequency associated with targeted fundamental frequencies and retained harmonics. In fact, the targeted fundamental frequency, such as the blade passing frequency, is usually known in advance. Frequencies that are not associated with the blade passing frequency are not known before obtaining the HB solution and therefore are not captured. In this case, gains in computational effort are not considerable, since the reduction in time is in the order of some hours. Predictions coming from this method confirm the trend found by the Time Integration transient method. This means retaining only one harmonics $(M = 1)$ is a fair approximation to solve the unsteady transonic flow filed associated to the compressor rotating row under consideration. In Figure 7.60, 7.61, 7.62 and 7.63 comparisons of the S-shape curve for each mode are depicted. In Figure 7.64, 7.65, 7.66 and 7.67 unsteady pressure coefficient comparisons at each span height have been conducted, showing a fair matching for each configuration. The reference Time integration predictions are the ones stopped at P=9 compared with the one for HB case with $M = 1$. Other information on the HB setup can be found in the methodology section.

7.10.1 S-shape comparisons

Logarithmic decrement distributions obtained with the Harmonic Balance method are in agreement with the ones obtained with the time integration methods. Deviations between the two models have been stated for each case in order to identify configurations where the logarithmic decrement values are different. For the first and fourth mode the same least stable condition have been found in both cases, even if it is present an high deviation for the first mode case in this configuration, as possible to see in Figure 7.60. For the fifth and sixth mode, instead, the least stable mode is different between the two cases, as evident in Figure 7.62 and 7.63. In particular for the fifth mode, the least stable mode has been found in the same region, while for the sixth mode the least stable mode is now in the positive range of nodal diameters for the HB case. In fact, in correspondence of these regions for the fifth and sixth mode, higher values of deviation have been identified.

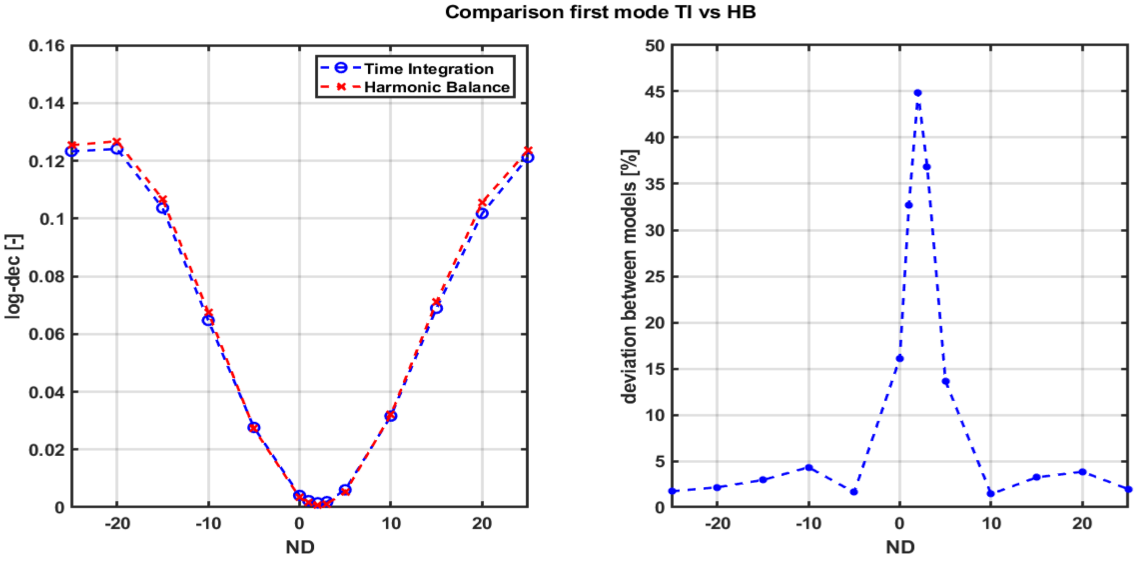

Figure 7.61 : Logarithmic decrement distribution for the first mode comparing time integration and harmonic balance transient methods

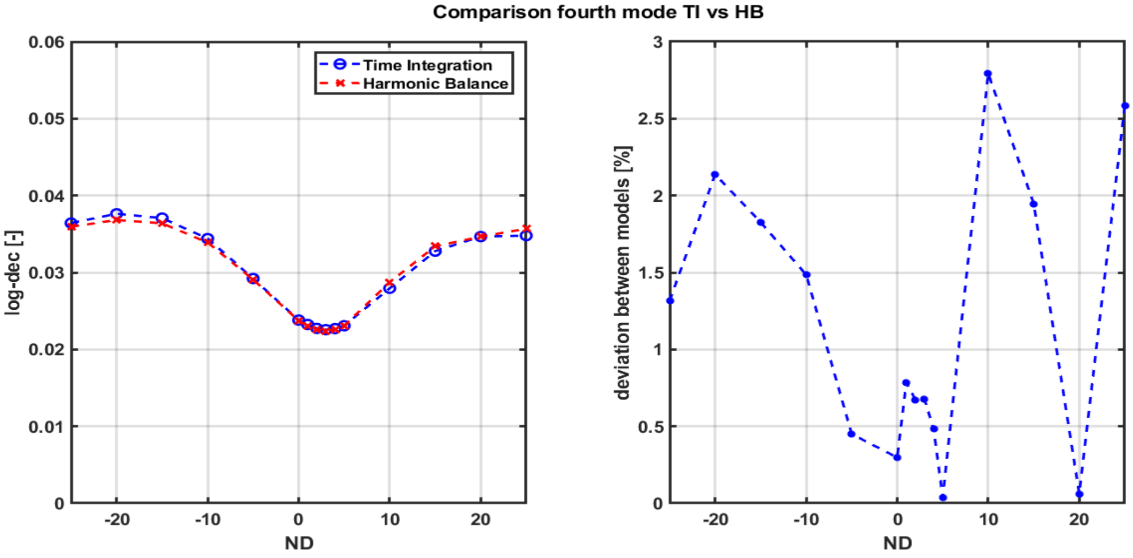

Figure 7.62: Logarithmic decrement distribution for the fourth mode comparing time integration and harmonic balance transient methods

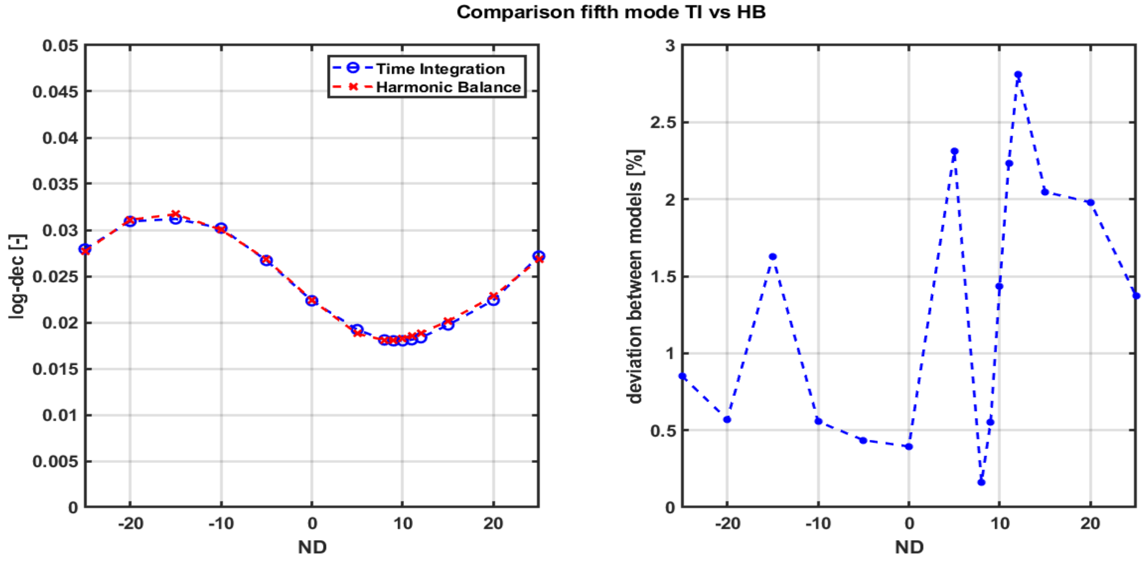

Figure 7.63: Logarithmic decrement distribution for the fifth mode comparing time integration and harmonic balance transient methods

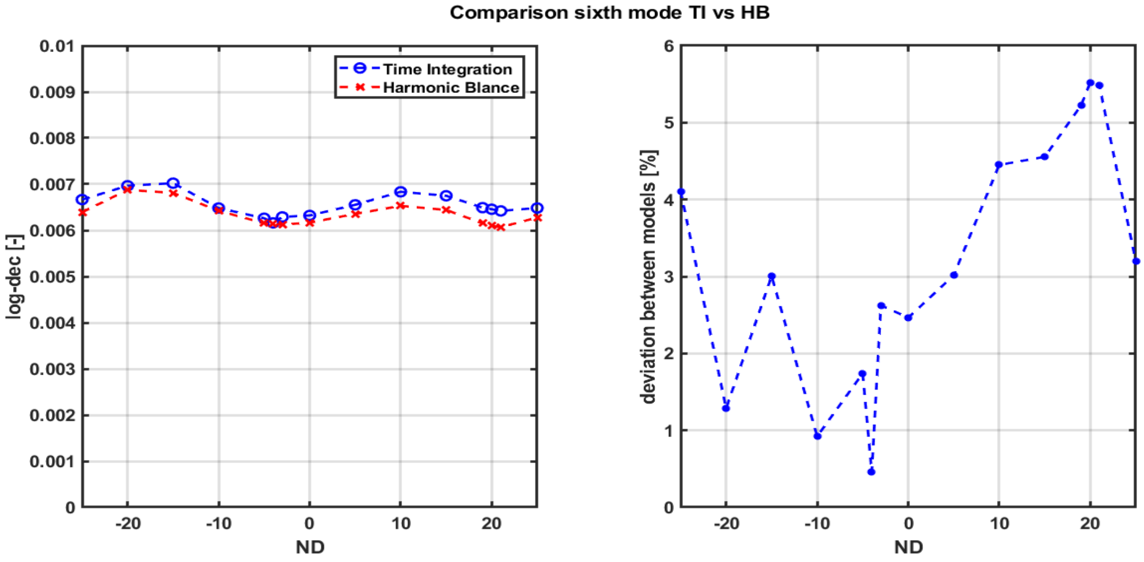

Figure 7.64: Logarithmic decrement distribution for the sixth mode comparing time integration and harmonic balance transient methods

7.10.2 Unsteady pressure coefficient comparisons

Unsteady pressure distribution for the least stable condition of the Time Integration case is compared with the same configuration for HB case. Discrepancy in these predictions are quite negligible and are associated to the previous deviations stated for the S-shape curve. This means Harmonic Balance method is an accurate transient method of prediction for this rotating blading, even if not all the frequencies are captured.

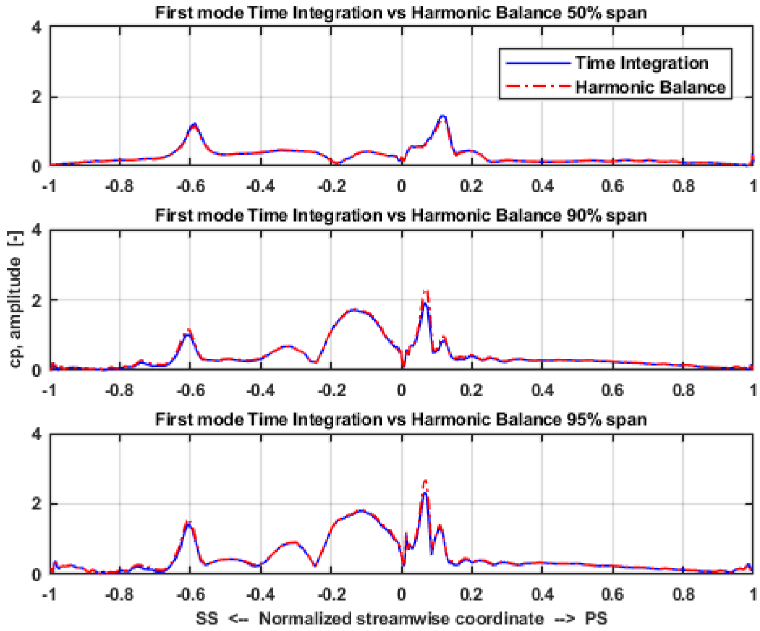

Figure 7.65: Unsteady pressure coefficient comparison between Time Integration and Harmonic Balance method for the first mode in the least stable condition

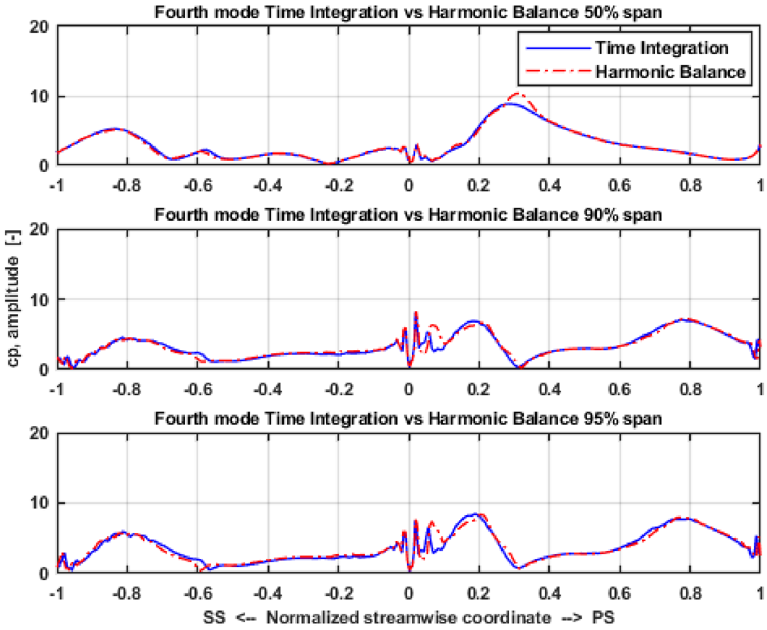

Figure 7.66: Unsteady pressure coefficient comparison between Time Integration and Harmonic Balance method for the fourth mode in the least stable condition

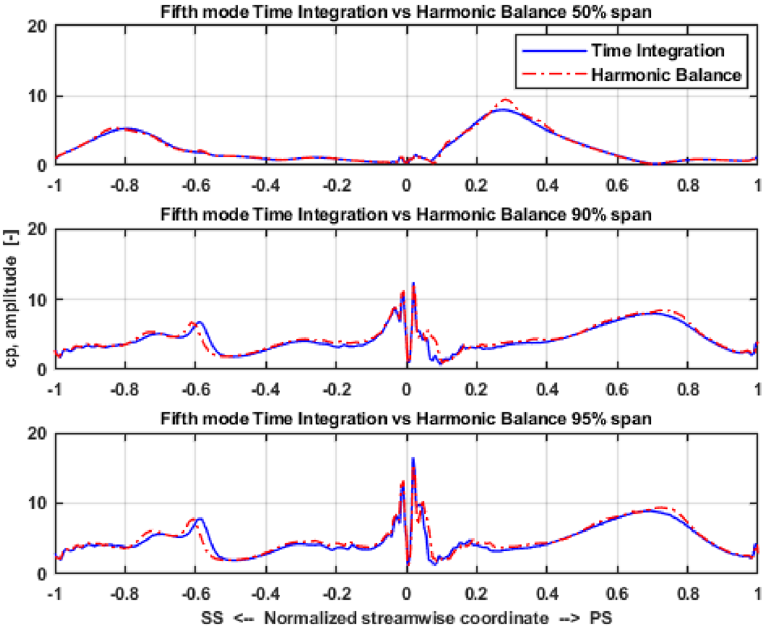

Figure 7.67: Unsteady pressure coefficient comparison between Time Integration and Harmonic Balance method for the fifth mode in the least stable condition

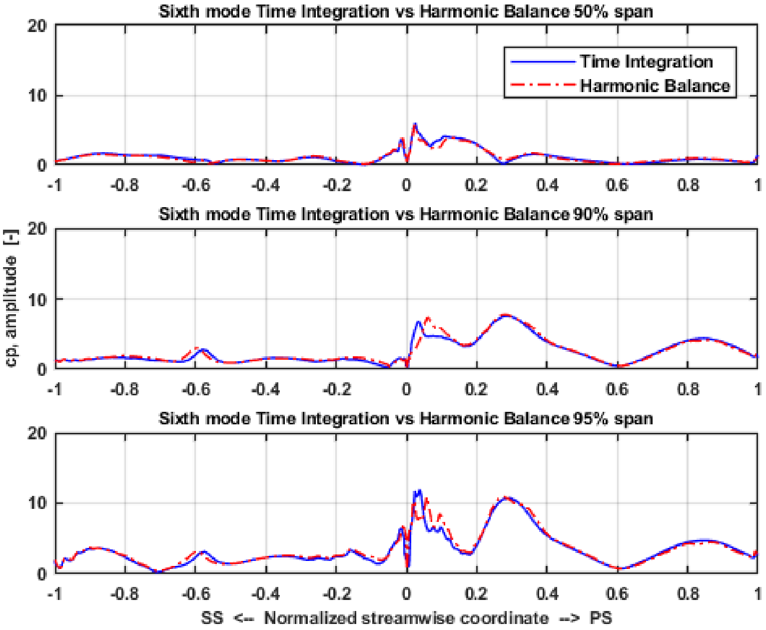

Figure 7.68: Unsteady pressure coefficient comparison between Time Integration and Harmonic Balance method for the fifth mode in the least stable condition

8 CONCLUSION AND FUTURE WORK

In this numerical study conducted on the first stage of VINK6 compressor, steady-state blade loading and Mach number flow field in design condition (design throttle and nominal rotational speed) and aerodynamic damping for the first six modes have been investigated. The numerical tool chosen for the analysis is ANSYS CFX, composed by CFX-Pre, which is used for setting the transient method and the numerical parameters, CFX-Solver and CFD-post, useful for post-processing the solution and getting insights into the quantities of interest as function of the initial setup. Firstly, steady-state simulations of the whole stage has been computed. Three different mesh refinements have been used for k-epsilon and SST turbulence model. Only the rotor blade loading has been taken into account since successive unsteady simulations aims to get aerodynamic damping of this rotating blade row for different blade deformations. Steady-state blade loading with k-epsilon model are mesh independent, thus the medium mesh refinement represents the optimum case in terms of computational effort and accuracy. Steady-state blade loading with SST model predicts a less sharp shock along the suction side and especially for higher span locations mesh independence is not completely verified. Therefore, in this case, it is fair to continue investigating the finest mesh in order to try to understand unsteady phenomena occurring due to this turbulence approach. The blade is more fore-loaded for higher span heights since the shock at mid-chord occurs at higher streamwise locations. The Mach flow field shows a bow shock at the leading edge, which propagates until mid-chord of the adjacent blade. After the shock the flow gets subsonic, while before it is supersonic since the compressor operates in the transonic regime. Steady-state simulations of the rotor alone have been after conducted in order to match the blade loading curve of the rotor obtained from the stage simulation. From here on, only medium mesh with k-epsilon model and fine mesh with SST model have been employed. After getting the same trend for rotor steady simulation, unsteady investigations have been set up. Two different transient methods have been used, which are Time Integration and Harmonic Balance method. Logarithmic decrement distribution computed with the Energy Method has been calculated for the first, fourth, fifth and sixth mode. The first mode is the only one affected by possible flutter risk as the least stable mode approaches the stability line. The other modes feature high reduced frequencies, out of the critical range found in literature, thus the flutter risk is not relevant. The average value and the peak-to-peak amplitude of the S-shape curves are higher as much as lower natural frequency of the modes is. In fact, the first mode features the highest average value and peak-to-peak amplitude. Deviation between aerodamping values for the two blades prescribed by the Fourier transformation method has been stated for each S-shape curve and it is higher where the logarithmic decrement is lower. For $ND = 0$, deviation values seem accurate for all the investigated mode. For higher reduced-frequency modes convergence has been tougher to be attained than for the first mode; simulations of these cases have been extended to P=35 getting Peak-to-Peak and Steady-Value torque error equal to 0. This means simulations are completely convergent but for the fourth and fifth mode a discrepancy between aerodamping values of the two blades is still present. The causes of this mismatch can be related to numerical issue, as the non-reflective boundary conditions at inlet and outlet of the domain. SST and k-epsilon turbulence model have been compared for the unsteady case; again the SST model shows a less sharp pressure peak, but the unsteady pressure and local work coefficient distribution are almost the same as the k-epsilon case for each span location. From here on, only the k-epsilon turbulence model has been used in unsteady simulations. By simulating only the last stable condition for the second and third mode and taking only the least stable condition from the S-shape curve for the other analyzed modes interesting insights can be obtained in terms of unsteady pressure and local work coefficient distribution. Each mode has its displacement amplitudes and directions, which lead to different pressure profiles and unstable regions as function of the span and streamwise location. At 95% span all the unsteady pressure distributions are comparable since the highest displacement has been found in this area; at 50% span unsteady pressure profiles depend on the specific mode shape. In general higher unsteady pressure values have been found at higher span location, except for the fourth and fifth mode cases where the specific direction of these mode shapes lead to higher unsteadiness around mid-span region. The first mode pressure profile features lower unsteady pressure values than other modes, however a deeper study has shown the dependence on the unsteady pressure phase in this case, which can be unfavorable in same configurations and yield lower pressure values. A deeper study has also be performed for the fourth mode, where convergence level has been investigated and scaling factor. In particular doubling or halving the scaling factor, doubled or halved unsteady pressure should be obtained. However, this analysis has shown some non-linearities since the unsteady pressure distribution are not perfectly consistent. CFX Fourier transformation has been checked with the one implemented in MATLAB with the Fast Fourier Transform (FFT) function. From this investigation it can be concluded that when the convergence level is below 0.1% for Peak-to-Peak and Steady-Value torque error both by computing the Fourier transformation in MATLAB for the last period the agreement with CFX predictions is almost perfect. The discrepancy values between the two predictions in a given significant streamwise position have been quantified and convergence level can be considered acceptable when discrepancy values are below 0.5%. This means CFX predictions are quite reliable since they make use of converged pressure values. Harmonic balance method has shown the same trend of S-shape curve, unsteady pressure coefficient and local work coefficient distribution that means these numerical predictions are robust enough with respect to the numerical setup.

Future works can make use of these predictions to build up the cascade test rig and try to get an agreement between experimental measurements and numerical values. Unsteady pressure on the blade due to the fluid flow and aerodamping values have been predicted and validated for a wide range of cases, therefore further more specific investigations on the same blading can be performed starting from these results.

Bibliography

[1]Petrie-Repar, P.

Lecture notes, *Aeromechanics project course, Kungliga Tekniska Högskolan*, *Department of Energy Technology* (2019)

[2]Jiří Čečrdle

"Whirl Flutter of Turboprop Aircraft Structures", *Woodhead Publishing* (2015)

[3]Fridh, J., Glodic N.

Lecture notes, *Thermal Turbomachinery course, Kungliga Tekniska Högskolan, Department of Energy Technology* (2019)

[4]Fasana, A., Marchesiello, S.

"Meccanica delle vibrazioni", CLUT (2006)

[5]Bendiksen, O., Kielb, R.E., Hall, K.C.

"Turbomachinery Aeroelasticity", *Encyclopedia of Aerospace Engineering, John Wiley* & *Sons, Ltd* (2010)

[6]Doi, H.

"Fluid/Structure Coupled Aeroelastic Computations For Transonic Flows in Turbomachinery", *a dissertation submitted to the department of aeronautics and astronautics and the committee on graduate studies of Stanford University in partial fulfillment of the requirements for the degree of doctor of philosophy* (2002)

[7] Biollo,R., Benini, E.

"Recent advances in transonic axial compressor aerodynamics", *Prog. Aerosp. Sci.* (2013)

[8]Albin, B.

"Transonic flow in turbomachines", *Computerized Educational Platform Heat and Power Technology, Stockolm/Lausanne* (2005)

[9]Rampado, M.

"Analisi numerica dell'interazione fluido-strutturale in una turbina di bassa pressione", *Tesi di laurea magistrale, Università Degli Studi di Padova, Dipartimento di Ingegneria Industriale DII* (2015)

[10] Verdon, J. M.

"Linearized Unsteady Aerodynamic Theory", *AGARD Manual on Aeroelasticity in Axial-Flow Turbomachines, Vol. 1, Unsteady Turbomachinery Aerodynamics, Chapter 2* (1987)

[11]Zhao, F., Nipkau, J., Vahdati, M.

"Influence of acoustic reflection on flutter stability of an embedded blade row", *Mechanical Engineering Department, Imperial College London, London, UK* (2015)

[12]Vogt, D.M.

"Experimental Investigations of Three-Dimensional Mechanisms in Low-Pressure Turbine Flutter", *Doctoral Thesis, Kungliga Tekniska Högskolan, Department of Energy Technology, Stockholm* (2005)

[13] Panovsky, J., Kielb, R. E.

"A Design Method to Prevent Low Pressure Turbine Blade Flutter", *Journal of Engineering for Gas Turbines and Power, Vol. 122, pp. 89-98* (2000)

[14]Chernysheva, O.V., Fransson, T.H., Kielb, R.E., Barter, J.

"Influence of a Vibration Amplitude Distribution on the Aerodynamic Stability of a Low-

Pressure Turbine Sectored Vane", *proceedings 10th International Symposium on Aerodynamics, Aeroacoustics and Aeroelasticity of Turbomachines (ISUAAAT), Durham, North Carolina, USA* (2003)

[15]Crawley, E. F.

"Aeroelastic Formulation for Tuned and Mistuned Rotors", *AGARD Manual on Aeroelasticity in Axial-Flow Turbomachines, Vol.2, Structural Dynamics and Aeroelasticity, Chapter 19 (*1988)

[16]Fransson, T.H., Et al

"Aeroelasticity in Turbomachines comparison of Theoretical and Experimental Cascade Results", *EPFL, Lausanne* (1986)

[17] Torsten, H., Fransson, T.H.

"Aeroelasticity in Axial-Flow Turbomachines"**,** *Book 1 and Book 2*

[18]Stasolla, V., Carillo Segura, S., Mohan, A., Bakhshandeh, M.

Minor project technical report, *Aeromech project course, Kungliga Tekniska Högskolan, Department of Energy Technology* (2019)

[19]Nowinski, M., Panovsky, J.

"Flutter Mechanisms in Low Pressure Turbine Blades"*, J. of Engineering for Gas Turbines and Power, Vol. 122, 2000, pp. 82-88* (2000)

[20]Glodic, N.

"Sensitivity of Aeroelastic Properties of an Oscillating LPT Cascade", *Licentiate Thesis*, *Kungliga Tekniska Högskolan, Department of Energy Technology, Stockholm* (2013)

[21]Lejon, M., Grönstedt, T., Glodic, N., Petrie-Repar, P.,Genrup, M., Mann, A.

"Multidisciplinary design of a three stage high speed booster", *Turbine Technical Conference and Exposition, ASME, Charlotte, USA* (2013)

[22]Fröhler, B.

"Aeroelastic Investigation of the 1st Stage VINK Compressor", *Technical report, Thrust Internship, Kungliga Tekniska Högskolan, Department of Energy Technology* (2017)

[23]ANSYS CFX 19.2

"ANSYS CFX 19.2 Documentation", *ANSYS* (2019)

[24]Raw M.

"A new Control-Volume based Finite Element Procedure for the Numerical Solution of the Fluid Flow and Scalar Transport Equations", *Ph.D.Thesis, University of Waterloo, Canad*a (1985)

[25]Barth T. J., Jesperson D.C.

"The Design and Application of Upwind Schemes on Unstructured Meshes", *AIAA Paper 89-0366* (1989)

[26]Rhie C. M., Chow W. L.

"Numerical Study of the Turbulent Flow past an Airfoil with Trailing Edge Separation", *AIAA Journal, 21, 1525-1532* (1983)

[27]Hutchinson, B. R., Raithby, G. D.

"A Multigrid Method based on the Additive Correction Strategy", *Numerical Heat Transfer, 19, 511-530* (1986)

[28]Raw, M.

"Robustness of Coupled Algebraic Multigrid for Navier-Stokes Equations", *AIAA Paper-960297, 34th AIAA Aerospace Science Meeting, Reno* (1996)

[29]Versteeg, H.K., Malalaseker, W.

"An Introduction to Computational Fluid Dynamics", Pearson Education Limited 1995, 2nd edition (2007)

[30]Menter, F. R.

"Two-equation Eddy-viscosity Turbulence Models for Engineering Applications", *AIAA Journal, 32(8), 1598 – 1605* (1994)

[31]Elder, R., Woods, I., Patil, S., Holmes W., Steed, R., Hutchinson, B.

"Investigation of efficient cfd methods for the prediction of blade damping", *Turbine Technical Conference and Exposition, ASME, San Antonio, Texas, USA* (2013)

[32]Hall, K.C, Jeffrey, P. T., Clark, W.S.

"Computation of Unsteady Nonlinear Flow in Cascades Using a Harmonic Balance Technique", *Duke University, Durham, North Carolina* (2002)

[33]Cornelius, C., Biesinger, T., Galpin, P., Braune, A.

" Experimental and Computational Analysis of a Multistage Axial Compressor Including Stall Prediction by Steady and Transient CFD Methods ", *J. Turbomach., vol. 136, no. 6* (2013)

[34] Zeeshan, S.

"Feasibility of Using Morphing Inlet Guide Vanes for Improved Aerodynamics Performance and Reduced Forcing", *Master Thesis Report, Kungliga Tekniska Högskolan, Department of Energy Technology, Stockholm* (2017)

[35]Cumpsty, N.A.

"Compressor Aerodynamics", *Longman Group UK ltd* (1989)